Local magnetoelastic field control in nanostructure arrays for straintronic applications

Nabil Challab

N° attribué par la bibliothèque

|__|__|__|__|__|__|__|__|__|__|

Thèse

Pour obtenir le grade de

Docteur de l'université Sorbonne Paris Nord

Spécialité : Sciences des Matériaux

Présentée par

Nabil Challab

Local magnetoelastic field control in nanostructure arrays for straintronic applications

Soutenue le 08 juillet 2021 devant le jury composé de :

Président		
	Maximilien Cazayous	Université de Paris
Rapporteur		
	Matthieu Bailleul	Université de Strasbourg
	Denys Makarov	HZDR Dresden (Germany)
Examinateur		
	Adekunle O. Adeyeye	Durham University (United Kindem)
	Flavio Abreu Araujo	Université Catholique de Louvain (Belgium)
	Mohamed Haboussi	Université Sorbonne Paris Nord
Directeurs de thèse		
	Damien Faurie	Université Sorbonne Paris Nord
	Fatih Zighem	Université Sorbonne Paris Nord

Université Sorbonne Paris Nord
Laboratoire des Sciences des Procédés et des Matériaux (LSPM)
UPR CNRS 3407, 99 avenue J.-B. Clément, 93430 Villetaneuse, France

THESE

Acknowledgments

There are adventures that one wishes would last forever and my PhD thesis is one of them. It is one of them thanks to many people who gave me the desire to go ahead and gave me the opportunity to realise a dream and to honor my parents' wishes. My story started when I applied for the PSM master at the Galileo Institute and after an interview with Paolo Pedri and Frédéric Du Burck. I would like to thank them very warmly for giving me the opportunity to enter the master and to resume my studies. I would also like to thank all the pedagogical and administrative staff involved in the Master. Thank you to Mourad Cherif for your support and encouragement during all these years. I would like to thank Mohamed Belmeguenai who gave me the chance to join the laboratory of process and material sciences through my master's internship and especially for having taught me the processes and introduced me to the field of scientific research.

This opened up the possibility of doing a thesis but sometimes events and circumstances change the course of things. I did a second Master 2 and in parallel I participated in a research project with Fatih Zighem, Mohamed Haboussi and Damien Faurie. Spending hours reviewing the calculation code and checking the results and reviewing the equations and the implemented model is not an easy task when Mohamed and Fatih are the project leaders. Staying late in the office to make sure that everything was going well in the code was a recurring thing with Mohamed Haboussi. We would 'forget' about the equations and all the boundary conditions. I learned so much during this experience and we had a lot of fun working late to find solutions. This adventure continued during the thesis I started in 2017. I would like to thank Fatih for opening all the doors for me to flourish in my work. I did absolutely everything I wanted to experiment without constraints even though I used constraints in my research work. I thank my directors Fatih and Damien, Mohamed Haboussi, Mohamed Belmeguenai, Yves Roussigné and Philippe Djemia for their availability and the various scientific discussions that allowed me to move forward and solve many problems encountered in the experiments and calculations. A big thank you to Nicolas Grenèche (in charge of the MAGI calculator on which I did all my simulations) for his availability and his help each time we called on him. My stay at the National University of Singapore was a very enriching adventure both on a personal and scientific level. I would like to take this opportunity to thank Professor Adekunle Olusola Adeyeye for his hospitality and for giving me access to all the measurement and characterisation devices and instruments available in his laboratory. I had the chance to explore and discover many experimental techniques that I did not know before this mobility.

My thanks to all the administrative staff of the laboratory Nathalie Duros, Ouafa Rahmani, Sandrine Ouazan and Chrystel Redon; the staff of the study and engineering department especially Noël Girodon for all the developments of precision tools which served me in the assembly of the measurement benches. My thanks to Greg Chalvignac from the IT department for all his help.

My thanks to all the members of the jury who did me the honor of listening to me during my presentation and the very instructive exchange during the questions. I would like to take this opportunity to thank the two rapporteurs of my thesis, Denys Makarov and Flavio Abreu Araujo, for all their remarks and proposals.

In an experience like the thesis, one needs a lot of moral support and backing. Friends and relatives are a support on which one can count on and I did not lack this because I was well surrounded. I thank Mohamed Aouali and Djilali Merouani for all the support they gave me, Safia Mohand Oussaid for her unfailing friendship, Menad Boussaid, Djoudi Ourdani, Hatem Ammar, Ramdane Yachir, Aziz Aoudjhane, Wahiba and Yacine Sedoud, Damia Dekkar, Ahmed Andaloussi, Siham Sodki, Ibtissem Benguettat and Marwa Dhahri for their presence and encouragement. I thank Salima Benchabane who was patient and present especially during the preparation and who endured with me the stress before the defense.
The Meghar family whom I thank infinitely for all the support during a very difficult period. I would like to express my gratitude to Maître Labbad Meghar for his help and unfailing support.
My family, my brother Yacine who has always been there, who has always encouraged me to go forward and succeed. My sister Linda, my brothers Khelil, Sofiane and Faouzi thank you for all the encouragement and assistance. I still have fond memories of using an iron door, as we didn't have a blackboard, to do our revision when I was in primary school. Thank you for all those moments.

A huge thank you and gratitude to my parents. These few lines are not enough, nothing will be enough to thank you and return all the good and happiness you have given me. I hope I have made you happy even for a moment and honoured you through this modest work. I dedicate all my titles and achievements to you, which I would never have accomplished without you, my two doctors. "To you, my dear friend Josseph, I dedicate all my titles and achievements that I would never have achieved without you, my two doctors.
To you my dear friend Josseph who left so early, thank you for everything. All my thoughts FRIEND.

"**The fear of failure is a failure in itself**"

Remerciements

Il est des aventures qu'on souhaite éternelle et celle de ma thèse de doctorat en est une. C'en est une grâce à beaucoup de personnes qui m'ont donné envie d'aller de l'avant et m'ont donné l'opportunité de réaliser un rêve et d'honorer la volonté de mes parents. Mon histoire a commencé quand j'ai candidaté au master PSM de l'institut Galilée et après un entretien avec messieurs Paolo Pedri et Frédéric Du Burck. Je tiens à les remercier très chaleureusement pour m'avoir donné l'opportunité d'intégrer le master et de reprendre mes études. Je remercie également tout le personnel pédagogique et administratif qui intervient dans le master. Merci à Mourad Cherif pour ton soutien et tes encouragements durant toutes ces années. Je tiens à remercier Mohamed Belmeguenai qui m'a offert la chance d'intégrer le laboratoire des sciences de procédés et des matériaux à travers mon stage de master deux et surtout de m'avoir appris les procédés et introduit au domaine de la recherche scientifique.

Ceci m'a ouvert la possibilité de faire une thèse mais parfois les évènements et circonstances changent le cours des choses. J'ai fait un deuxième Master 2 et en parallèle j'ai participé à un projet de recherche avec Fatih Zighem, Mohamed Haboussi et Damien Faurie. Passer des heures à revoir le code de calcul et vérifier les résultats et revoir les équations et le modèle implémenté n'est pas une mince affaire quand Mohamed et Fatih sont les chefs de projet. Rester tard au bureau pour s'assurer que tout allait bien dans le code était chose récurrente avec Mohamed Haboussi. On « s'oubliait » dans les équations et toutes les conditions aux limites. J'ai tant appris durant cette expérience et on s'est beaucoup amusé en travaillant tard pour trouver des solutions. Cette aventure a continué durant la thèse que j'ai entamée en 2017. Je tiens à remercier Fatih pour m'avoir ouvert toutes les portes afin que je m'épanouisse dans mon travail. J'ai fait absolument tout ce que je voulais expérimenter sans contrainte même si je faisais recours aux contraintes dans mes travaux de recherche. Je remercie mes directeurs Fatih et Damien, Mohamed Haboussi, Mohamed Belmeguenai, Yves Roussigné et Philippe Djemia pour leurs disponibilités et les différentes discussions scientifiques qui m'ont permis d'aller de l'avant et de résoudre beaucoup de problèmes rencontrés dans les expérimentations et les calculs. Un grand merci à Nicolas Grenèche (responsable de calculateur MAGI sur lequel j'ai fait toutes mes simulations) pour sa disponibilité et son aide à chaque fois que l'on fait appel à lui. Mon séjour à l'université de Nationale de Singapour était une aventure très enrichissante à la fois sur le plan personnel et le plan scientifique. Je remercie à cette occasion le professeur Adekunle Olusola Adeyeye pour son accueil, pour m'avoir donné la possibilité d'accéder à tous les dispositifs et instruments de mesures et caractérisation disponibles au sein de son laboratoire. J'ai eu la chance d'explorer et de découvrir plein de techniques expérimentales que je ne connaissais pas avant cette mobilité.

Mes remerciements à l'ensemble du personnel administratif du laboratoire Nathalie Duros, Ouafa Rahmani, Sandrine Ouazan et Chrystel Redon ; le personnel du service d'étude et ingénierie particulièrement Noël Girodon pour tous les développements d'outils de précision qui m'ont servi dans le montage des bancs de mesures. Mes remerciements à Greg Chalvignac du service informatique pour toute son aide.

Mes remerciements à tous les membres du jury qui m'ont fait l'honneur de m'écouter durant mon exposé et de l'échange, très instructif, durant les questions. Je remercie à cette occasion les deux rapporteurs de ma thèse, Denys Makarov et Flavio Abreu Araujo, pour toutes leurs remarques et propositions.

Dans une expérience comme la thèse, on a besoin de beaucoup d'appui moral et soutien. Les amis et proches sont un appui sur lequel on peut compter et je n'en ai pas manqué car j'étais bien entouré. Je remercie Mohamed Aouali et Djilali Merouani pour tout le soutien qu'ils m'ont apporté, Safia Mohand Oussaid pour son amitié indéfectible, Menad Boussaid, Djoudi Ourdani, Hatem Ammar, Ramdane Yachir, Aziz Aoudjhane, Wahiba et Yacine Sedoud, Damia Dekkar, Ahmed Andaloussi, Siham Sodki, Ibtissem Benguettat et Marwa Dhahri pour leur présence et leur encouragement. Je remercie Salima Benchabane qui était patiente et présente surtout durant les moments de préparation et qui a enduré avec moi le stress avant la soutenance.
La famille Meghar que je remercie infiniment pour tout le soutien durant une période très difficile. Je tiens à témoigner toute ma reconnaissance à Maître Labbad Meghar pour son aide et tout son soutien.
Ma famille, mon frère Yacine qui a toujours été présent, qui m'a toujours encouragé à aller de l'avant et réussir. Ma sœur Linda, mes frères Khelil, Sofiane et Faouzi merci pour tous les encouragements et pour toute l'assistance. Je garde toujours ce bon souvenir quand on utilisait une porte en fer, car on n'avait pas de tableau, pour faire nos révisions quand j'étais au primaire. Merci pour tous ces moments.
Un immense merci et plein de gratitude à mes parents. Ces quelques lignes ne suffisent pas, rien ne suffira pour vous remercier et vous rendre tout le bien et le bonheur que vous m'avez apporté. Je souhaite vous avoir rendu heureux ne serait-ce qu'un instant et vous avoir honoré à travers ce modeste travail. Je vous dédie tous mes titres et toutes mes réussites que je n'aurais jamais accomplis sans vous mes deux Docteurs. « Nerza Assalou » comme dit mon père.
A toi mon cher ami Joseph parti si tôt, merci pour tout. Toutes mes pensées l'AMI.

« La peur de l'échec est un échec en soi ».

Contents

1 Introduction

Contents

Since about two decades, the need to understand the links between magnetoelectric properties of nanoscale systems and their strains has been of increasing interest. The reasons for this renewed interest in fundamental or applied physics studies on magnetoelastic (or indirect magnetoelectric) effects are multiple. They are linked to the recent appearance of new thematic fields of nanomagnetism such as:
(i) Curvilinear magnetism which deals with the effects of curvatures of nanometric objects on the magnetic configuration.
(ii) Straintronics, which aims at developing magnetoelectric systems whose performance is controlled by elastic strains.
(iii) Flexible or stretchable magnetoelectric systems which are the subject of applied studies on the performance of thin films and magnetic nanostructures on flexible substrates.
In all cases, the understanding of magnetoelastic effects at small scales is important because they condition the properties of the objects studied. My thesis is an experimental and numerical contribution to the understanding of magnetoelastic effects in nanostructures, whose geometrical limitations lead to heterogeneous fields (magnetic and elastic). My work is at the crossroads of these three thematic fields, it includes a numerical development in micromagnetism including heterogeneous strain fields and validations of

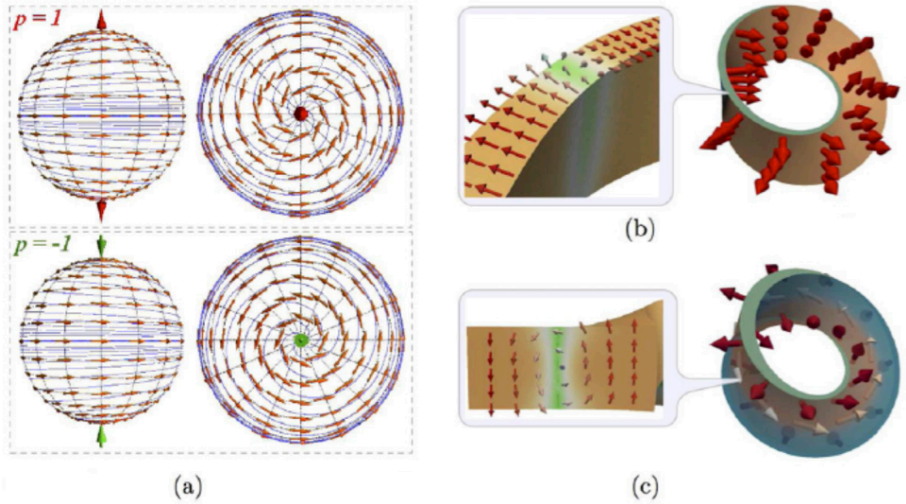

Figure 1.1: Shape-induced patterning [1]: (a) Topologically induced double vortex ground state of soft magnetic spherical shell [2]. (b), (c) Topologically induced domain walls appear as a ground state in magnetic Möbius ring with strong easy-normal anisotropy [3].

this approach on ferromagnetic nanostructures. Before addressing the motivation of my thesis, we first provide a brief overview of these three fields. Then, we will briefly review the state of the art of existing methods to probe the magnetomechanical properties of thin films and nanostructures, both experimental and numerical.

1.1 Current topics involving magnetoelasticity

1.1.1 Curvilinear magnetism

Curvilinear magnetism took off in the 2010s. It consists most often in dealing with 1D or 2D magnetic objects subjected to curvatures in 3D space. These strong curvatures lead to considerable modifications of the fundamental physical (magnetic) properties of the object considered, with for example topological effects [1]. The absence of symmetry inversion and the emergence of effective anisotropy and Dzyaloshinskii-Moriya interaction (DMI) lead to curvature-induced magnetochiral responses and topology-induced magnetization shaping. These effects can therefore have a strong impact on multiple applications involving for example topological defects (such as skyrmions) or spin wave propagation. If the current studies are essentially fundamental, the experimental mastery of these objects could allow to take advantage of these phenomena for applications in spintronics, as an alternative to other approaches *e.g.* the interfacial DMI (in ferromagnetic/heavy metal layer stacks).

For example, figure 1.1 shows the magnetization pattern for curved objects, such as a

spherical shell with a double vortex, or in a Mobiüs ring where the anisotropy induced by the curvature makes a magnetic domain wall appear. Up to now, theoretical research on curvature effects in magnetic objects has focused heavily on the energies involved. These include the Heisenberg exchange, anisotropy and DMI which are local contributions. Moreover, authors have also shown the role of dipolar interaction on curvature-induced anisotropy. This last effect has also generated a preferential chirality of the domain walls in cylindrical shells and a resulting asymmetry of the spin wave spectra [4]. In this context, much work remains to be done to understand the effects of curvature in arbitrary geometries, including theory-experiment confrontations. Hence, it will also be necessary to include the effects of strains in the object, probably very localized (given the strong curvatures) for the comparisons to be fruitful. For the moment, there is no such numerical code taking into account very heterogeneous strains to estimate their effect on the stabilization (or not) of topological defects (domain walls, vortices, skyrmions, Bloch points). Without reaching such an objective, we will see that my thesis work can contribute to the development of such a model.

1.1.2 Straintronics

In general, straintronics is a broad field of condensed matter physics that concerns the control of physical properties by the deformation of the crystal lattice. In the field of magnetism, there are many topics since 2000 related to the development of artificial multiferroics. From an application point of view, the objective is to develop electronic devices to control the magnetic state by an electric field and *vice versa* [5, 6, 7]. For example, in the field of spintronics, one ambition is to obtain a voltage control of the magnetization to design and develop electrically writable, non-volatile, magnetic memories with low energy consumption [8]. One way is to design artificial magnetoelectric composites combining ferroelectric and magnetic media [9]. These composites show several geometrical features, comprising magnetic thin films or nanostructures on ferroelectric substrates or actuators [10, 11].

An example of application of straintronics is the control of domain wall propagation properties in magnetic nanowires by strains (figure 1.2) [12]. It is shown in Lei *et al.* [12] that the movement of DWs can be electrically controlled at room temperature using indirect magnetoelectric coupling *via* the $PbZr_{1-x}Ti_xO_3$ substrate (PZT)/nanostructure interface. In particular, figure 1.2-ii shows that the energy barrier of the domain walls can be doubled by varying the voltage from 0 to -50V or +50V, which is quite interesting in spintronic applications. The inclusion of PZT electrodes would also endow the additional function of addressable content, as domain walls in parts of a racetrack could be 'clamped' by applied electric fields, while walls in other parts could continue to be shifted along the wire. These developments are potentially interesting if one is capable of a very good control of the local strain fields.
Another example is the control of the magnetic configuration of micrometric structures deposited on a PMN-PT ferroelectric substrate (figure 1.3-a). These experiments show that the magnetic configuration under strain can vary considerably by changing the

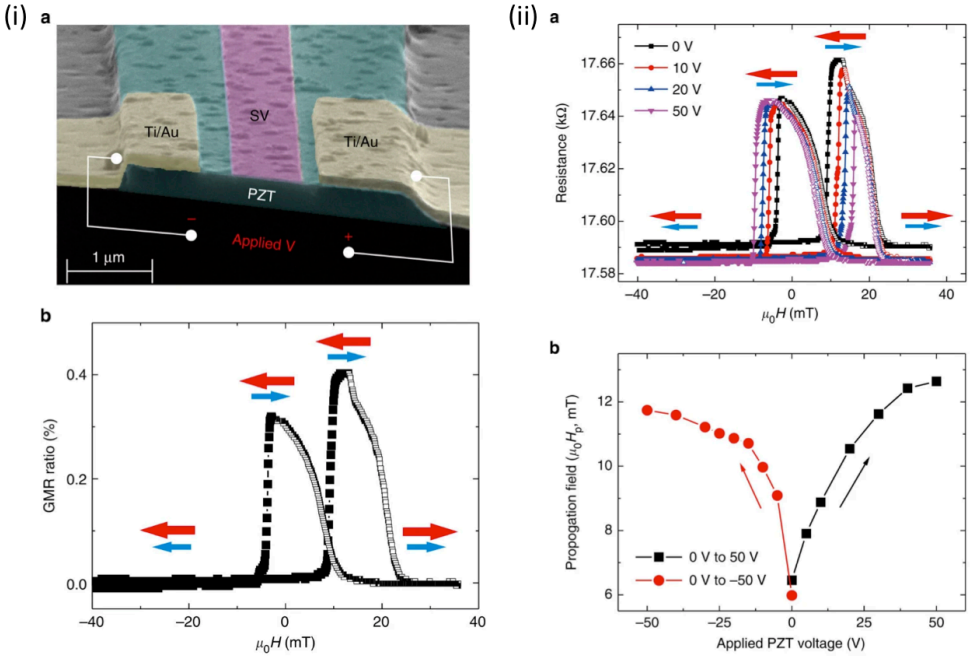

Figure 1.2: (i) a: Cross section of a hybrid PZT and spin-valve (SV) hall bar-shaped device measured by scanning electron microscopy. SV strip is located in the middle of PZT, and side electrodes are in a good contact with PZT side walls. b: GMR loops of SV strip, which is measured by sweeping an external magnetic field H is along easy axis. The free-layer and pinned-layer magnetization reversal with applied field are shown with solid black squares and open black squares, respectively.(ii) a: Giant magnetoresistance loops with different applied voltages, which starts from a depolarized state of the PZT layer. b: Propagation field in the free layer as a function of the voltage applied on the PZT layer. The figure is adapted from [12].

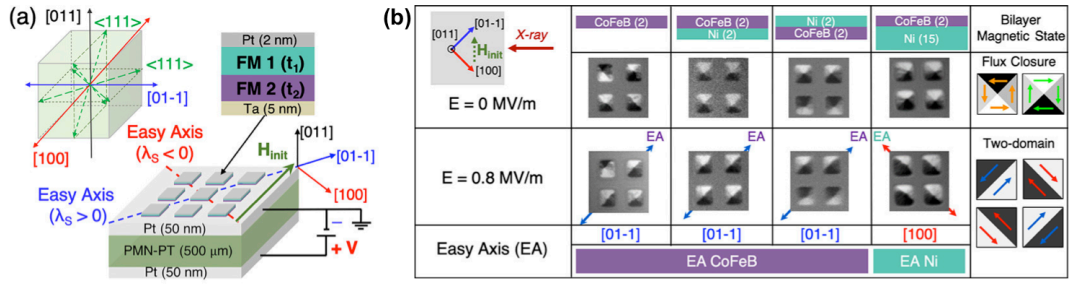

Figure 1.3: (a) Schematic of ferromagnetic dots (Ni/CoFeB bilayer systems) deposited on PMN–PT crystal with the surface normal along the [011] crystallographic direction. (b) Electric field-controlled magnetic reorientation in 2 µm microsquares from four different Ni/CoFeB bilayer systems. The ratio between the Ni and CoFeB magnetic volumes controls the magnetoelectric effect in these multiferroic systems.

thickness ratio of two ferromagnetic layers of different materials (Nickel and CoFeB). When the ratio of the two magnetic thicknesses is significantly larger than one, the magnetoelastic properties of the system are dominated by those of the thicker layer. On the other hand, when the layers are of the same thickness, the exchange-coupled microstructures exhibit a more complex behavior, which cannot be described by simply combining the magnetoelastic effects of the two constituent materials, as shown in figure 1.3-b.

In these different cases of straintronics, it is important to understand the magnetoelastic effects and therefore to know how to relate the strain heterogeneities and magnetic field heterogeneities within the same system. In the examples cited, the thicknesses are often very small compared to the lateral dimensions, which may justify neglecting the strain heterogeneities. In addition, PZT or PMN-PT substrates are rigid, which limits the strong strain concentration in the substrate. However, we will see in the following that for larger thicknesses, especially when using flexible substrates, the effects of heterogeneities on magnetic behavior can be significant.

1.1.3 Thin films and nanostructures on flexible/stretchable substrates

The topic of magnetic systems deposited on flexible or extensible substrates has taken off in the 2010s. Indeed, several groups have focused on this issue to show the feasibility of modern deformable magnetoelectronic devices, adaptable to non-planar surfaces. This theme includes applied works but also more fundamental works on magnetoelastic effects in thin films, nanometric stacks, or 1D and 2D nanostructures.

One of the characteristics of these systems is the strong stiffness contrast between the magnetic nanostructures and their substrate, which can make the deformation fields very

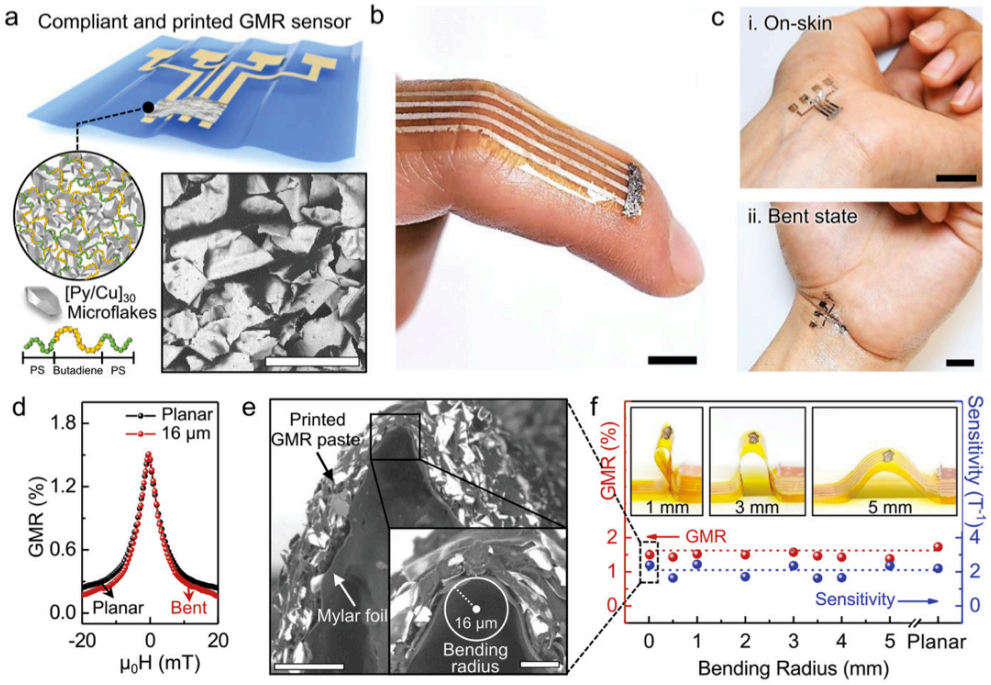

Figure 1.4: a) Schematic of GMR sensors consisting of [Py/Cu]30 microflakes and triblock copolymer (SBS) printed on ultrathin foils. SEM image reveals dried GMR paste printed on a Mylar foil. Scale bar: 100 µm. b,c) Photographs of printed GMR sensors conformably applied on skin with curved body parts of a finger (b) and a stretched (c-i) and bent (c-ii) wrist. Scale bar: 1 cm. d) GMR performance of the printed sensors under planar and bent state (16 µm of bending radius). e) Cross-sectional SEM images of bent GMR sensors printed on an ultrathin Mylar foil. At the apex the GMR sensor is bent to the radius of 16 µm (inset). Scale bars: 100 µm, 20 µm (inset). f) The magnitude of the GMR effect and the sensor sensitivity following the gradual decrease of the bending radius from 5 mm to 16 µm. Taken and adapted from [13].

heterogeneous for nanostructures. This is an important point, which will be quantified in this thesis, and probably still requires fundamental numerical and experimental work. However, for thin films or stacked layers whose lateral dimensions are very large compared to the thickness, the assumption of homogeneous deformation is often true and several works have shown the applicability of flexible or stretchable giant magnetoresistance (GMR) sensors or to a lesser extent giant magnetoimpedance (GMI) sensors.
An example of work on GMR sensors is shown in Figure 1.4. Indeed, Ha et al. recently showed that these sensor devices are capable of detection in low magnetic field (below 1 mT) and sustaining high-performance magnetoresistive sensing under extreme mechanical deformation of up to 16 µm of bending radii (see figure 1.4-f) and 100% stretching. The remarkable performance is achieved by dispersing GMR microflakes of $[Py/Cu]_{30}$ in a viscous triblock copolymer based poly(styrene-butadiene-styrene) (SBS) elastomer (1.4-a). This type of application work, based on fundamental developments, allows to consider new 3D printable devices, light and adaptable to arbitrary geometries, based on the GMR sensor technology.

Other applications than flexible/stretchable GMR sensors can be considered. We think in particular of artificial magnonic crystals which are interesting for high frequency applications (gigahertz range). In order to consider this type of systems on deformable substrates, it is necessary to understand the mechanical properties of these objects and optimize them. This was one of the objectives of S. Merabtine's thesis at LSPM[?], which showed that lateral nanostructuring could be a way to delay damage (cracks), see figure 1.5. Indeed, for a given material thickness, he showed that the cracking of nanolines was much later than that of a continuous film. This is shown in figure 1.5-(i-ii) for $Ni_{80}Fe_{20}$ systems. For these same systems, Merabtine *et al.* also showed that the magnetic anisotropy was insensitive to the multiplication of cracks, at least up to 20% of strain (figure 1.5-(iii)-(a-b)). It is also interesting to see that the FMR linewidths are also very insensitive to these damages, as shown in figure 1.5-(iii)-(c-d), linked in particular to the weak magnetostriction of $Ni_{80}Fe_{20}$.
To go further, it is now important to analyze this type of behavior for systems that are also magnetostrictive, taking into account the distribution of deformation in the system. An analysis of the elastic heterogeneities must be taken into account to analyze this type of study. This is one of the objectives of this thesis: to take into account the effects of strain heterogeneities related to free surfaces and to the stiffness contrast between constituents to properly analyze the magnetomechanical behavior of nanostructured systems on flexible substrates.
In the next paragraph, we will briefly review the state of the art of current methods to measure or model magnetomechanical effects.

1.2 State of art on experimental and numerical methods

1.2.1 Ferromagnetic resonance

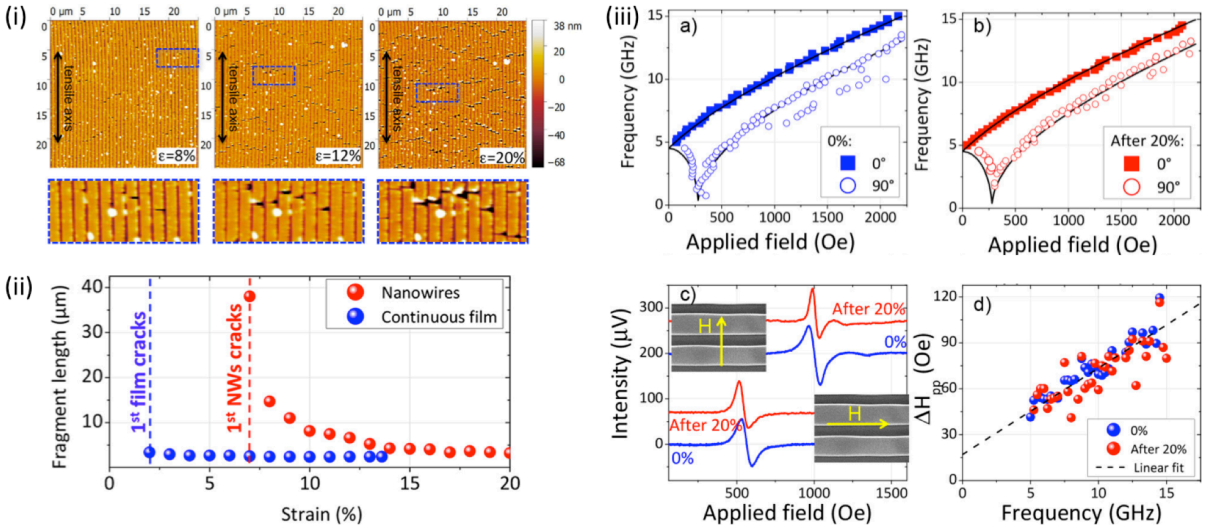

Figure 1.5: (i) Typical AFM images highlighting the multicracking of a 20 nm thick $Ni_{80}Fe_{20}$ array of nanowires on Kapton substrate at different strain states (8%, 12%, and 20%). (ii) Residual fragments length as a function of the applied strains of $Ni_{80}Fe_{20}$ film and arrays of nanowires (NWs). (iii) (a, b) Frequency dependencies as a function of applied magnetic field along and perpendicular to the nanowires for a $Ni_{80}Fe_{20}$ array of nanowires. The dependencies are presented for two stresses states: at 0% (a) and at 20% (b). (c) Typical FMR spectra of the NWs for magnetic field applied along and perpendicular to the NWs at 0% of strain and after 20% of strain. (d) Peak to peak FMR line width ΔH_{pp} variations as a function of the frequency obtained from the spectra recorded with a magnetic field applied along the NWs. The dashed line is a linear fit and serves as a guide for the eyes. Taken and adapted from [14].

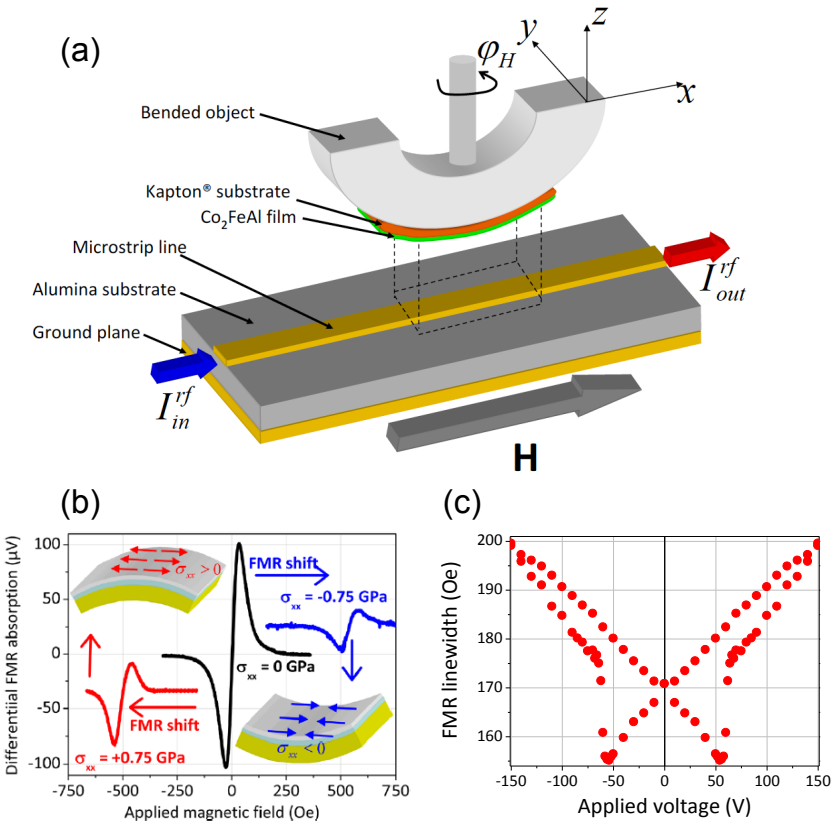

Figure 1.6: (a) Sketch of a bending test combined with broadband FMR [15]. I_{in}^{rf} and I_{out}^{rf} correspond to the injected and transmitted radio frequency current. The static magnetic field $\vec{H}$ is applied along the microstrip-line. (b) Bending effect on FMR lines in a flexible system (CoFeB film on Kapton substrate) [16]. (c) FMR linewidth of FeCuNbSiB thin films on Kapton of as function of voltage applied to a ferroelectric actuator (on which compliant system is cemented) [17].

Ferromagnetic resonance spectroscopy (FMR) [18] is an old but powerful technique to study the magnetization dynamics in thin films and nanostructures [19, 20]. FMR consists in exciting the magnetization of a magnetic material with a microwave field at a certain frequency to make it precess around the effective field. At resonance, the frequency of the microwave field coincides with the precession frequency of the magnetization, absorption is then maximal. This technique offers possibilities for measuring the properties of a magnetic layer either by making a field sweep (the microwave frequency is fixed and the static field is varied) or a frequency sweep (the static field is fixed and the frequency of the microwave field is varied). The conventional FMR technique (with a resonant cavity) is not well suited for *in situ* magneto-mechanical characterization due to the limited available space to perform micro-mechanical testing. This is the reason why several groups have adopted inductive permeameter techniques even if they provide lower sensitivity in the FMR detection [21, 22]. Indeed, they allow greater flexibility in the sample environment with the advantage to work in a broadband regime [23, 24]. *In situ* techniques combining broadband FMR set up and mechanical testing have been recently developed and have made it possible to characterize these phenomena in flexible systems. Several studies have been carried out under tension [25, 26] or bending [15, 16, 27].
Thanks to the FMR detection in thin films and nanostructures, it is possible to study and characterize their dynamic magnetic properties and thus to extract fine informations on their micromagnetic properties from their microwave responses. Figure 1.2.1-a shows a bending support combined with a broadband FMR technique where the sample is close to the microstrip line [15]. Figure 1.2.1-b shows that for a given material (here CoFeB on a Kapton® substrate) the displacement of a FMR line depends on the direction of curvature [16]. Thus, it is possible to characterize systems in both tension and compression. For instance, it is possible to detect the presence of in-plane anisotropies (amplitude and order) by performing in-plane angular measurements or to measure the magnetic damping properties from the resonance peak lines. This last parameter governs the speed at which the magnetization of a ferromagnetic medium can be reversed or reoriented and is a key issue in assessing the potential usefulness of such media. Depending on the intended application, it is better to have low (for MRAM [28], TMR read heads [29], etc.) or high (current-perpendicular to plane giant magneto-resistance read sensors [30], etc.) damping values. In this context, Zighem et *al.* showed a strain-control of the magnetic damping in FeCuNbSiB thin films by combining broadband FMR technique and micro-mechanical test (ferroelectric actuation) [17]. Figure 1.2.1-c shows that the FMR peak-to-peak line-width can be tuned from 150 to 200 Oe depending on the strain state.
Moreover, the signature of the applied strains is very visible by the offset of the resonance lines. This has made it possible, for example, to determine the saturation magnetostriction coefficient of Heusler alloys [15], as well as the evolution of anisotropy under actuation or bending of complex alloys or magnetic oxides [31, 27, 32]. Finally, this technique has also been used to characterize the properties of magneto-impedance systems under bending for wireless applications [33].

1.2.2 Magneto-optical techniques

Among the magneto-optical techniques, Brillouin light scattering (BLS) spectroscopy and magneto-optical Kerr effect (MOKE) magnetometry have been used by different groups to study the magneto-mechanical coupling of flexible magnetic systems. One of the advantage of those techniques is that they allow probing magnetization properties under different kind of mechanical testing (ferroelectric actuator, bending and even tensile with a conventional mini-machine); this is due to the non-contact aspect of these techniques which *in fine* analyze the scattered light by the material.
BLS is based on the inelastic scattering of light by thermally activated wave phenomena (in the GHz range) in a material. BLS gives access to spin wave and surface acoustic wave modes with non-zero wave vectors, but has been little used in combination with mechanical tests. For instance, it has been used by Karboul-Trojet et *al.* to study spin wave energies in a Ni thin film as function of an external uniaxial stress applied thanks to a conventional tensile machine [34]. In the context of flexible magnetic system, its main disadvantage is its acquisition time as compared to FMR since it gives similar results than those obtained by FMR since no group has taken into advantage of the wave-vector dependencies. However, this technique could be of strong interest for future systems such as magnonic crystals on flexible substrates, for studying the evolution of magnonic band structures *versus* of an applied strain.
On the other hand, MOKE magnetometry is more and more used in the field of flexible/stretchable magnetic systems. The magneto-optical Kerr effect is the result of an interaction between an electromagnetic wave and a ferromagnetic material. When an electromagnetic wave interacts with a magnetized material (usually a ferromagnetic material) the polarization of the reflected wave is not the same as that of the incident wave. Thus the analysis of the polarization of the wave as a function of an external static magnetic field makes it possible to follow the magnetization curves of the magnetic material being probed. There are many studies showing the evolution of magnetization curves of magnetic alloys on polymer substrates, to analyze the effect of mechanical stresses on the evolution of the coercive field and remanent magnetization [35, 36, 37, 38, 39, 40, 41]. In the context of flexible magnetic systems, it is indeed easier to use MOKE rather than the other magnetometry techniques such as SQUID (superconducting quantum interference device), VSM (vibrating sample magnetometry), AGFM (alternating gradient field magnetometry), etc... to record magnetization curves as function of the applied strains even if no quantitative value of the magnetic moment is obtained. Therefore, it can be easily coupled to tensile or bending tests [35] to perform *in-situ* strain testing.

1.2.3 Magneto-resistance measurements

Magnetoresistance is the variation of the electrical resistance in the presence of a magnetic field. GMR or TMR systems on polymer substrates have many applications [45, 46]. In the case of magnetic field sensors, the aim is to develop systems that are not very sensitive to strains and damages in order to avoid all the possible additional sources

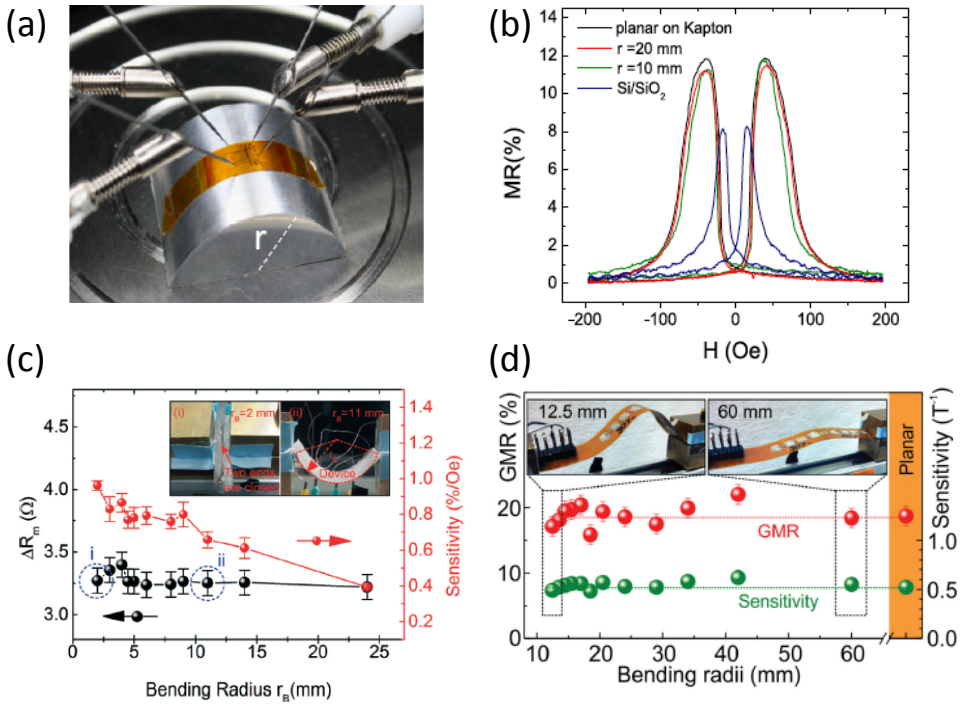

Figure 1.7: (a) Image of a magneto-resistance measurement of a TMR on Kapton in bending [42]. (b) Comparative measurement between several bending states, and comparison with an oxidized silicon substrate [42]. (c) Bending test (charge-discharge) and in situ electrical resistance measurement of a GMR deposited on PET coated with a thin layer of SU-8 polymer [43]. (d) Magnetoelectric performance of a GMR sensor under imposed bending [44].

of perturbations (strain induced response for example) [44]. On the contrary, in the case of strain sensors, magnetoelastic effects will be sought to correlate magneto-resistive behavior and strain field [47, 48]. since flexible magnetic systems have attracted the interest of the scientific community and industry for their high application potential, many groups have tried to develop tensile [49] or bending experiments [42] with *in situ* magneto-resistance measurements. In this context, 4-wire devices under magnetic field have been developed in simple bending, biaxial swelling or simple tension up to potentially very large strains. In general, these tests make it possible, on the one hand, to measure the strain effects on the measured GMR values and, on the other hand, to test the reliability of systems under repeated stress, such as cyclic bending or tensile tests [43]. Figure 1.2.3-a shows a 4-wire measurement system under bending developed by Bedoya-Pinto *et al.* [42]. These measurements made on a TMR system on Kapton show a small effect of strain on their magneto-resistance, as shown in Figure 1.2.3-b [42]. Figures 1.2.3-c and 1.2.3-d show *in situ* bending devices (with motor-controlled mechanical loading setup) to evaluate the evolution of electrical resistance and magneto-resistance, respectively [44]. Figure 1.2.3-d shows a remarkable consistency of the sensitivity of a GMR sensor despite the wide variation of the bending radius (down to 12.5 mm). Overall, all these techniques allow efficient diagnosis of the performance of magneto-resistive sensors under imposed strains.

1.2.4 Magnetization imaging

Finally, although not widely used, a few groups have used magnetic domain imaging techniques (essentially magnetic force (MFM) [50, 51, 52, 53]- and MOKE [38, 40]-microscopies) to study the influence of applied strains on magnetic properties. MOKE microscopy uses the principle of the magneto-optical Kerr effect (see above) with a camera allowing the image of magnetic contrasts on the surface of the material. MFM is a variety of atomic force microscopy, in which a magnetized tip scans a magnetic material; tip/sample magnetic interactions are detected and allow reconstructing the magnetic configuration of the surface.
For example, these techniques can be used for studying the evolution of strip domains. In these specific cases where there is an out-of-plane magnetic contrast, micro-mechanical tests could be adopted because of the geometric space available. For instance, magnetic imaging has been performed by using ferroelectric actuators [52], tensile machines [50, 51] or more recently by bending the system [53] under an atomic force microscopy. In addition, the geometrical space available under the microscope allows to setup studies under applied strain and magnetic field [50, 51].

1.2.5 Numerical methods for magnetomechanical behavior

The numerical description of magnetic nanostructures behavior involves the development of micromagnetic modeling of the Landau-Lifschitz-Gilbert (LLG) equation. The commonly used calculation codes (Nmag [54], Oommf [55] and mumax3 [?]) allow to simulate their dispersion relation in the Brillouin zones [56]. However, there is no pos-

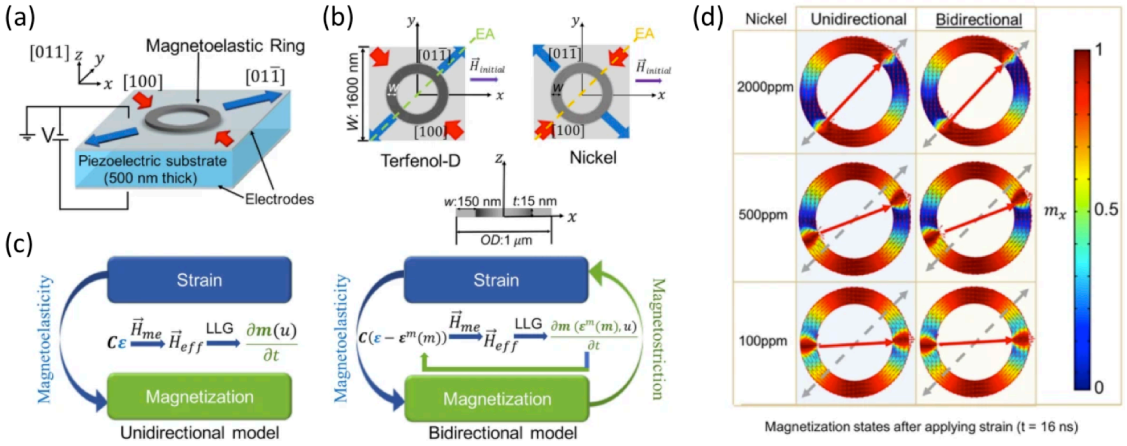

Figure 1.8: Schematic illustrations of (a) setup for the ferromagnetic ring on top of piezoelectric substrate PMN-PT. (b) Top view and cross section view of the magnetoelastic rings (Terfenol-D and Ni). Illustration of the initialization field $H_{initial}$ with respect to the crystal orientations in PMN-PT, and the tensile and compressive response along corresponding directions. EA indicates the strain-induced magnetic easy-axis due to magneto-elastic coupling. (c) Description of the two simulation approaches: the unidirectional model only tracks inverse magnetostrictive effect; while the bidirectional model considers both the magnetostrictive and inverse magnetostrictive effects. (d) Domain wall rotation state in Ni rings at 16ns after strain application predicted by two models when subjected to 2000 ppm, 500 ppm and 100 ppm strains. Adapted from [60].

sibility in these codes to apply inhomogeneous strains. The only possible option is to apply a homogeneous uniaxial stress, which means incorporating a uniform (magnetoelastic) anisotropy field in the simulation. For magnonic crystals on flexible substrates, it is important to include local strains in the problem because heterogeneities can be strong and influence the micromagnetic behavior. The magnetoelastic coupling (magnetization switching, strain and their coupling) must therefore be fully described at the local scale. Few groups have implemented numerical codes that couple the LLG equation describing the magnetization dynamics as well as the solid mechanics ones in strain-mediated artificial multiferroics [57, 58, 59]. These codes could be very well adapted to the problem of systems with flexible substrates.

The model developed by Liang *et al.* [58] is probably the most complete, taking into account both direct (effect of the applied magnetic field on the strain) and inverse (effect of the applied strain on the effective field) magnetostrictive effects, all at the local scale. Note that the inverse magnetostrictive effect is the also called magnetoelastic coupling consisting on the manipulation of the magnetic properties *via* a strain. This

model has been applied to nanorings deposited on a ferroelectric substrate [60]. Figure 1.2.5-(a) shows the modeling scheme of the nanoring deformed by the ferroelectric substrate. The authors studied 2 materials for the nanorings (Ni and Terfenol), Terfenol having a very high magnetostriction coefficient (about 1200.10^{-6}) compared to Ni (about 30.10^{-6}). Figure 1.2.5-(b) shows the geometry of the computational elements, including the applied field and the strain directions. The 1.2.5-(c) shows the two models used, the unidirectional model is the one taking into account only the reverse magnetostriction (magnetoelastic effect), while the bidirectional model takes into account both effects (direct and reverse). The authors have shown that these two models are equivalent for materials with standard magnetostriction such as Nickel (see figure 1.2.5-(d), which is not at all the case for Terfenol. In this example, the strain applied through the application of voltage changes the magnetoelastic energy, causing the "onion" state to re-orient to its new energy minimum configuration and driving the domain walls towards the direction of the principal strain axes.
This example shows that for materials that are classically used in nanomagnetism (Ni, Fe, Co and their alloys), the consideration of the inverse magnetostriction is enough to describe the magnetomechanical behavior. This is why in this work focused on NiFe alloys, we have always neglected the direct effects of magnetostriction. At the present time, no group except ours has been numerically interested in magnetomechanical effects related to compliant substrates.

1.3 Brief summary of the manuscript

My manuscript includes several aspects describing the magnetomechanical behavior of nanostructures. After describing the tools used for the different steps of my work (sample preparation, characterization, analysis, etc.), we will describe the scientific work itself. A large chapter is dedicated to the numerical development of a micromagnetic model of nanostructures on compliant substrate. This part will be followed by results on the effect of strain heterogeneities on the static and dynamic magnetization. After having discussed these effects, two chapters will deal with the effects of heterogeneities on the magnetomechanical behavior of real objects, including experimental (*in situ* FMR)/model confrontations. The first case will be that of NiFe nanoline arrays deposited on Kapton, while the second one will focus on NiFe antidots also deposited on Kapton. Overall, the main thread of the manuscript concerns the relationship between strain and magnetic modes localizations. We will see that these coupled local effects can have a significant influence, especially in the case of magnetic antidots.

2 Micromagnetic and micromechanical numerical methods

Contents

In this chapter, the theoretical aspects of micromagnetic and micromechanical properties are succinctly discussed. Indeed, during this thesis, we have intensively used micromagnetic and micromechanical numerical simulations, either separately or by combining them. When performing separate simulations, OOMMF package has been employed to calculate micromagnetic modes and COMSOL Multiphysics to carry out micromechanical simulations. When combining micromagnetic and micromechanical simulations, we have employed two approaches: i) in the first one, the simulations are achieved separately but we used the results of a simulation to feed the second one. The micromagnetic behavior is first simulated and the magnetic modes were identified and localized within the magnetic nanostructure. The second step consists in the estimation of the transmitted strain in the zone in which the magnetic mode is localized and injected in the model to estimate the resonance field shift. This step is important to take into account the real strain field experienced by the magnetic moments localized in the magnetic mode zone; ii) in the second one, we have fully coupled the magnetic and the mechanical properties of a magnetic medium. For this purpose, we have developed a fully coupled mechanical-micromagnetic model in COMSOL Multiphysics. In the following, we briefly present some basics of the micromagnetic theory before presenting the general philosophy of the micromagnetic simulations carried out under OOMMF. In a second part, we give a short theoretical background regarding the elastic properties of solids before presenting basic numerical results obtained from an array of magnetic nanostructures under mechanical

straining. Finally, the fully coupled mechanical-micromagnetic model developed during this thesis will be presented.

2.1 Spatio-temporal micromagnetic simulations

In this section, we present some aspects of the micromagnetic theory that is generally used to model ferromagnetic objects of small size (from micrometer to nanometer). It was introduced by Brown and assumes that the ferromagnetic medium is continuous. Thus, the atomic details of the origin of the ferromagnetic order are ignored but, as we will see, magnetism at the scale of magnetic domains and walls is fairly well described. Thus, thermodynamic quantities (such as magnetization or the various internal fields) are continuous variables even if their origins are all atomic. We can then define the magnetization of the medium as a vector $\vec{M}(\vec{r},t)$, macrospin approach, of constant modulus M_S evolving in the space and time. This micromagnetic approach is above all energetic. It is then necessary to identify the main phenomena involved in the configuration of the magnetization within the medium and thus associate them an energy. The simulations that we are going to carry out are based on a dynamic model introduced by Landau and Lifshitz which describes the evolution of $\vec{M}(\vec{r},t)$ over time; the equilibrium positions being the relaxed states of the system.

2.1.1 Theoretical background

The study of the magnetization dynamics in ferromagnetic thin films is very important for the understanding of the different phenomena that emerge there, whether they are relaxation, propagation or confinement and localization phenomena. We will therefore introduce the different basic definitions before presenting the model used in homecode simulations. Magnetism in matter takes its origin from the motion of electrons orbiting around a nucleus within an atom. Indeed, an electron in rotation on a closed trajectory can be compared to an electric current flowing through a conducting wire which generates a magnetic field and moment. This electron has an orbital magnetic moment due to its orbital motion around the nucleus, to which is added another moment linked to the rotation of the electron around itself, which also creates a magnetic moment known as the spin magnetic moment. The sum of the moments generated in the same atom gives rise to the atomic magnetic moment, and the contribution of all of the atomic magnetic moments of a given volume of matter gives rise to what is known as magnetization[61, 62]. According to this definition, one can understand that all the atoms (from the periodic table) do not exhibit a magnetic moment.

The most interesting materials in the spintronics domain are the ones with elements carrying a non-zero magnetic moments. The atoms with this characteristics are clearly identified in the Mendeleev periodic table, generally localized in the transition metals whose the d atomic level is incomplete, the lanthanide with an incomplete $3d$ (2.1), $4f$ level and the actinides with an incomplete $5f$ level. So, the relative orientations of the magnetic moments within the magnetic materials gives rise to different magnetic material

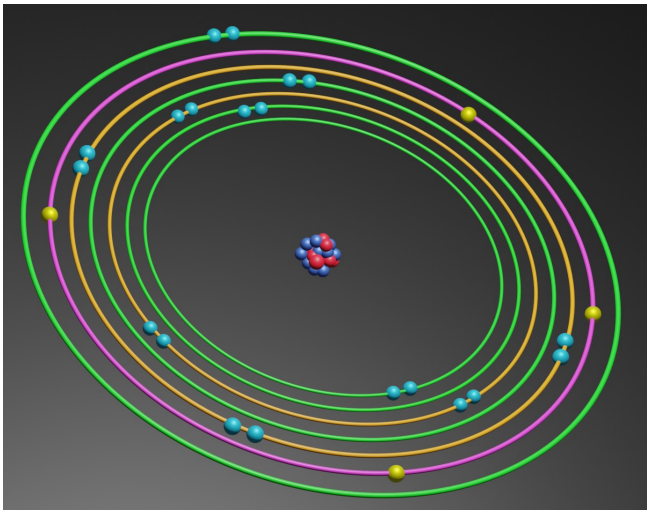

Figure 2.1: Schematic representation of atomic structure with electronic configuration within an atom in which the $3d$ level partially filled. The impaired electons (yellow color) do not have their magnetic moments compensated and give rise to a global magnetic moment in the considered atom in which the paired (blue spheres) have their moments compensated.

classes. Namely the paramagnetic, ferromagnetic, antiferromagnetic and the ferrimagnetic materials. These magnetic orders are schematically represented in figure 2.2. The first sketch corresponds to ferromagnetic materials characterized by a parallel alignment of the magnetic moment at a critical temperature beyond which this ferromagnetic order is lost. Indeed, the effect of the thermal agitation consists in destroying this equilibrium state. The second class is the antiferromagnetic materials, which, as can be deduced from their nomination, represent materials with an "antiparallel" alignment of the magnetic moments of similar amplitudes. Ferrimagnetic materials are quite similar to the antiferromagnetic materials with however antiparallel magnetic moments of different amplitudes. The last class gathers the so-called paramagnetic materials within which the magnetic moments are randomly oriented over the sample[62, 63, 64].

As mentioned earlier, these materials at certain temperature conditions exhibit a spontaneous macroscopic magnetic moment. In other words, there is a temperature above which the ferromagnetic material under consideration exhibits spontaneous magnetization even in the absence of an applied external magnetic field. The explanation was provided by the molecular field model, or internal field model, developed by Pierre Weiss in 1907. This model states that if one were to take a magnetic moment inside a ferromagnetic material, the latter would feel a magnetic field which is nothing more than the resultant of the fields generated by the different magnetic moments of the crystal to which the external magnetic field is added if it is applied. It was in 1928 that Heisenberg provided the explanation of the microscopic origin of the molecular field taken from Weiss

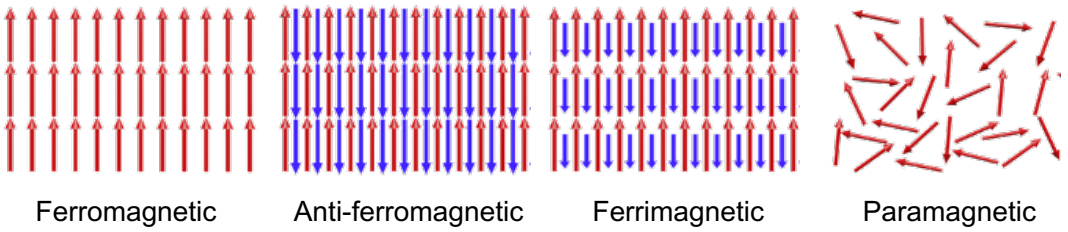

Figure 2.2: Magnetic materials classes. The ferromagnetic order exhibits an homogeneous magnetic moment modulus, the antiferromagnetic an alternative alignment of antiparallel magnetic moments of same modulus, the ferrimagnetic has the same distribution, antiparallel magnetic moment with different amplitudes and the paramagnetic class which shows a random spatial distribution of the magnetic moments.

theory. Indeed, Heisenberg showed that the magnetic moments are aligned thanks to the exchange interaction. The Weiss theory seems incomplete since it does not explain the antiferromagnetic and ferrimagnetic character of certain materials. However, the antiferromagnetic and ferrimagnetic character is the result of local and not long range phenomena. Louis Néel provided an explanation in 1950 by modifying the Weiss model. In Néel's modification, the local nature is taken into account since he introduced the notion of a local molecular field, which therefore takes into account the different nature of the atoms, unlike Weiss theory, where the value of the field is averaged [63, 65, 66]. Ferromagnets are the materials that have interested us during these studies. We will therefore give more details on the Weiss field model in order to introduce the different forms of energy that will be used during the various simulations and interpretations.

Let us consider an atomic magnetic moment in a ferromagnetic material. In the framework of Weiss mean molecular theory, the magnetic moment in question is subject to the mean field that results from the competition of the fields generated by the different magnetic moments, to which we could add the applied magnetic field. The total field then experienced by this magnetic moment is of the form:

$$H = H_{app} + H_{med} \tag{2.1}$$

where H_{app} represents the applied field and H_{med} the average molecular field is of course a function of the magnetic moment of a defined volume in the material - in this case, the magnetization is considered as it represents the average magnetic moment contained in a given volume. This field can therefore be expressed in the following form $H_{med} = A\,M$ where A is a constant related to the average molecular field and M the magnetization of the material. If now we are interested in an assembly of magnetic moments, such as an assembly of spins immersed in the applied external field, the associated Hamiltonian is written as:

$$\mathcal{H} = \sum_{ij} J_{ij} S_i \cdot S_j - g_i \mu_B H_{app} \sum_i S_i \tag{2.2}$$

where $\mathcal{H}$, S_i, S_j, g_i, μ_B and H_{app} represent the Hamiltonian, spin operator of i-th and j-th sites, gyromagnetic ratio of the i-th moment, the Bohr magnetron and the applied magnetic field, respectively. It follows from this Hamiltonian that if we consider the moment at site i, cut off the external field and consider the identical magnetic moments, we find an average field felt by the magnetic moment i and which is of the form [66]:

$$H_{med} = \frac{1}{g_i \mu_B} \sum_{ij} J_{ij} S_j \tag{2.3}$$

This model is able to explain the existence of the ferromagnetic order in matter. This leads to an implicit definition of the magnetization in a ferromagnetic material as the average of the magnetic moments present in a given volume and is calculated as follows:

$$\overrightarrow{M} = \sum_i \frac{\overrightarrow{m}_i}{V} \tag{2.4}$$

where $\vec{M}$, $\vec{m}_i$ and V are the magnetization, the ith magnetic moment and the volume considered, respectively. Two important properties also describe ferromagnetic materials and it is essential to introduce them and give their description. These are magnetic susceptibility and magnetic permeability. Magnetic permeability is the ability of certain materials to deflect the lines of a magnetic field. In other words, this property reflects the ability of certain materials to increase or decrease the magnetic induction within the magnetic material under consideration. The relationship between the magnetic field and the magnetic induction (or magnetic density flux) is given by:

$$\vec{B} = \mu_0(\vec{H} + \vec{M}) \tag{2.5}$$

which can be written also in the following form:

$$\vec{B} = \mu \overrightarrow{H} = \mu_0 \mu_r \overrightarrow{H} \tag{2.6}$$

where $\vec{B}$, $\vec{H}$, μ, μ_0 and μ_r represent the magnetic induction vector, the excitation magnetic field, the absolute magnetic permeability, the vacuum permeability and the relative permeability, respectively. Magnetic permeability can be a scalar value in the case of isotropic medium or a tensorial quantity otherwise. Magnetic susceptibility measure the response of a given material immersed in an external magnetic field and reflects the alignment ratio of the magnetic moments (magnetization) with the magnetic field or against his direction. The magnetization is related to the applied magnetic field by the magnetic susceptibility *via:*

$$\vec{M} = \chi \vec{H} \tag{2.7}$$

Substituting this last equation and equation 2.5, the magnetic density flux takes the following form:

$$\vec{B} = \mu_0(1 + \chi)\vec{H} \tag{2.8}$$

Then, the relative magnetic permeability (μ_r), which is a dimensionless entity, is equal to $1+\chi$. We will now look at the different interactions and energies in order to use them in the description of the magnetization static and dynamic properties.

2.1.1.1 Energies and interactions

The energies prevailing in a ferromagnetic medium are the Zeeman energy, the exchange energy, the magnetostatic energy, the magnetocrystalline anisotropy energy and the magnetoelastic energy. Of course, we have focused on the main energies encountered in the various studies discussed here, but other terms can be included like interfaces and free surfaces terms and other effects. The global expression of energy is given by [62]:

$$F = F_{Zee} + F_{dem} + F_{ani} + F_{exch} \tag{2.9}$$

where F_{Zee}, F_{dem}, F_{ani}, F_{exch} represent the Zeeman, demagnetizing, anisotropy and exchange energy contributions, respectively.

Zeeman interaction energy This interaction reflects the behavior of elementary magnetic moments (spin), in this case magnetization (macrospin approximation), in presence of an external magnetic field $\vec{H}$. The energy of Zeeman takes the following form:

$$F_{Zee} = -\vec{H} \cdot \vec{M} \tag{2.10}$$

The exchange interaction This interaction is responsible of the magnetic order and this by aligning magnetic moments in parallel way giving rise to ferromagnetism (or antiparallel of the latter i.e. antiferromagnetism). This interaction originates from quantum effects and has no analog from the classical point of view due to the indescernability of the electrons carrying the magnetic moments. The exchange interaction is divided into two variants according to the distance between two neighboring magnetic moments. The first variant is the direct exchange that is encountered when the interaction occurs directly between the two moments in question without an intermediate atom. In the case of the second variant, called indirect exchange which occurs through another atom, the weak overlap of the respective wave functions of the magnetic moments means that the indirect exchange remains the predominant interaction and occurs through another atom. The predominant exchange interaction during this thesis was the direct exchange. As introduced previously, the direct exchange comes from the direct overlap between the electronic wave functions of neighboring atoms. Because of the fermionic nature of electrons, the principle of exclusion of Pauli must be respected. As a consequence, the wave functions are therefore antisymmetric. In the simple case of two neighboring electrons, the exchange energy can be expressed by the effective Hamiltonian H_{spin} given by the expression [66, 67]:

$$H_{spin} = -2J\,\vec{S}_1 \cdot \vec{S}_2 \tag{2.11}$$

where $\vec{S_1}$ and $\vec{S_2}$ are the angular spin moments of the atoms of the site i and j. J represents the overlapping integral, also called the exchange constant. In the case of a solid, in a discretization approach, this energy is expressed by the Heisenberg model whose Hamiltonian is given by:

$$H = \sum_{ij} J_{ij} \vec{S_i} \cdot \vec{S_j} \tag{2.12}$$

where J_{ij} represents the exchange constant between the spins of sites i and j. ans as a first approximation (interaction between first neighbors), on can write:

$$J_{ij} = \begin{cases} J & \text{Close neighbors} \\ 0 & \text{Otherwise} \end{cases} \tag{2.13}$$

The alignment of the spins in a magnetic material depends on the sign of the exchange integral (constant). In the case of a positive overlapping integral, a parallel alignment of the spins is favored, which gives rise to ferromagnetism if the moments have the same modulus. A negative overlapping integral favors an antiparallel alignment of the spins (antiferromagnetism or ferrimagnetism). In the micromagnetic theory, the energy related to this interaction takes the following form:

$$F_{exch} = \frac{A_{ex}}{M_s^2}\left(\left(\vec{\nabla}M_x\right)^2 + \left(\vec{\nabla}M_y\right)^2 + \left(\vec{\nabla}M_z\right)^2\right) \tag{2.14}$$

where A_{ex}, M_x, M_y and M_z are the exchange stiffness and the different components of the magnetization.

The magnetostatic magnetic interaction Magnetostatic energy is the part of the magnetic excitation created by within the framework of Maxwell's equations. This interaction can act inside a finite size ferromagnetic object through a demagnetizing or outside the ferromagnetic object through the stray field. This contribution is global and can radiate outside the ferromagnetic medium. Thus, unlike the other contributions coming from magnetization, this contribution is not zero outside the medium. This energy is expressed using the demagnetizing field H_{dem} and can be written as[62]:

$$\delta F_{dem} = -\frac{1}{2}\int \vec{H}_{dem} \cdot \vec{M} \tag{2.15}$$

with

$$\vec{H}_{dem} = -\iiint \mathrm{div}\vec{M}\frac{\vec{OP}}{\left\|\vec{OP}\right\|^3}\mathrm{d}V + \iint \vec{n}\cdot\vec{M}\frac{\vec{OP}}{\left\|\vec{OP}\right\|^3}\mathrm{d}S \tag{2.16}$$

where V and S correspond to the volume and area of the ferromagnetic medium, $\vec{n}$ is the normal vector, O is the point where the magnetic volume element is located and P is a variable point. This field satisfies Maxwell's equations. As a consequence, the demagnetizing field can be view in term of virtual "free charges" which appear where the normal component of magnetization points to the discontinuous interfaces (magnetic medium-vacuum medium for instance). These "free charges" with a volume density $\rho = -\nabla\cdot\vec{M}$ and a surface density $\sigma = \vec{M}\cdot\vec{n}$ induce a demagnetizing field opposing the direction of magnetization. In general, this demagnetizing field is uniform neither in direction nor in amplitude in the volume of the medium. It strongly depends on the shape of the medium. Thus, this demagnetizing field can only be calculated easily in the case of uniformly magnetized ellipsoidal objects ($\mathrm{div}\vec{M} = 0$). In this last case the demagnetizing field is written[62, 68]:

$$\vec{H}_{dem} = -4\pi\bar{\bar{N}}\vec{M} \tag{2.17}$$

where $\overline{\overline{N}}$ is the demagnetization tensor[69]. When the main axes of the ellipsoid coincide with those of the coordinate system, the demagnetization tensor is diagonal with $N_{xx} + N_{yy} + N_{zz} = 1$. The energy density associated with the demagnetizing field can then take the form[62]:

$$F_{dem} = 2\pi(N_{xx}M_x^2 + N_{yy}M_y^2 + N_{zz}M_z^2) \tag{2.18}$$

The magnetocrystalline anisotropy Magnetocrystalline anisotropy expresses the fact that the spontaneous configuration of a material depends on the crystal structure. This anisotropy is the direct consequence of the spin-orbit interaction that gives rise to a direction that minimizes the internal energy of the system. This is called the easy axis of magnetization. Indeed, experimentally, it is observed that it is more difficult to magnetize a single crystal sample in certain crystallographic directions than in others. This anisotropy reflects the existence of energy terms depending on the orientation of the magnetization with respect to the crystalline axes. The physical origin of this anisotropy is attributed to the spin-orbit coupling. The atomic orbits, disturbed by the ionic environment, are linked to the crystal lattice. Through the spin-orbit coupling, the spins are also linked to the lattice. It is usual to develop magnetocrystalline anisotropy as a function of the magnetization orientation. As an example, the form of the magnetocrystalline energy term in the case of hexagonal crystals can be written as[62, 70]:

$$F_{ani} = K_1 \sin^2\theta + K_2 \sin^4\theta + K_3 \sin^6\theta + K_3 \sin^6\theta \sin 6\varphi \tag{2.19}$$

where θ and φ are the usual spherical angles, the polar axis being chosen parallel to the c axis of the crystal. Constants K_i are called magnetocrystalline anisotropy constant and are expressed in J/m^3.

Magneto-elastic anisotropy The overwhelming majority of ferromagnetic materials are sensitive to the strain. This effect can be described using a magnetoelastic anisotropy energy term which microscopic origin is also the spin-orbit coupling. It is due to the coupling between the magnetization and the deformations of the crystal lattice. This magnetoelastic anisotropy is found, for example, in epitaxial thin films. Indeed, in order to adapt to the substrate, the lattice of the crystal deforms thus generating a magnetoelastic field within the film. This energy is written as the doubly contracted product of the stress tensor ($\overline{\overline{\sigma}}$) and the magnetic strain tensor ($\overline{\overline{\varepsilon}}_{mag}$):

$$F_{me} = -\overline{\overline{\sigma}} : \overline{\overline{\varepsilon}}_{mag} \tag{2.20}$$

It should be noted that the magnetoelastic strain tensor $\overline{\overline{\varepsilon}}_{mag}$ is that resulting from the so-called direct magnetostriction and depends on the direction of the magnetization. In the case of an isotropic medium (which is the case for all the systems studied during this thesis), the expression of this strain is quite simple:

$$\overline{\overline{\varepsilon}}_{mag} = \begin{pmatrix} \lambda & 0 & 0 \\ 0 & -\frac{\lambda}{2} & 0 \\ 0 & 0 & -\frac{\lambda}{2} \end{pmatrix} \tag{2.21}$$

λ being the magnetostriction coefficient at saturation which can be positive or negative. This coefficient is worth some 10^{-6} in transition metals. It is unitless because it is the deformation of the magnetic material when it is subjected to a magnetic field. Thus, in the case of an isotropic medium, there is only one magnetostriction coefficient. Finally, it is interesting to note that there are homogenization methods (Voight and Reuss for example) making it possible to determine effective magnetostriction coefficients in heterogeneous media from the magnetostriction coefficients of solid materials. In reality, the isotropic case is only a special case of these homogenization methods. We will come back to this magnetoelastic energy during the presentation of our model that combines magnetic and mechanical effects.

2.1.1.2 Magnetization equilibrium

Equilibrium is an important concept in materials and in physics in general. Indeed, every physical system tends towards an equilibrium configuration that minimizes its entropy. Two equilibria can be found in nature, stable and unstable equilibrium situations. Magnetic systems do not escape this universal law. We will therefore focus on the study of equilibrium in a ferromagnetic layer and then move on to the study of the magnetization dynamics in the next subsection. We have introduced the different energies that can be encountered in a ferromagnetic material. The equilibrium in question here depends of course on the competition between the different terms introduced and the minimization of the total energy. Indeed, the different energy terms that we have just introduced make it possible to determine the static equilibrium configurations of the magnetic moments by minimizing the free total energy of the system. This is only done analytically in a few special cases. One of the approaches making it possible to determine an equilibrium configuration is to search for a local minimum for the free energy with the constraint $\vec{M}^2 = M^2$ (fixed norm of the magnetization). A Lagrange multiplier λ_L is used for this purpose[71]:

$$L = F + \lambda_L \left(\vec{M}^2 - M^2 \right) \tag{2.22}$$

The equilibrium configuration is then obtained by deriving this last equation by $\vec{M}$ (Euler-Lagrange equation)[62]:

$$2\lambda_L \vec{M} = -\left(\frac{\partial F}{\partial \vec{M}} \right) \tag{2.23}$$

This equation reflects the fact that the functional gradient of the energy is aligned with the functional gradient of the constraint. The right-hand term of this equation has the size of a magnetic field and is called effective magnetic field ($\vec{H}_{eff}$). This effective magnetic field can be considered as the functional derivative of the energy with respect to the magnetization:

$$\vec{H}_{eff} = -\frac{\partial F}{\partial \vec{M}} \tag{2.24}$$

Thus, we can define an anisotropy field, an exchange field, a demagnetizing field, a Zeeman field, ... At equilibrium, at any point of the medium, we have the following

relation:

$$\vec{H}_{eff} \times \vec{M} = \vec{0} \tag{2.25}$$

Thus, the magnetization and this effective field are collinear at all points. In addition, at equilibrium, in the vicinity of the surface, the magnetization satisfies the following relation:

$$\vec{M} \times \left(\vec{n} \cdot \vec{\nabla}\right) \vec{M} = \vec{0} \tag{2.26}$$

As the norm of the magnetization is constant, we necessarily have $\vec{M} \cdot \left(\vec{n} \cdot \vec{\nabla}\right) \vec{M} = 0$. We then deduce that in the vicinity of the surface of a free surface, the magnetization must remain stationary:

$$\left(\vec{n} \cdot \vec{\nabla}\right) \vec{M} = \vec{0} \tag{2.27}$$

To be more complete, in presence of a surface contribution to the total energy, the previous condition is modified. For example, an energy density related to an anisotropy can take the following form:

$$F_{sur} = K_S \left(1 - \frac{\left(\vec{n} \cdot \vec{M}\right)^2}{M^2}\right) \tag{2.28}$$

And the condition 2.27 becomes:

$$\frac{\partial \vec{M}}{\partial n} = K_S \left(\vec{n} - \left(\vec{n} \cdot \vec{M}\right) \cdot \vec{M}\right) \tag{2.29}$$

Finally, the magnetization distribution of a material depends on the competition between the various energetic contributions previously mentioned without forgetting of course to take into account the external shape of the object which intervenes through the boundary conditions and the demagnetizing field. We observe that at zero applied magnetic field, these contributions are invariant by any transformation which changes the sign of the magnetization vector. Thus, knowing a state of equilibrium, we deduce a second one. These equilibrium configurations which correspond to the local minima of the energy can be manipulated from one state to another by application (among others) of an external magnetic field. This continuous passage will present a discontinuity for certain critical values of the magnetic field. Consider a magnetic structure at equilibrium approaching a critical field. For this field, the state of equilibrium remains a local minimum but it is no longer a minimum minimorum. It thus becomes a state of unstable equilibrium. An infinitesimal disturbance of the system can move away from this state to the point of ending up in a different stable state. We then speak of magnetization reversal. The type of reversal depends on the magnetic configuration of the structure. Depending on whether the magnetization is uniform or not, two processes will guide this phenomenon which will result either in large-amplitude rotations of the magnetization or in domain walls propagation. Several configurations then exist in order to minimize the energy of the system.

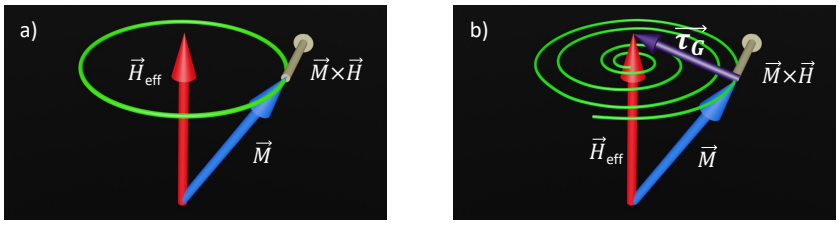

Figure 2.3: Sketch of the magnetization oscillation and the different torques. a) Larmor precession of the magnetization around the effective magnetic field. b) The magnetization oscillation around the effective magnetic field and the effect of the Gilbert damping represented here by the damping torque vector $\vec{\tau_G}$.

2.1.1.3 Magnetization dynamics: Landau-Lifshitz-Gilbert equation

Let us take a look at the equation governing the movement of magnetization over time. If we consider a magnetic moment $\vec{m}$ subjected to a magnetic field $\vec{H}$, its energy density is described by the Zeeman coupling and is written:

$$F_{Zee} = -\vec{m} \cdot \vec{H} \tag{2.30}$$

Let us denote by $\vec{c}$ the torque exerted by the magnetic field on the magnetic moment, this torque is then equal to:

$$\vec{c} = -\vec{m} \times \vec{H} \tag{2.31}$$

If we call $\vec{\ell}$ the angular momentum associated with this magnetic moment, the equation of motion is written using the angular momentum theorem:

$$\frac{\mathrm{d}\,\overrightarrow{\ell}}{\mathrm{d}t} = \overrightarrow{c} \tag{2.32}$$

In an approach of continuous medium (by averaging the previous equation), one can write:

$$\frac{\mathrm{d}\,\overrightarrow{L}}{\mathrm{d}t} = \vec{M} \times \vec{H}_{eff} \tag{2.33}$$

Where $\overrightarrow{L}$ is the angular momentum per unit volume. We also know that these two quantities are linked to each other by the gyromagnetic factor (γ):

$$\overrightarrow{L} = -\frac{1}{\gamma}\vec{M} \tag{2.34}$$

Here γ is the absolute value of the gyromagnetic factor of the material γ_0 which is written as a function of Landé's factor g (dimensionless), of the mass m and the charge of the particle $\gamma_0 = -\frac{g|e|}{2m}$. Magnetization is considered as a local density of magnetic moments whose contributions are orbital or spin. For ferromagnetic materials like Fe, Ni , Co... this contribution is essentially due to the spins, so the factor g will be close to that of an

electron, itself close to 2[72]. If we take into account all the contributions to energy, we thus end up with an equation of motion written[62, 63, 73, 74]:

$$\frac{\mathrm{d}\overrightarrow{M}}{\mathrm{d}t} = -\gamma \vec{M} \times \vec{H}_{eff} \tag{2.35}$$

This equation was established by Landau and Lifshitz for the case of ferromagnetic materials and is thus based on the gyromagnetic effect. For a constant effective field, the magnetization precess uniformly around this field at a natural frequency called Larmor $\omega_{Lar} = \gamma H_{eff}$[75] (see figure 2.3-a). This equation being conservative, it is noted that this motion in no way leads to the minimum energy situation which is an alignment of the magnetization according to the effective field ($\vec{H}_{eff} \times \vec{M} = \vec{0}$). In order for the magnetization to reach the stable thermodynamic equilibrium state, it is necessary to introduce a dissipation mechanism describing the interaction with the crystalline environment. Gilbert then introduces in a phenomenological way a second term in the equation of motion which tends to align the magnetization according to the effective field[76, 77]:

$$\frac{\mathrm{d}\overrightarrow{M}}{\mathrm{d}t} = -\gamma \vec{M} \times \vec{H}_{eff} + \frac{\alpha}{M_S} \vec{M} \times \frac{\mathrm{d}\overrightarrow{M}}{\mathrm{d}t} \tag{2.36}$$

This second term corresponds to the energy dissipation and is characterized by the dimensionless Gilbert damping coefficient (α). In presence of α[1] the solution of the LLG equation reveals a second characteristic time (in addition to the Larmor frequency), the relaxation time that is equal to $\tau = \frac{1+\alpha^2}{\alpha\omega_L}$. On the other hand, the frequency is slightly modified and becomes $\omega = \frac{\omega_L}{1+\alpha^2}$. The illustration of this addition torque is schematically represented in figure 2.3-b). Finally, geometrically, we see that to bring the magnetization back to the effective field, the dissipation term must be oriented along the meridian. The movement resulting from the precession term and the dissipation term is a spiral described on the sphere $\vec{M}^2 = M^2$ (see figures 2.3-a) and -b)). The expression of movement can also be written as resolved[62]:

$$\frac{\mathrm{d}\overrightarrow{M}}{\mathrm{d}t} = -\frac{\gamma}{1+\alpha^2} \vec{M} \times \vec{H}_{eff} + \frac{\gamma\alpha}{M_S\left(1+\alpha^2\right)} \vec{M} \times \vec{M} \times \vec{H}_{eff} \tag{2.37}$$

2.1.1.4 Small magnetization oscillations

During this thesis, the magnetization dynamic is treated by considering small oscillations of the magnetization around an equilibrium position. The magnitudes which are the magnetization and the effective field are thus broken down into a static part and into a dynamic part assumed to be much smaller than the previous one:

$$\begin{aligned} \vec{M}(t) = &\quad \vec{M} + \vec{m}e^{i\omega t} \\ \vec{H}_{eff}(t) = &\quad \vec{H}_{eff} + \vec{h}_{eff}e^{i\omega t} \end{aligned} \tag{2.38}$$

[1] The order of magnitude of α is 0.01 in most ferromagnetic materials.

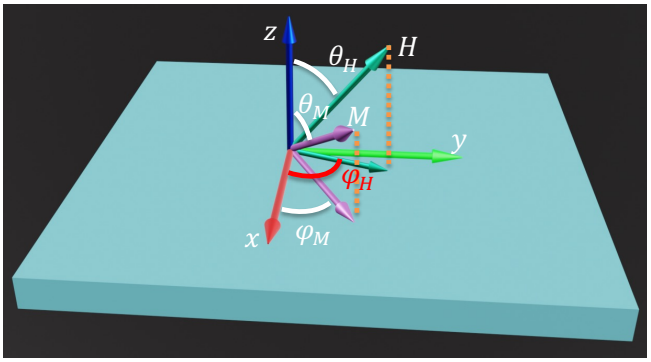

Figure 2.4: Space spherical coordinates system and the representation of the magnetization and effective magnetic field

with $m(t) \ll M$ and $h(t) \ll H_{eff}$. Assuming that the motion is not attenuated, the linearized Landau-Lifshitz equation without dissipation ($\alpha = 0$) can be written as:

$$\frac{i\omega}{\gamma}\vec{m} = -\vec{M} \times \vec{h}_{eff} - \vec{m} \times \vec{H}_{eff} \tag{2.39}$$

We suppose indeed that $\vec{m} \times \vec{h}_{eff}$ is negligible and that $\vec{M} \times \vec{H}_{eff} = 0$. One of the direct consequences of this expression is that the dynamic and static components of the magnetization are perpendicular to each other: $\vec{m} \perp \vec{M}$ [2]. Let us consider an effective magnetic field along the Oz axis and the saturation magnetization aligned in the same direction. The conservation criteria and the fact that the amplitude of the dynamic components of both magnetic field and magnetization are very small, the Landau-Lifshitz takes the form:

$$i\omega m_x + \gamma H_{eff} m_y = -\gamma M h^y_{eff} \tag{2.40}$$

$$-\gamma H_{eff} m_x + i\omega m_y = \gamma M h^x_{eff} \tag{2.41}$$

The component $\vec{m}$ and $\vec{h}_{eff}$ are linked by the high-frequency magnetic susceptibility $\overline{\overline{\chi}}$ (Polder tensor)[78]:

$$\vec{m} = \overline{\overline{\chi}}\, \vec{h}_{eff} = \begin{pmatrix} \chi & i\chi_a \\ -\chi_a & \chi \end{pmatrix} \begin{pmatrix} h^x_{eff} \\ h^y_{eff} \end{pmatrix} \tag{2.42}$$

In the precedent equations, on can notice that if $\omega \to \gamma H_{eff}$, χ and χ_a grow unlimitedly. Taking the magnetic damping into consideration will avoid this phenomenon by transforming χ and χ_a into complex quantities: $\chi = \chi' + i\chi''$ and $\chi_a = \chi'_a + i\chi''_a$. Figure 2.5 shows the variation of the real and imaginary parts of the Polder tensor $\overline{\overline{\chi}}$ as function of an applied magnetic field. The real part change in sign, while the imaginary parts pass through maxima at the resonance. The resonance condition is given by :

$$\omega_{res} = \frac{\gamma H_{eff}}{1 + \alpha^2} \tag{2.43}$$

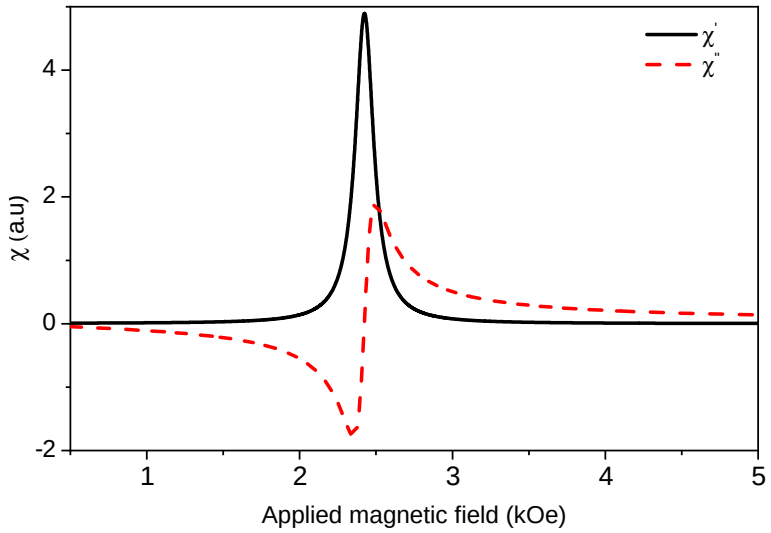

Figure 2.5: The real (solid line) and the imaginary (dashed line) part of the complex hf susceptibility.

The imaginary part of the magnetic susceptibility $\chi^{"}$ characterizes the energy absorption that appears in a ferromagnetic system due to excitation by a microwave field. The absorbed microwave power, P_{rf} in a ferromagnetic thin film, is then defined as:

$$P_{rf} = \frac{1}{2}\omega Im\left[\chi\right]|h_{rf}|^2 \tag{2.44}$$

2.1.1.5 Uniform precession mode

In this paragraph, we consider a uniformly magnetized material. If, moreover, the effective field, here its dipolar component, is also uniform in the material (which imposes a constraint on the shape of the sample) then a spatially uniform precession of the magnetization can be established around the effective field corresponding to the gyromagnetic mode. It is neither more nor less of the precession of the magnetic moment following a cone whose axis corresponds to the constant effective field. Obtaining an expression of the resonant frequency of this excited mode, commonly called uniform precession mode, can be done by considering small oscillations of the magnetization around its equilibrium position. The goal here is to express the equation describing the magnetization motion in spherical coordinates. In spherical coordinates, in which the magnetization is identified by its zenith and azimuth angles (see figure 2.4). In this system, the unit vectors are:

$$\overrightarrow{e}_r = \begin{pmatrix} \sin\theta_M \cos\varphi_M \\ \sin\theta_M \sin\varphi_M \\ \cos\theta_M \end{pmatrix}; \overrightarrow{e}_\theta = \begin{pmatrix} \cos\theta_M \cos\varphi_M \\ \cos\theta_M \sin\varphi_M \\ -\sin\theta_M \end{pmatrix}; \overrightarrow{e}_\varphi = \begin{pmatrix} -\sin\varphi_M \\ \cos\varphi_M \\ 0 \end{pmatrix}$$

[2]Indeed, $\frac{i\omega}{\gamma}\vec{m}\cdot\vec{M} = \left(-\vec{M}\times\vec{h}_{eff} - \vec{m}\times\vec{H}_{eff}\right)\cdot\vec{M} = -\left(\vec{M}\times\vec{M}\right)\cdot\vec{h}_{eff} - \left(\vec{H}_{eff}\times\vec{M}\right)\cdot\vec{m} = 0.$

The magnetization motion (see equation 2.35) is described by its position and and velocity:

$$\vec{M} = M\left(\sin\theta_M\cos\varphi_M\vec{e}_x + \sin\theta_M\sin\varphi_M\vec{e}_y + \cos\theta_M\vec{e}_z\right) = M\vec{e}_r \tag{2.45}$$

$$\frac{\mathrm{d}\overrightarrow{M}}{\mathrm{d}t} = M(\dot{\theta}_M\vec{e}_\theta + \dot{\varphi}\sin\theta_M\vec{e}_\varphi) \tag{2.46}$$

The effective field ($\vec{H}_{eff}$) takes the following form:

$$\vec{H}_{eff} = -\nabla_{\vec{M}}F = -\frac{1}{M_S}\left(F\vec{e}_r + \frac{\partial F}{\partial\theta_M}\overrightarrow{e}_\theta + \frac{1}{\sin\theta_M}\frac{\partial F}{\partial\varphi_M}\overrightarrow{e}_\varphi\right) \tag{2.47}$$

The incorporation of the effective field expression and the temporal derivative of magnetization in the equation2.35 gives the following form:

$$M\begin{pmatrix}0\\ \dot{\theta}\\ \dot{\varphi}\sin\theta_M\end{pmatrix} = -\gamma\begin{pmatrix}0\\ \frac{1}{\sin\theta_M}\frac{\partial F}{\partial\varphi_M}\\ -\frac{\partial F}{\partial\theta_M}\end{pmatrix} + \frac{\alpha}{M_S}\begin{pmatrix}0\\ -M^2\ \dot{\varphi}\sin\theta_M\\ \dot{\theta}M^2\end{pmatrix} \tag{2.48}$$

at the equilibrium position the derivative terms tends to zero ($\frac{\partial F}{\partial\theta_M} = \frac{\partial F}{\partial\varphi_M} = 0$). Let us now consider a small perturbations nearby the equilibrium angles (θ_{eq} and φ_{eq}) representing a small oscillation of the magnetization at this position. Let us replace the partial derivative forms by the following notation: F_ξ with $\xi = \theta, \varphi$. The minimization related to the perturbation is of the form:

$$\begin{aligned}\delta F_\theta &= \partial_\theta F_\theta\delta\theta(t) + \partial_\varphi F_\theta\delta\varphi(t)\\ \delta F_\varphi &= \partial_\varphi F_\varphi\delta\varphi(t) + \partial_\theta F_\varphi\delta\theta(t)\end{aligned} \tag{2.49}$$

where $\delta\theta(t)$ and $\delta\varphi(t)$ represent the perturbations around the equilibrium position: $\delta\theta(t) = \theta(t) - \theta_{eq} = \delta\theta e^{-i\omega t}$ and $\delta\varphi(t) = \varphi(t) - \varphi_{eq} = \delta\varphi e^{-i\omega t}$. Because $\alpha << 1$, one can neglect the squared damping terms in the formulation. Considering these conditions, one can write:

$$\begin{aligned}\dot{\theta} &= -\frac{\gamma}{M\sin\theta}\frac{\partial F}{\partial\varphi} - \frac{\alpha\gamma}{M_S}\frac{\partial F}{\partial\theta}\\ \dot{\varphi} &= \frac{\gamma}{M\sin\theta}\frac{\partial F}{\partial\theta} - \frac{\alpha\gamma}{M_S\sin^2\theta}\frac{\partial F}{\partial\varphi}\end{aligned} \tag{2.50}$$

By incorporating equations 2.49 in equation 2.50, one can write:

$$\begin{aligned}-\tfrac{1}{\gamma}M\dot{\theta}\sin\theta &= F_{\varphi\theta}\delta\theta + F_{\varphi\varphi}\delta\varphi\\ \tfrac{1}{\gamma}M\dot{\varphi}\sin\theta &= F_{\theta\theta}\delta\theta + F_{\theta\varphi}\delta\varphi\end{aligned} \tag{2.51}$$

The previous system admits a non-trivial solution if and only if its determinant is zero. The natural frequency of this system corresponds to the resonant frequency of the uniform mode. Finally, if one neglect the losses ($\alpha = 0$), we obtain the Smith-Beljers equation[79, 80]:

$$\left(\frac{\omega}{\gamma}\right)^2 = \left(\frac{1}{M\sin\theta}\right)^2\left(\frac{\partial^2F}{\partial\theta^2}\frac{\partial^2F}{\partial\varphi^2} - \left(\frac{\partial^2F}{\partial\theta\partial\varphi}\right)^2\right)_{\theta_{eq},\varphi_{eq}} \tag{2.52}$$

The presence of dissipation ($\alpha \neq 0$) leads to a complex form of $\omega = \omega' + \omega$". The real part corresponds to the previous relation and the complex part can be written as[62]:

$$\frac{\omega"}{\gamma} = \frac{\alpha}{2M}\left(\frac{\partial^2F}{\partial\theta^2} + \frac{1}{\sin^2\theta}\frac{\partial^2F}{\partial\varphi^2}\right)_{\theta_{eq},\varphi_{eq}} \tag{2.53}$$

Thus knowing the form of the energy, it is possible for us to know the orientation of the magnetization (equation 2.51) and the resonance frequency (equation 2.52). In the case of materials of ellipsoidal shape whose main axes coincide with those of the reference frame, by considering a saturating magnetic field applied in the direction Oy, the resonance frequency is given by Kittel's formula [81]:

$$\left(\frac{\omega_R}{\gamma}\right)^2 = \left(H + \left(N_z - N_y\right) M\right)\left(H + \left(N_x - Ny\right) M\right) \tag{2.54}$$

This resonance is not sustainable. The magnetization is gradually aligned according to the direction of the effective field after having carried out a spiral movement around this same field. Its gradual alignment is due to the dissipative effects. To maintain the precession, it is necessary to compensate for the losses by a radiofrequency magnetic excitation of frequency ω_{rf}. The coupling between the radiofrequency field and the magnetization is optimum for $\omega_{rf} = \omega_R$, which defines magnetic resonance. This is the principle of the ferromagnetic resonance technique, a technique that we will detail in the next chapter and that we have intensively used during this thesis.

2.1.1.6 Spin waves in thin films

The notion of spin waves was first introduced by Bloch who showed that the low energy excitations of the Heisenberg Hamiltonian are states in which the reversal of a spin is delocalized on all the lattice: a spin wave is characterized by its wave vector k and its pulsation $\omega(\vec{k})$ (i.e. in a quantum context, its energy $\hbar\omega(\vec{k})$). In this subsection, we will first present the case of the so-called magnetostatic spin waves and then briefly present spin waves in the exchange regime in the context of a thin film uniformly magnetized in its plane and in absence of anisotropy (magnetocrystalline and magnetoelastic). In these conditions, we suppose an infinite thin film in the plane Oxy and bounded by a thickness d according to the direction z. Finally, an external magnetic field is applied along y.

Magnetostatic spin waves (either by neglecting the exchange contribution or by taking into account this exchange with an approximation)
Under the magnetostatic regime assumption, the currents associated with field fluctuations are neglected (the electrical and magnetic variables are decoupled). Under this assumption, one can write:

$$\vec{\nabla} \times \vec{h}_{dem} = \vec{0} \tag{2.55}$$

where $\vec{h}_{dem}$ is the dynamical part of the demagnetizing field. In addition, the magnetization of the material and the demagnetizing field present within the film obey the Maxwell equation:

$$\vec{\nabla} \cdot \vec{b} = \vec{\nabla} \cdot \left(\vec{h}_{dem} + 4\pi\vec{m}\right) = 0 \tag{2.56}$$

$\vec{b}$ being the oscillating magnetic induction field. Equation 2.55 makes it possible to introduce the magnetostatic potential (ϕ) linked to the demagnetizing field by the relation:

$$\vec{h}_{dem} = \vec{\nabla}\phi \tag{2.57}$$

In these conditions, equation 2.56 takes the following form:

$$\Delta\phi + 4\pi\vec{\nabla}\cdot\vec{m} = 0 \tag{2.58}$$

We now consider that the magnetic potential takes the following form:

$$\phi(x,y,z,t) = \phi(z)e^{-i(k_x x + k_y y)}e^{i\omega t} \tag{2.59}$$

As previously mentioned, an external magnetic field is applied along y, thus the static magnetization $\vec{M}$ is aligned along y. The linearized Landau-Lifshitz relation (see equation 2.39) makes it possible to determine the components of the dynamic magnetization:

$$\begin{pmatrix} m_x \\ m_y \end{pmatrix} = \begin{pmatrix} i\alpha_2 & \alpha_1 \\ \alpha_1 & i\alpha_2 \end{pmatrix} \begin{pmatrix} \partial_z\phi \\ ik_y\phi \end{pmatrix} \tag{2.60}$$

where $\alpha_1 = \frac{HM}{H^2-\Omega^2}$; $\alpha_2 = \frac{H\Omega}{H^2-\Omega^2}$ and $\Omega = \frac{\omega}{\gamma}$. Moreover, equation 2.58 takes the following form[82]:

$$-\left(k_x^2 + \frac{k_y^2}{1+\alpha_1}\right)\phi(z) + \partial_z^2\phi(z) = 0 \tag{2.61}$$

So, one can deduce that the potential is:

$$\phi(z) = \phi_1 e^{Qz} + \phi_2 e^{-Qz} \tag{2.62}$$

where $Q = \left(k_x^2 + \frac{k_y^2}{1+\alpha_1}\right)^{\frac{1}{2}}$. Outside the film, the oscillating field derived from a potential ψ that obey to a Laplace type equation ($\Delta\psi = 0$). To be compatible with the form of the potential inside the film ϕ and in order to remain limited, this potential must take the following form:

$$\begin{aligned} \psi^{<}(x,y,z,t) &= \psi_1 e^{Kz}e^{i(k_x x + k_y y)}e^{i\omega t} \quad \text{for} \quad z < 0 \\ \psi^{>}(x,y,z,t) &= \psi_1 e^{-Kz}e^{i(k_x x + k_y y)}e^{i\omega t} \quad \text{for} \quad z > d \end{aligned} \tag{2.63}$$

where $K = \left(k_x^2 + k_y^2\right)^{\frac{1}{2}}$. The boundary conditions between the film and the exterior express the continuities of $\vec{h}_{dem}^{\parallel}$ and $\vec{b}_{\perp}$. They result in a system of linear equations bearing on the unknowns ϕ_1, ϕ_2, ψ_1 and ψ_2 without second member:

$$\begin{aligned} K\psi_1 &= Q\left(1+4\pi\alpha_1\right)\left(\phi_1-\phi_2\right) - 4\pi\alpha_2 k_y\left(\phi_1+\phi_2\right) \\ -K\psi_2 e^{-Kd} &= Q\left(1+4\pi\alpha_1\right)\left(\phi_1 e^{Qd} - \phi_2 e^{-Qd}\right) - 4\pi\alpha_2 k_y\left(\phi_1 e^{Qd} - \phi_2 e^{-Qd}\right) \\ \psi_1 &= \phi_1 + \phi_2 \\ \psi_2 &= \phi_1 e^{Qd} - \phi_2 e^{-Qd} \end{aligned} \tag{2.64}$$

If this system is invertible, then all the unknowns are zero. A magnetization oscillation only exists if the system is not invertible, i.e. its determinant is zero:

$$K_1 \cdot K_2 = 0 \tag{2.65}$$

with

$$K_1 = (-K + Q(1 + 4\pi\alpha_1) - 4\pi\alpha_2 k_y)(K - Q(1 + 4\pi\alpha_1) - 4\pi\alpha_2 k_y)\, e^{-2Qd} \quad (2.66)$$

$$K_2 = (K + Q(1 + 4\pi\alpha_1) - 4\pi\alpha_2 k_y)(K + Q(1 + 4\pi\alpha_1) - 4\pi\alpha_2 k_y)\, e^{-2Qd} \quad (2.67)$$

MagnetoStatic Surface spin Wave (MSSW) If we consider a wave propagating in the x direction ($k_y = 0$), i.e. perpendicular to the static magnetization, the relation 2.65 takes the following form[83, 84, 85]:

$$\Omega^2 = (H + 2\pi M)^2 - (2\pi M)^2 e^{-2k_x d} \quad (2.68)$$

This relation gives the dispersion of the surface magnetostatic mode, also called Damon Eshbach mode. Relation 2.62 shows that this spin wave has an evanescent character; here we find a justification for its name as surface wave. A significant asymmetry is observed in the shape of the magnetostatic potential associated with the demagnetizing field between the two surfaces of the film. Thus, a spin wave propagating in one direction will be localized near the upper surface and the spin wave propagating in the other direction will be localized near the lower surface. This specificity makes it possible to highlight certain interface effects by playing on the buffer and capping layers (down and top interfaces). This is also how it is possible to measure the so-called Dzyaloshinskii Moriya interaction in magnetic film/non magnetic film systems by measuring the non reciprocity of this spin wave energy.

MagnetoStatic Backward Volume spin Waves (MSBVW) We speak of magnetostatic backward volume wave when we consider waves propagating parallel to the static magnetization direction (i.e. $k_x = 0$). System 2.64 leads to the following relation[86, 85]:

$$\ell = \tan\left(\frac{k_y d}{2\ell}\right) \quad (2.69)$$

where $\ell = (1 + 4\pi\alpha_1)^{\frac{1}{2}}$. It results from equation 2.65 a set of solutions for ℓ from which we can deduce the frequencies from the following relation:

$$\Omega^2 = H^2 + \frac{4\pi M H}{1 + \ell^2} \quad (2.70)$$

The waves associated with these modes have a stationary character in the z direction; hence the name volume waves. Note that the frequency decreases when the wave vector k_y increases, the group velocity is negative. That justifies the denomination of backward waves. Generally, only the lowest mode is studied by ferromagnetic resonance or Brillouin light scattering.

The expressions 2.68 and 2.70 correspond to limit case. In the general case (i.e. $k_x \neq 0$ and $k_y \neq 0$: arbitrary angle between the static magnetization and the direction of the spin wave propagation) it is advisable to find numerically the eigenfrequencies starting from the relation 2.65. Finally, one can note that the MSBVW mode dispersion is less than that of MSSW mode.

MSSW and MSBVW modes in the exchange regime The frequencies of the magnetostatic modes that we have just present were calculated neglecting the exchange constant A. These expressions remain valid as long as the module k of the wave vector is small (i.e. for values of kd lower to about 3). For larger wave vectors, the contribution of the exchange cannot be neglected. Under certain conditions, it is possible to obtain an analytical expression of the natural frequency magnetostatic modes (MSSW and MSBVW) taking into account the exchange. Account given that the magnetic films are thin (a few nanometers), it is convenient to integrate the Landau-Lifshitz and Maxwell equations on the thickness of the film. This approach was introduced by Stamps and Hillebrands and can only concern modes that slightly vary on the thickness of the film[87, 88]; stationary modes of exchange will therefore not be described by this approach. This method is powerful in that it allows to obtain analytical expressions by taking into account other energy terms associated with different phenomena in a fairly simple way. In these conditions, the integration of the linearized Landau-Lifshitz relation can be written as:

$$i\Omega\overline{\vec{m}} = \vec{M} \times \left(\vec{h}_{dem} + -\frac{2A}{M^2} Q^2 \overline{\vec{m}} - \lambda \overline{\vec{m}} \right) \tag{2.71}$$

Where the magnetization oscillation has the form $\vec{m} = \vec{m}(z)e^{i(k_x x + k_y y)}$ and where we have set $Q^2 = (k_x^2 + k_y^2)$. The following convention was chosen: $\overline{f} = \frac{1}{d}\int_0^d f dz$ and $[f] = f(d) - f(0)$. Under these conditions, the demagnetizing field dynamic is written:

$$\vec{h}_{dem} = i\overline{\phi}\vec{Q} + \frac{1}{d}[\phi]\vec{e}_z \tag{2.72}$$

The integration of Maxwell's equation associated with the boundary conditions allows us to determine the following quantities:

$$\overline{\phi} \cong \frac{4\pi i \vec{Q} \cdot \overline{\vec{m}}}{Q(\frac{2}{d} + Q)} \; ; \; [\phi] = \frac{-8\pi m_z}{\frac{2}{d} + Q} \tag{2.73}$$

Note that this only approximation necessary to obtain these two quantities is as follows (strong assumption):

$$\frac{1}{d}\int_0^d \phi(z) dz \simeq \frac{\phi(d) + \phi(0)}{2} \tag{2.74}$$

The integration of the linearized Landau-Lifshitz relation then leads to a homogeneous and linear system on the components of $\overline{\vec{m}}$. This system must not be invertible for the magnetization oscillation to be non-zero. By writing that the determinant of the system is zero, we obtain the eigenfrequencies. Finally, note that when the exchange is taken into account in the calculation of the magnetostatic modes , we see that the MSBVW mode no longer necessarily has a negative group velocity. However, we will keep its name by analogy with the dipolar approximation (i.e. by neglecting A).

Perpendicular stranding spin waves These waves have a wave vector parallel to the normal of the film plane. These waves undergo reflections at the interfaces and enter

a stationary regime, a regime which will depend on the thickness d of the layer and of the pinning conditions[89, 90]. We always consider a uniformly magnetized thin film for which the field is applied in the film plane and suppose that waves propagate in the z direction. Assuming a profile of the form $m(z) = m^+e^{iq_z z} + m^-e^{iq_z z}$ and by writing the previously defined Rado-Weertman conditions, it is possible to determine the frequencies of the stationary modes:

$$\begin{aligned}\left(\frac{\omega}{\gamma}\right)^2 &= \left(H - H_a + \tfrac{2A}{M}(Q^2+k_z^2)(H + \tfrac{2A}{M}(Q^2+k_z^2))\right)\\ &\cdot\left(4\pi M(H + \tfrac{2A}{M}(Q^2+k_z^2) - H_a\left(\tfrac{Q^2}{Q^2+k_z^2}\right)\right)\end{aligned} \tag{2.75}$$

Where we have set $Q^2 = q_x^2 + q_y^2$. $H_a = \frac{2K}{M}$ is a perpendicular anisotropy field defined by the anisotropy constant K. An approximation is made as to the value of k_z. We set $k_z \simeq \frac{n\pi}{d}$ (with n positive integer), which often makes it possible to describe the eigenfrequencies of the stationary modes. We speak of order mode 1,2,3, ... according to the value of n.

2.1.2 Micromagnetic simulations

Till now, magnetic heterogeneities were mentioned in the different analytical expression above which are valid just in the case of homogeneously magnetized films. When studying isolated magnetic nano-object or arrays of magnetic nano-objects such as dots, antidots, nanowires,....; it is only possible to obtain an analytical expression for spin waves at the cost of approximations which are sometimes too unrealistic. Indeed, in the case of a magnetic objects whose dimensionality are reduced, new free surfaces appear and give rise to heterogeneous demagnetizing fields, which *in fine* can lead to non-uniform magnetization distributions. In addition to this heterogeneous magnetization distribution, spectacular effects such as the quantification of some spin wave modes appear. These effects can sometimes be treated satisfactorily analytically. It is for example the case in arrays of rectangular section nanowires for which an approximate analytical modelization captures well the quantization effects if one suppose a uniform magnetization along the nanowire. This is the reason why many experimental studies carried out on arrays of magnetic nano-objects use micromagnetic simulations in order to try to explain or even predict certain phenomena which cannot be interpreted simply in an analytical way. During this thesis, we have employed this philosophy when studying arrays of nanostructures.

For this purpose, we used the OOMMF (Object Oriented Micro Magnetic Framework)[55] software. It allows us to find the equilibrium configurations for a particular geometry and parameters, but also to follow the temporal evolution of this configuration under the effect of an external perturbation (a radio frequency field in the ferromagnetic resonance experiments). The goal here is not to present the code itself by detailing the calculation procedures, we will be satisfied with a fairly brief presentation.

We start by defining our object. In order to keep calculation times reasonable, we have decided to limit ourselves to a small number of nanostructures (a few holes if we take

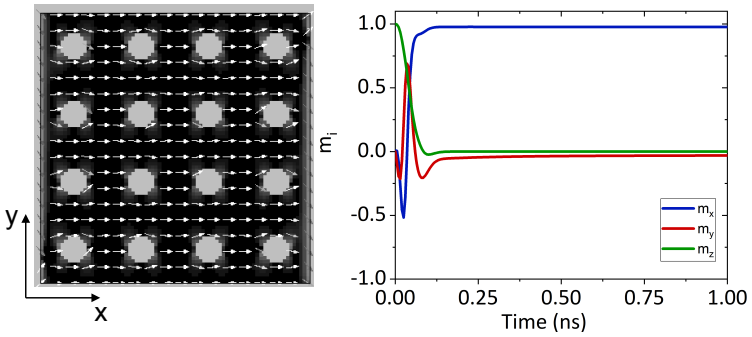

Figure 2.6: Top view of a simulated (finite) array of antidots (4×4 nanoholes of diameter 250 nm and a periodicity of 600 nm). A magnetic field (1150 Oe) is applied along x. Relaxation curves (magnetization components variation as function of time) obtained with $\alpha = 0.5$, the magnetic moments were initial uniformly aligned along z at $t = 0$ ns. After 1 ns of relaxation, the magnetic moments are almost all aligned the applied magnetic field (along x direction). Magnetic parameters are those of permalloy (Ni80Fe20): $M_S = 800$ emu.cm^{-3}, $\gamma/2\pi = 0.003$ GHz.Oe^{-1} and $A = 1 \times 10^{-6}$ erg.cm^{-1}.

the example of an antidot array). The first stage of our work consisted in finding the state of equilibrium of the system studied by taking into account all the energy contributions: exchange, magnetostatic (demagnetizing and dipolar), Zeeman,... Note that the different magnetic parameters (saturation magnetization M_S, gyromagnetic ratio γ and exchange stiffness A) used in the simulations have been systematically (when possible) experimentally obtained either from magnetic resonance measurements or magnetometry measurements performed on a continuous film. Indeed, since we will be interested in the temporal evolution of our magnetic system under the influence of external disturbance (here it will be a small radio frequency magnetic field), it will be a question of determining the evolution of the magnetization according to time by solving the Landau Lifshitz equation at each cubic cell:

$$\frac{\mathrm{d}\vec{M}}{\mathrm{d}t} = -\gamma \vec{M} \times \vec{H}_{eff} + \frac{\alpha}{M_S} \vec{M} \times \frac{\mathrm{d}\vec{M}}{\mathrm{d}t} \tag{2.76}$$

Solving this equation will allow us to determine the equilibrium configurations for different field values. The 3d structure which will be considered each time is broken down into elementary cells within which the different quantities are evaluated. Depending on the exchange length value defined as $\ell_{ex} = \sqrt{\frac{2A}{\mu_0 M_s^2}}$, we will take an elementary cell of dimension $\ell_x \times \ell_y \times \ell_z$ nm^3 with the idea to have $\ell_x = \ell_y = \ell_z \simeq \ell_{ex}$. In this initial step, the LLG equation is generally solved with a damping constant fixed at $\alpha = 0.5$ since only the final equilibrium interests us. As an example, the relaxation curves of an finite array of nanoholes is presented in figure 2.6 where $m_i = M_i/M_s$ (i stands for x, y or z directions and M_s the saturation magnetization). The studied system corresponds to a finite array of antidots (periodicity of 600 nm and nanohole diameter of 250 nm with a thickness of

20 nm). The magnetic moments were initially aligned along z; at $t = 0$ ns a magnetic field is applied along x direction, the final magnetization distribution corresponds to an alignment of the magnetic moments along this field. One can note that the equilibrium state is obtained in less than 1 ns, which is due to the strong Gilbert damping constant.

Actually, the micromagnetic simulations have been performed with the aim to locate the different magnetic modes and to calculate their frequency dependencies as a function of the applied magnetic field. These latter dependencies can be directly compared to the FMR experiments. Indeed, the frequency response of magnetic objects in the low excitation regime is characterized by the susceptibility χ reflecting the linearity between the excitation field and the magnetic response of the object. The dynamic phenomena of magnetization can be treated according to two approaches: a frequency approach or a temporal approach. Frequency approaches are the most often used because historically, with regard to the first experiments with ferromagnetic resonance, we have been led to reason in frequency space. It is a temporal resolution that we will adopt for this study. The approach we used to calculate the dynamic susceptibility spectra is presented in the following. By using a temporal approach, in a homogeneous medium, we can define the magnetization at a given point as a linear function of the magnetic field prior to the instant t of the measurement:

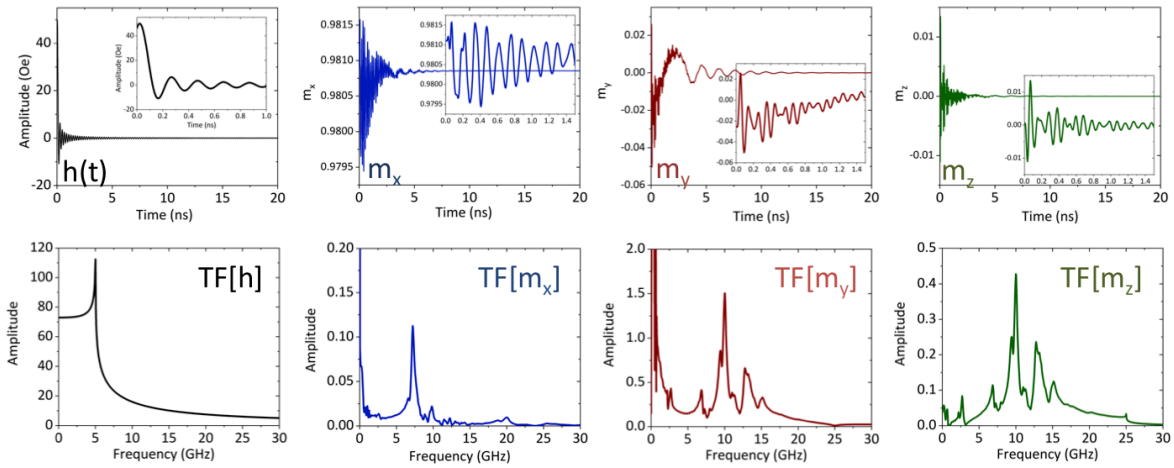

Figure 2.7: Exciting magnetic field presented in the text and corresponding temporal variations of the normalized magnetization components (m_x, m_y and m_z). The bottom graphs are the Fourier transform of the top graphs. This curves have been obtained by applying $h(t)$ to the equilibrium configuration presented in figure 2.6. The scale are not identical in all graphs.

$$\overrightarrow{M} = \int_{-\infty}^{t} \vec{h}(t') f_{\chi}\left(t - t'\right) dt' \tag{2.77}$$

The fact that the magnetization depends only on the antecedent magnetic field is related to the principle of causality. Thus, by setting $f_\chi(t-t')$ for any subsequent time that is $t-t'<0$, the previous integral can be extended to infinity:

$$\overrightarrow{M} = \int_{-\infty}^{+\infty} \vec{h}(t') f_\chi\left(t-t'\right) dt' \tag{2.78}$$

We then see that the magnetization appears as a product of convolution between the magnetic field $h(t)$ and the linear function $f_\chi(t)$. This observation invites us to take the Fourier transforms of these different quantities, we thus have:

$$\tilde{M}(\omega) = \tilde{h}(\omega)\tilde{f}_\chi(\omega) \tag{2.79}$$

By considering the susceptibility as being the Fourier transform of the linear function $f_\chi(t)$, we then define the magnetic susceptibility at the pulsation ω as:

$$\chi(\omega) = \int_{-\infty}^{+\infty} f_\chi(t) e^{i\omega t} \tag{2.80}$$

$\chi(\omega)$ is then the multiplier coefficient connecting $\tilde{h}(\omega)$ and $\tilde{M}(\omega)$:

$$\tilde{M}(\omega) = \tilde{h}(\omega)\chi(\omega) \tag{2.81}$$

All these terms being complex, we can separate them into real and imaginary part. Therefore, the knowledge of the Fourier transforms of the magnetization and of the magnetic field makes it possible to calculate the complex magnetic susceptibility. Wishing to go back to susceptibility, any form of the excitation $h(t)$ is in principle applicable; however it is advisable to choose an excitation which makes it possible to probe the good frequency range. We will take an exciting field of the following form:

$$h(t) = h_0 \mathrm{sinc}\left(2\pi f_{cut}(t-t_0)\right) \tag{2.82}$$

where f_{cut} was fixed at 25 GHz with a sampling frequency $f_s = 200$ GHz giving a Nyquist frequency $f_n = 100$ GHz. This exciting field can be viewed in figure 2.7. So in this second step, the dynamic response of our system is obtained by exciting the system in the equilibrium previously calculated with a short magnetic field pulse applied orthogonally which disturbs the equilibrium state (if it is almost homogeneous). The system can thus relax following the LLG equation with a damping constant fixed at $\alpha = 0.008$. Each dynamic simulation is calculated over 20 ns divided in 4000 stages and each stage is got by mean of the Runge Kutta algorithm. The Fourier transform method was used to get the resonance frequencies related to the different magnetic modes. Figure 2.7 presents a typical example of the obtained temporal variation of the normalized magnetization components when the system is excited using the field $h(t)$ and their respective Fourier transform amplitude. The magnetic system is the one presented in figure 2.6 and the exciting field is thus applied along y. Obviously, the more intense Fourier transform corresponds to TF$[m_y]$ and the less intense Fourier transform component corresponds to

TF[m_x][91], i.e. to the one calculated along the static magnetization $\vec{M}$ (that can be considered as uniform in the present example).

Finally, the Fourier transform method was also used to get the spacial localization of each modes. For this purpose, the spacial absorption at the corresponding frequencies are calculated using the averaged value of each elementary mesh cell over the thickness, since we consider the thickness small enough (here 20 nm) to get uniform distribution of the magnetization over it. Figure 2.8 presents an example of a typical profile mode calculation of the more intense frequency in the spectra presented in figure 2.7.

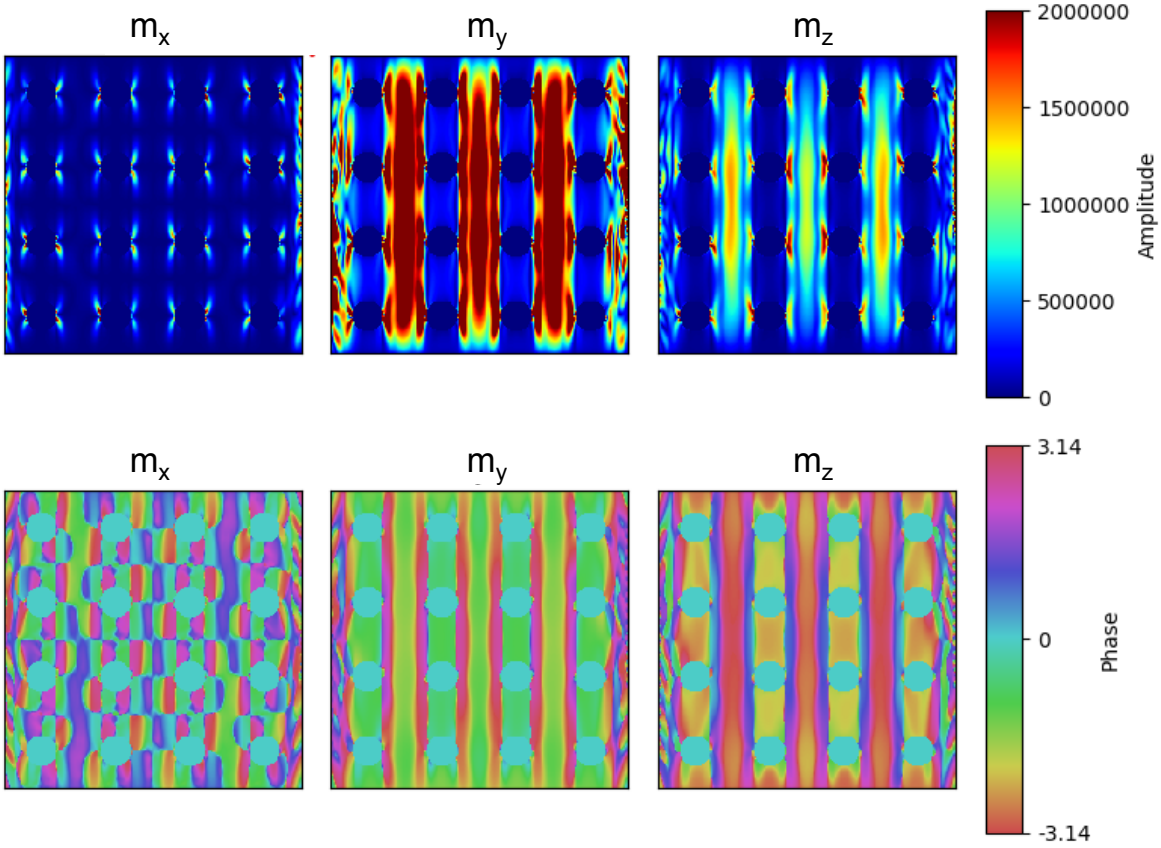

Figure 2.8: Spatially resolved modes in all three cartesian directions plotted over the extent if the system at the more intense frequency. Top row: power spectra for x, y and z component. Bottom row: corresponding phase distribution for the three components.

2.2 Mechanical simulations under COMSOL Multiphysics®

In this section, we discuss the finite element simulations carried out under COMSOL Multiphysics® [92] to evaluate the deformations within nanostructures induced by a ferroelectric actuator. Indeed, all the systems that we have studied consist of a magnetic medium (thin film or array of nanostructures) deposited on a Kapton® substrate. Then, these magnetic medium/Kapton systems were glued onto ferroelectric actuators. Thus, the application of an electric field within the ferroelectric allows the application of strains within the magnetic medium. When the medium is a thin film, we have already shown (during M. Gueye's thesis[**?**]) that the transmission rate of planar strains is 100%; we also confirmed this during this thesis by using the digital image correlation technique (see next chapter). However, when the medium is an array of nanostructures, the planar strains will be heterogeneous at the scale of the periodicity of the array and the resolution of the digital image correlation technique that we have developed is not sufficient to capture this heterogeneity. This is the reason why we have performed finite element simulations to characterize the in-plane strain heterogeneities in nanostructure arrays/Kapton systems. Due to the strain heterogeneities in those arrays, we will see that the in-plane strain transmission rate is sometimes higher than the imposed strain in the Kapton substrate. Before that, we address some theoretical background regarding the elastic properties of solids. We start with a brief review of some fundamental aspects of stress, strain and the related elastic energy density.

2.2.1 Theoretical background

2.2.1.1 Stress and strains in solids

In the following definitions, we restrict ourself to states of elastic stress and strain. Let us consider an element of elementary volume cut fictitiously from a solid. This volume element is subject to different state of stress which can be classified into two categories, namely volume forces and surface forces. The volume forces are mainly due to the effect of gravity, and therefore of volume, or to electromagnetic interactions. The surface forces, on the other hand, originate outside the elementary volume under consideration and include the various forces exerted by the surrounding environment. In this case, the applied stresses on the magnetostrictive material σ are defined as the force F per area A perpendicular to the direction of the applied force. Depending on the force direction, one can distinguish between tensile and compressive stress. The stress has the same dimension as pressure, that is, $N.m^{-2}$ (or Pa) in SI unit system and $dyn.cm^{-2}$ in CGS unit system. The solid responds to the stress by a deformation called strain ε. The stress tensor is a second rank tensor, its components will all be noted by the symbol σ for the normal stresses or τ for the shear stresses with appropriate suffices. The first suffix denotes the direction of the outward normal to the surface upon which it acts and the second the direction of the stress components. The related tensor take the following

form:

$$\overline{\overline{\sigma}}= \begin{pmatrix} \sigma_{11} & \sigma_{12} & \sigma_{13} \\ \sigma_{21} & \sigma_{22} & \sigma_{23} \\ \sigma_{31} & \sigma_{32} & \sigma_{33} \end{pmatrix} = \begin{pmatrix} \sigma_{11} & \tau_{12} & \tau_{13} \\ \tau_{21} & \sigma_{22} & \tau_{23} \\ \tau_{31} & \tau_{32} & \sigma_{33} \end{pmatrix} \tag{2.83}$$

The stress tensor is symmetric ($\sigma_{ij} = \sigma_{ji}$), this propriety is the result of the momentum equilibrium condition of an infinitesimal volume. The strain is a consequence of stress. As a result of strain in a material a point is moved from (x_1, x_2, x_3) to (x_1', x_2', x_3') by amounts u_i such that $x'_i = x_i + u_i$, where u_i vary with position:

$$u_i = e_{ij} x_j \tag{2.84}$$

We have defined a second rank tensor with nine components e_{ij} (with $e_{ij} = \frac{\partial u_i}{\partial x_j}$). The component e_{ij} represents the movement of points on the x_j axis in the direction of the x_i axis. We can separate these contributions by expressing e_{ij} as the sum of symmetrical (ε_{ij}) and antisymmetrical (ω_{ij}) components:

$$e_{ij} = \varepsilon_{ij} + \omega_{ij} \tag{2.85}$$

where

$$\varepsilon_{ij} = (e_{ij} + e_{ji})/2 \tag{2.86}$$

and

$$\omega_{ij} = (e_{ij} - e_{ji})/2 \tag{2.87}$$

Shape change (shear) is described by the symmetrical tensor ε_{ij}. This is the strain tensor. Rotation is described by the antisymmetrical tensor ω_{ij}. As a resume, the strain tensor has the following form:

$$\overline{\overline{\varepsilon}}= \begin{pmatrix} \varepsilon_{11} & \varepsilon_{12} & \varepsilon_{13} \\ \varepsilon_{21} & \varepsilon_{22} & \varepsilon_{23} \\ \varepsilon_{31} & \varepsilon_{23} & \varepsilon_{33} \end{pmatrix} \tag{2.88}$$

diagonal terms reflect the change in volume of the stressed member, while non-diagonal terms express shear. This shear is said to be pure when the trace (sum of the diagonal terms) of the deformation tensor is zero.

2.2.1.2 Elasticity in single crystal: the cubic case

In the elastic regime, the strain is related to the stress thanks to Hooke's law which says that the strain is proportional to the stress. In addition, stress and strain can be related by either the stiffness tensor (C_{ijkl}) or the compliance tensor (s_{ijkl}), each of which is of fourth rank tensor. For example a stress component is given in terms of the strain components which is given using the summation convention by:

$$\sigma_{ij} = C_{ijkl} \varepsilon_{kl} \tag{2.89}$$

Or, using the compliance tensor:

$$\varepsilon_{ij} = S_{ijkl} \sigma_{kl} \tag{2.90}$$

If the body is homogeneous, that is, the mechanical properties are the same for every particle in the body, then C_{ijkl} are independent of position. We shall be concerned only

Stresses		Strains	
Tensor Notation	Contracted Notation	Tensor Notation	Contracted Notation
$\sigma_{11}(\sigma_1)$	σ_1	$\varepsilon_{11}(\varepsilon_1)$	ε_1
$\sigma_{22}(\sigma_2)$	σ_2	$\varepsilon_{22}(\varepsilon_2)$	ε_2
$\sigma_{33}(\sigma_3)$	σ_3	$\varepsilon_{33}(\varepsilon_3)$	ε_3
$\tau_{23}=\sigma_{32}$	σ_4	$\gamma_{23}=2\varepsilon_{32}$	ε_4
$\tau_{31}=\sigma_{31}$	σ_5	$\gamma_{31}=2\varepsilon_{31}$	ε_5
$\tau_{12}=\sigma_{12}$	σ_6	$\gamma_{12}=2\varepsilon_{12}$	ε_6

Table 2.1: Tensor versus contracted notation for stresses and strains.

with homogeneous bodies. There are 81 coefficients in equation 2.89 and equation 2.90, due to the symmetry of the strain tensor ($\varepsilon_{ij} = \varepsilon_{ji}$), we have $C_{ijkl} = C_{ijlk}$, the number of independent C_{ijkl} goes from 81 to 54. Moreover, due the symmetry of the stress tensor ($\sigma_{ij} = \sigma_{ji}$), we have $C_{ijkl} = C_{jikl}$, the preceding equations further reduce the number of independent coefficients 54 independent by 18. Thus, we have, for the general case of a linearly elastic body, a maximum of 36 material coefficients. Using this so-called contracted Voigt subscript notation (see table 2.1), we can express the various equations in a shorter form, the fourth order tensor C_{ijkl} reduces to the matrix representation C_{ij}.

The stiffness and compliance matrix C_{ij} (resp. S_{ij}) have 36 constants. However, less than 36 of the constants can be shown to actually be independent for elastic materials when important characteristics of the strain energy are considered. Elastic materials for which an elastic potential or strain energy density function exists have incremental work per unit volume of [93] :

$$\mathrm{d}F_{el} = \sigma_i \mathrm{d}\varepsilon_i \tag{2.91}$$

When the stresses σ_i act through strains $\mathrm{d}\epsilon_i$. However, because of the stress-strain relations, Equation 2.89, the increment work becomes[94, 95]:

$$\mathrm{d}F_{el} = C_{ij}\varepsilon_j \mathrm{d}\varepsilon_i \tag{2.92}$$

Upon integration for all strains, the work per unit of volume is :

$$F_{el} = \frac{1}{2} C_{ij}\varepsilon_i\varepsilon_j \tag{2.93}$$

However, Hooke's law, Equation 2.89, can be derived from Equation 2.93 i.e $\frac{\partial F_{el}}{\partial \epsilon_i} = C_{ij}$, where upon $\frac{\partial^2 F_{el}}{\partial \epsilon_i \partial \epsilon_j} = \frac{\partial^2 F_{el}}{\partial \epsilon_j \partial \epsilon_i} = C_{ij} = C_{ji}$. Thus, the stiffness matrix is symmetric, so only 21 of the constants are independent. We have then the following stress-strain relation in Equation 2.94 [3] with a reduction from 36 to 21 independent constants:

[3] The relations in Equation 2.94 are referred to characterizing anistropic materials because there no planes of symmetry for the materials properties.

$$\begin{pmatrix} \sigma_1 \\ \sigma_2 \\ \sigma_3 \\ \tau_4 \\ \tau_5 \\ \tau_6 \end{pmatrix} = \begin{pmatrix} C_{11} & C_{12} & C_{13} & C_{14} & C_{15} & C_{16} \\ C_{12} & C_{22} & C_{23} & C_{24} & C_{25} & C_{26} \\ C_{13} & C_{23} & C_{33} & C_{34} & C_{35} & C_{36} \\ C_{14} & C_{24} & C_{34} & C_{44} & C_{45} & C_{46} \\ C_{15} & C_{25} & C_{35} & C_{45} & C_{55} & C_{56} \\ C_{16} & C_{26} & C_{36} & C_{46} & C_{56} & C_{66} \end{pmatrix} \begin{pmatrix} \varepsilon_1 \\ \varepsilon_2 \\ \varepsilon_3 \\ \gamma_4 \\ \gamma_5 \\ \gamma_6 \end{pmatrix} \tag{2.94}$$

The number of independent elastic constants can be further reduced in materials having a higher degree of crystal symmetry. In such case, some elastic constants may vanishes while the others are related each other. Among the material with higher degree of symmetry, the cubic material is the simplest. Consider a cubic material for which the [100], [010] and [001] cube axes are parallel to the axes x_1; x_2; x_3 coordinate system. Then, the non-zero elements of the elastic stiffness C_{ij} are given in the Equation 2.95 where $C_{11} = C_{22} = C_{33}$, $C_{12} = C_{23} = C_{31}$, $C_{44} = C_{55} = C_{66}$ and all others elastic constants vanish [96].

$$\begin{pmatrix} C_{11} & C_{12} & C_{12} & 0 & 0 & 0 \\ C_{12} & C_{11} & C_{12} & 0 & 0 & 0 \\ C_{12} & C_{12} & C_{11} & 0 & 0 & 0 \\ 0 & 0 & 0 & C_{44} & 0 & 0 \\ 0 & 0 & 0 & 0 & C_{44} & 0 \\ 0 & 0 & 0 & 0 & 0 & C_{44} \end{pmatrix} \tag{2.95}$$

Thus, using Equation 2.95 into the Equation 2.93 we can calculate the elastic energy for a cubic material:

$$F_{el} = \frac{1}{2}C_{11}(\varepsilon_1^2 + \varepsilon_2^2 + \varepsilon_3^2) + C_{12}(\varepsilon_1\varepsilon_2 + \varepsilon_2\varepsilon_3 + \varepsilon_1\varepsilon_3) + \frac{1}{2}C_{44}(\varepsilon_4^2 + \varepsilon_5^2 + \varepsilon_6^2) \tag{2.96}$$

2.2.1.3 Elasticity in polycrystals

The thin films studied during this research project are either polycrystals films or amorphous films. Indeed, the polycristalline thin films are constituted of an aggregate of crystal grains of various sizes and orientation. Their macroscopic properties are affected by the properties of the individual grains. The macroscopic behavior of our polycristalline films will be regarded as isotropic and homogeneous in term of elastic properties because we have verified that they have random crystallographic texture (non-textured polycrystal). The elastic strain and stress states of an individual crystallites is determined by the Hooke's equation (see equation 2.89) together with the boundary conditions. In these conditions, homogenization methods are used to define effective elastic coefficients which will depend on the single crystal's elastic coefficients. Reuss and Voigt homogenization methods are the simplest ones[97]. They are well known because the obtained values define a boundary for the effective elastic coefficients. For instance, in the case of an isotropic thin film, the effective elastic coefficients in the Voigt model ($\widetilde{C}_{11}$, $\widetilde{C}_{12}$ and

$\widetilde{C}_{44}$) are given by (with $C = C_{11} - C_{12} - 2C_{44}$)[98]:

$$\widetilde{C}_{11} = C_{11} - \frac{2}{5}C \tag{2.97}$$

$$\widetilde{C}_{12} = C_{12} + \frac{1}{5}C \tag{2.98}$$

$$\widetilde{C}_{44} = C_{44} + \frac{1}{5}C \tag{2.99}$$

while in the Reuss model they are given by (with $S = S_{11} - S_{12} - \frac{1}{2}S_{44}$):

$$\widetilde{C}_{11}^{-1} = C_{11}^{-1} - \frac{2}{5}S \tag{2.100}$$

$$\widetilde{C}_{12}^{-1} = C_{12}^{-1} + \frac{1}{5}S \tag{2.101}$$

$$\widetilde{C}_{44}^{-1} = C_{44}^{-1} + \frac{4}{5}S \tag{2.102}$$

$$\begin{pmatrix} \widetilde{C}_{11}+2\widetilde{C}_{44} & \widetilde{C}_{11} & \widetilde{C}_{11} & 0 & 0 & 0 \\ \widetilde{C}_{11} & \widetilde{C}_{11}+2\widetilde{C}_{44} & \widetilde{C}_{11} & 0 & 0 & 0 \\ \widetilde{C}_{11} & \widetilde{C}_{11} & \widetilde{C}_{11}+2\widetilde{C}_{44} & 0 & 0 & 0 \\ 0 & 0 & 0 & \widetilde{C}_{44} & 0 & 0 \\ 0 & 0 & 0 & 0 & \widetilde{C}_{44} & 0 \\ 0 & 0 & 0 & 0 & 0 & \widetilde{C}_{44} \end{pmatrix} \tag{2.103}$$

One can note here that only two independent coefficients are remaining ($\widetilde{C}_{11}$ and $\widetilde{C}_{44}$). The following relation is thus deduced:

$$\sigma_{ij} = \widetilde{C}_{11}\delta_{ij}\varepsilon_{kk} + 2\widetilde{C}_{44}\varepsilon_{ij} \tag{2.104}$$

From this relation $\sigma_{kk} = \left(3\widetilde{C}_{11} + 2\widetilde{C}_{44}\right)\varepsilon_{kk}$, we can rewrite the above formula as function of the stresses:

$$\varepsilon_{ij} = \frac{1}{2\widetilde{C}_{44}}\sigma_{ij} - \frac{\widetilde{C}_{11}}{2\widetilde{C}_{44}(3\widetilde{C}_{11}+2\widetilde{C}_{44})}\sigma_{kk}\delta_{ij} \tag{2.105}$$

We can define the Young's modulus (Y) and the Poisson's ratio (ν) by considering a simple traction:

$$\sigma = \begin{pmatrix} \sigma & 0 & 0 \\ 0 & 0 & 0 \\ 0 & 0 & 0 \end{pmatrix}; \varepsilon = \begin{pmatrix} \varepsilon_L & 0 & 0 \\ 0 & \varepsilon_T & 0 \\ 0 & 0 & \varepsilon_T \end{pmatrix} \tag{2.106}$$

Where ε_L and ε_T stand for the longitudinal and the transverse strains, respectively. They can be written as function of $\widetilde{C}_{11}$ and $\widetilde{C}_{44}$:

$$\varepsilon_L = \frac{\widetilde{C}_{11}+\widetilde{C}_{44}}{\widetilde{C}_{44}(3\widetilde{C}_{11}+2\widetilde{C}_{44})}\sigma = \frac{1}{Y}\sigma \tag{2.107}$$

$$\varepsilon_T = -\frac{\widetilde{C}_{11}}{2\widetilde{C}_{44}(3\widetilde{C}_{11}+2\widetilde{C}_{44})}\sigma = -\nu\varepsilon_L \tag{2.108}$$

Where the Young's modulus Y and the Poisson's ratio (ν) are given by:

$$Y = \frac{\widetilde{C}_{44}(3\widetilde{C}_{11} + 2\widetilde{C}_{44})}{\widetilde{C}_{11} + \widetilde{C}_{44}} \tag{2.109}$$

$$\nu = \frac{\widetilde{C}_{11}}{2(\widetilde{C}_{11} + \widetilde{C}_{44})} \tag{2.110}$$

The equation 2.105 can be rewritten by introducing Y and ν:

$$\varepsilon_{ij} = \frac{1+\nu}{Y}\sigma_{ij} - \frac{\nu}{Y}\sigma_{kk}\delta_{ij} \tag{2.111}$$

$$\sigma_{ij} = \frac{Y}{1+\nu}\varepsilon_{ij} + \frac{\nu Y}{(1+\nu)(1-2\nu)}\varepsilon_{kk}\delta_{ij} \tag{2.112}$$

Note that we can also define the bulk modulus (K) by considering an hydrostatic compression. In this condition, we have $\sigma_{ij} = \sigma\delta_{ij}$ and $\varepsilon_{ij} = \varepsilon\delta_{ij}$, which lead to $\sigma_{ij} = (3\widetilde{C}_{11} + 2\widetilde{C}_{44})\varepsilon$. We deduce that

$$K = \frac{1}{3}\left(3\widetilde{C}_{11} + 2\widetilde{C}_{44}\right) = \frac{1}{3}\frac{Y}{1-2\nu} \tag{2.113}$$

2.2.2 Strain field modelization in arrays of ferromagnetic nanostructures (Nanowires and antidot arrays)

The strain field generated in the nanostructures induced by the PZT substrate is determined by finite element method within COMSOL Multiphysics®[92, 99]. The geometry of the systems consists of a Kapton® layer of dimensions $7.5\times7.5\times5$ μm^3 and a $Ni_{60}Fe_{40}$ magnetic nanostructure array of dimensions $7.5 \times 7.5 \times 0.02$ μm^3 containing 8×8 nanodots periodically distributed according to both the studied geometries (parallel and perpendicular to the length of the nanowires system and parallel to axes of the antidot arrays or in the diagonal direction of this latter). The interface between the polymer layer and the nanostructures is assumed to be perfect (perfect adhesion implying continuity of the displacement and the traction vector at the interface). It is worth noting that the represented thickness of the Kapton® layer (5 μm) is much lower than the real thickness (127.5 μm). This thickness is however sufficient to avoid possible perturbations that may be caused by the stiffer magnetic nanostructures on the average strain of the compliant layer. It is also worth noting that the PZT ferroelectric behavior is not modeled here, only the strain applied by the PZT to the Kapton® is modeled. All these justified modeling choices are motivated by optimization/reduction of the computing time. Thus, it is necessary during numerical simulations to replicate the homogeneous in-plane strains transmitted by the PZT substrate to the Kapton® layer. For this purpose, the following tensile-compression displacement loading will be applied to the Kapton® layer[99]:

$$U_x = \epsilon_{xx}^{sub} x \quad / \quad x = \pm\frac{L}{2} \tag{2.114}$$

$$U_y = \varepsilon_{yy}^{sub} y \quad / \quad y = \pm\frac{L}{2} \tag{2.115}$$

U_x and U_y represent the displacement magnitudes applied quasi-statically to the Kapton® layer and L is the length of the Kapton® layer. Regarding the spatial discretization of the calculation domain in accordance with the finite element method, the COMSOL Multiphysics® automatic mesher was used[100]. Special attention was paid to densify the mesh wherever necessary, i.e. in the neighborhoods of interfaces and free surfaces. An evolutive spatial discretization was thus carried out, utilizing a 1-degree tetrahedral Lagrangean finite element, with a minimum characteristic length of 10 nm. This length enables to have two rows of finite elements along the thickness of the deposit (corresponding to the nanostructures thickness), which is sufficient to accurately calculate the mean strain in the nanostructures. Moreover, it has been checked that the adopted meshing density enables to reach the convergence of the numerical results. In view of the relatively small deformations involved here, the calculations are carried out within the linear framework of small perturbation assumptions. Within the small ranges of strain, the materials studied behave linearly in addition to being isotropic. Once the calculations are performed, a gage zone of dimensions 3×3 μm^2 was considered inside the nanostructures so as to avoid the disturbance induced by the free and loaded edges during the post-processing of the numerical results which will be shown in the corresponding chapters.

3 Development of a fully coupled mechanical-micromagnetic model

Contents

In this chapter, a numerical simulation tool that accounts for heterogeneous strain fields of magnetic strained objects has been developed, validated and tested for problems of increasing complexity. The LLG equation is solved by finite element methods in a fully coupled way with solid mechanical governing equations. This resolution is achieved within the software COMSOL Multiphysics®[92]. A concise presentation of the local governing equations with the associated boundary, initial and jump conditions is first provided. Then, the chosen examples related to the Larmor magnetization precession, dipolar interaction in circular and spherical media, magnetization reversal in non-strained nanostructure, and the effect of homogeneous strain on magnetization distribution are treated so as to validate the mathematical coupled problem implementation compared to analytical solutions when available. In particular, the obtained versatile numerical simulation tool is compared with the Nmag [54] micromagnetic code for the magnetization reversal of an unstrained object as another numerical validation considering an unstrained object. Finally, the validated simulation tool is deployed to simulate the targeted material systems corresponding to a magnetic nanomembranes submitted either to heterogeneous or homogeneous strain fields.

3.1 Implementation of LLG equation coupled with solid mechanical equations

Throughout this chapter we have used the SI system. When needed, we give the expressions of the energies in this system when it is necessary compared to what was introduced in the previous chapter. Let $\vec{m}$ be the reduced magnetization vector whose components are given by $m_i = M_i/M_s$ where i stands for x, y or z directions and M_s the saturation magnetization. As introduced in the precedent chapter, the global equilibrium of a magnetoelastic object can be written in term of the total energy density F as:

$$F = F_{Zee} + F_{ex} + F_{ms} + F_{el} \tag{3.1}$$

with $F_{Zee} = -\mu_0 M_s \vec{m} \cdot \vec{H}$, the Zeeman energy density, $F_{ex} = A\,(\nabla \vec{m})^2$, the exchange energy density, $F_{ms} = -\frac{1}{2}\mu_0 M_s \vec{H}_{dem}.\vec{m}$, the magnetostatic energy density. Here, $\vec{H}_{dem}$ is the demagnetizing field that is determined from the magnetic potential ϕ as $\vec{H}_{dem} = -\vec{\nabla}\phi$. The magnetic potential ϕ being the solution of the magnetostatic boundary value problem. Finally, F_{el} is the elastic energy density that contains the magnetoelastic contribution. For the sake of simplicity, we consider in the following, the magnetic medium as isotropic (isotropic elasticity and magnetoelasticity in absence of magnetocrystalline anisotropy) and this contribution can be written as:

$$F_{el} = \frac{1}{2}\underline{\underline{\varepsilon}}^{el} : \underline{\underline{\underline{\underline{C}}}} : \underline{\underline{\varepsilon}}^{el} \tag{3.2}$$

where $\underline{\underline{\varepsilon}}^{el}$ is the elastic strain second order tensor and $\underline{\underline{\underline{\underline{C}}}}$, the elastic stiffness fourth order tensor. In case of isotropic elasticity, the non-zero elastic stiffness components can be simply written as functions of Young's modulus E and Poisson's ratio ν. For magnetostrictive materials, the elastic strain $\underline{\underline{\varepsilon}}^{el}$ is equal to the total strain $\underline{\underline{\varepsilon}}$ minus the magnetoelastic one $\underline{\underline{\varepsilon}}^{m}$[101]:

$$\underline{\underline{\varepsilon}}^{el} = \underline{\underline{\varepsilon}} - \underline{\underline{\varepsilon}}^{m} \tag{3.3}$$

with,

$$\underline{\underline{\varepsilon}}\,(\overrightarrow{u}) = \frac{\overrightarrow{\nabla} \otimes \overrightarrow{u} + \left(\overrightarrow{\nabla} \otimes \overrightarrow{u}\right)^t}{2}, \tag{3.4}$$

and

$$\underline{\underline{\varepsilon}}^{m} = \frac{3}{2}\lambda \begin{pmatrix} m_x^2 - \frac{1}{3} & m_x m_y & m_x m_z \\ m_x m_y & m_y^2 - \frac{1}{3} & m_y m_z \\ m_x m_z & m_y m_z & m_z^2 - \frac{1}{3} \end{pmatrix}, \tag{3.5}$$

for an isotropic magnetostrictive ferromagnetic medium, with λ, the isotropic magnetostriction coefficient. It is worth noting that only the quasi-static displacement $\vec{u}$ is considered here for the calculation of $\underline{\underline{\varepsilon}}^{el}$ (*i.e.* dynamic effects of acceleration are neglected). Moreover, the magnetization distribution directly derives from a competition between the energy contributions mentioned above. To study the temporal evolution of the magnetization of the ferromagnetic medium, it is necessary to solve the LLG equation:

$$\frac{\partial \vec{m}}{\partial t} = -\mu_0 \gamma \vec{m} \times \vec{H}_{eff} + \alpha \vec{m} \times \frac{\partial \vec{m}}{\partial t} \tag{3.6}$$

where γ is the gyromagnetic ratio, α, the dimensionless Gilbert damping coefficient and $\vec{H}_{eff}$, the effective field, which stands as the functional derivative of the total energy density F (equation 3.1). It is important to note that the LLG is a nonlinear equation as the effective field $\vec{H}_{eff}$, intervening in the right hand side of the LLG equation, is a function of the LLG unknown itself, namely the magnetization $\vec{m}$, besides two other unknowns, the displacement $\vec{u}$ (through the strain) and the magnetic potential ϕ (through the demagnetizing field) (equations 3.1-3.3). Thus, to determine the temporal evolution of the magnetization in a ferromagnetic medium, it is necessary to solve the LLG equation in conjunction with two other field equations, viz. the mechanical equilibrium equation[102]:

$$\vec{\nabla} \cdot \left(\underline{\underline{\underline{C}}} : \underline{\underline{\varepsilon}} \right) + \vec{f} = \vec{0}, \tag{3.7}$$

and the magnetostatic equation:

$$\vec{\nabla} \cdot \vec{H}_{dem} = -\triangle \phi = S \tag{3.8}$$

The LLG equation is pertaining to the magnetic nanostructure domain (Ω_1), whereas the equilibrium equation (equation 3.7) concerns the magnetic nanostructure (Ω_1) and the substrate (Ω_2) domains, and the magnetostatic equation (equation 3.8) is related to the whole system constituted of the magnetic nanostructure (Ω_1), the substrate (Ω_2) and the surrounding universe (Ω_3).
In equation 3.7, $\vec{f}$=$\vec{0}$ as no body force is applied, whereas the source term (S) in equation 3.8 changes from a domain to another as follows:

$$S = \begin{cases} -\vec{\nabla} \cdot (M_s \vec{m}) & \text{on } (\Omega_1) \\ 0 & \text{on } (\Omega_2) \\ 0 & \text{on } (\Omega_3) \end{cases} \tag{3.9}$$

The above field equations (equations 3.7 and 3.8) are completed by the following boundary, transmission and initial conditions:

- Mechanical kinematic loading:

$$\vec{u} = \vec{u}^p \tag{3.10}$$

with $\vec{u}^p$ the prescribed displacement on the loaded faces of the substrate (Ω_2).

- Perfect adhesion jump conditions:

$$[\![\vec{u}]\!] = \left[\!\left[\left(\underline{\underline{\underline{C}}} : \underline{\underline{\varepsilon(\vec{u})}}\right) \cdot \vec{n}\right]\!\right] = \vec{0} \tag{3.11}$$

at the magnetic (Ω_1)/substrate (Ω_2) interface ($\vec{n}$ is the outer unit normal of the interface)

- Free boundary conditions:

$$\left(\underline{\underline{\underline{C}}} : \underline{\underline{\varepsilon(\vec{u})}}\right) \cdot \vec{n} = \vec{0}$$

on the borders of both magnetic (Ω_1) and substrate (Ω_2) domains that are free from any loading.

- Continuity of the perpendicular component of the magnetic induction:

$$\vec{n} \cdot \vec{\nabla}\phi = M_s \vec{m} \cdot \vec{n} \tag{3.12}$$

on the magnetic domain border (Ω_1),

$$\vec{n} \cdot \vec{\nabla}\phi = 0 \tag{3.13}$$

on the border of the domain (Ω_2) and the inner border of the domain (Ω_3).

- Remote condition of the evanescence of the demagnetizing potential far away:

$$\vec{n} \cdot \vec{\nabla}\phi = -2\frac{\phi_3}{\sqrt{x^2 + y^2 + z^2}} \tag{3.14}$$

on the outer border of the universe (Ω_3)

- Continuity of the parallel component of the magnetic field:

$$[\![\phi]\!] = 0 \tag{3.15}$$

depicting the continuity of the demagnetizing potential at each interface between adjacent domains.

- Initial conditions:

$$\vec{m}(\vec{r}, t = 0) = \vec{m}^p \tag{3.16}$$

where $\vec{m}^p$ stands as a prescribed value verifying $\|\vec{m}^p\| = 1$. It is worth mentioning that theoretically $\|\vec{m}\| = 1 \ \forall \vec{r} \in (\Omega_1)$; this condition has been numerically satisfied accounting the numerical errors. Moreover, it has been also numerically verified that the norm of the space mean value of $\vec{m}$ is always bounded by 1 for any non uniform magnetic moment distributions:

$$\|\langle \vec{m} \rangle\| < 1 \tag{3.17}$$

This criterion-like directly derives from the use of Schwartz theorem[1]. Finally, the above strongly coupled boundary and initial value problems are solved numerically by finite element method within the software Comsol Multiphysics® in order to simulate the temporal evolution of the magnetization under mechanical loading.

3.2 Numerical validations

In this section, four selected problems are solved for the purpose of validating the developed simulation code of micromagnetic mechanical, in the elastic regime, coupling within COMSOL Multiphysics®[92]. In the first problem, the LLG (3.6) is resolved alone to simulate the Larmor precession (in absence of damping). The second problem concerns the determination of the magnetostatic field inside (demagnetizing field) and outside (stray field) the examined ferromagnetic nano-object. The third problem corresponds to a quantitative comparison with a software specifically dedicated to micromagnetic, viz. the Nmag package [54]. For this purpose, the LLG equation is resolved in presence of all magnetic fields excepted the magnetoelastic one. In the last validation problem, the LLG equation is resolved by taking into account the magnetoelastic energy density in order to

[1] Indeed, one can show that

$$\left(\frac{\int m_x dV}{\int dV}\right)^2 + \left(\frac{\int m_y dV}{\int dV}\right)^2 + \left(\frac{\int m_z dV}{\int dV}\right)^2 < 1 \tag{3.18}$$

for any non-uniform configuration thanks to Schwartz inequality which states that if we consider two independent functions f and g, we have $\left(\int (fg)\, dV\right)^2 < \int f^2 dV \int g^2 dV$. The application of this Schwartz inequality to micromagnetism can be performed by considering a non uniform magnetization distribution for at least one component. Thus, one can suppose that m_x is variable and we apply Schwartz's inequality to the functions $f = m_x$ et $g = 1$. One obviously deduced that:

$$\left(\int m_x dV\right)^2 < \int m_x^2 dV \int dV \tag{3.19}$$

For the other components, we can write a similar relation by replacing x by y or z. Thus, we deduced that:

$$\left(\int m_x dV\right)^2 + \left(\int m_y dV\right)^2 + \left(\int m_z dV\right)^2 < \int \left(m_x^2 + m_y^2 + m_z^2\right) dV \int dV \tag{3.20}$$

study the magnetization of a magnetic nanowire homogeneously strained (or stressed). It is worth noting that for the performed simulations, the nano-objects were meshed by using the automatic mesher of COMSOL. Particular attention was paid to the distance between two adjacent nodes so that it does not exceed the exchange length defined as $\ell_{ex} = \sqrt{\frac{2A}{\mu_0 M_S^2}}$[103, 101, 104].

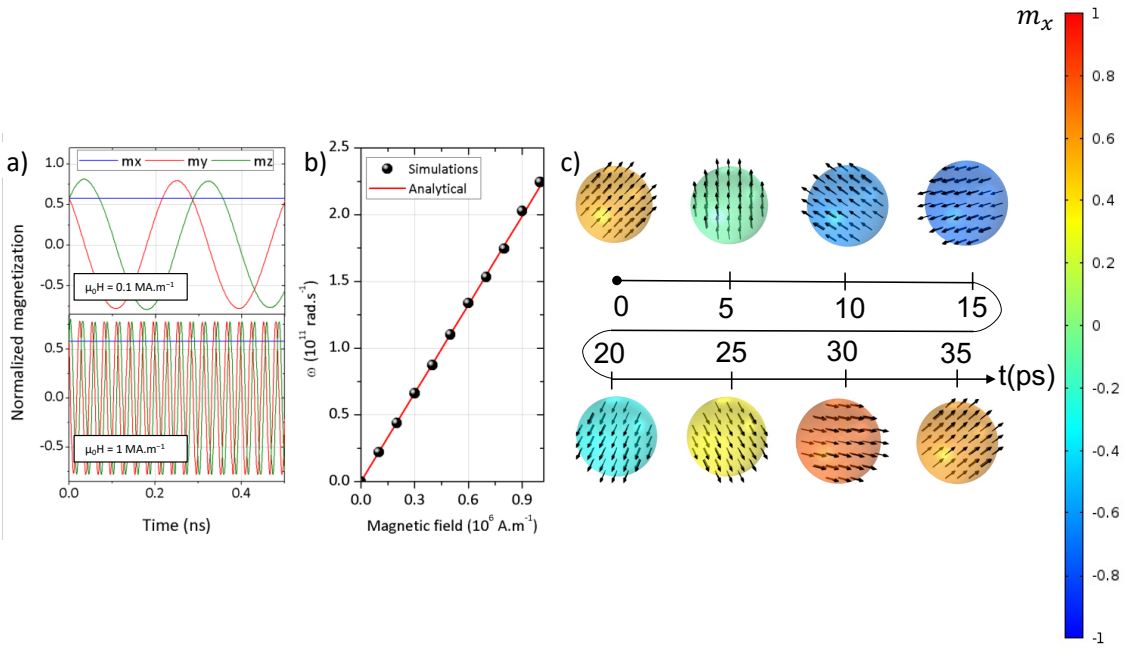

Figure 3.1: a) Temporal evolution of the normalized magnetization components for two different values of the applied magnetic field (along with $x-$direction): $\mu_0 H = 0.1 \times 10^6$ A.m^{-1} (top) and 1×10^6 A.m^{-1}(down). The initial magnetization is uniform and aligned along $[1, 1, 1]$ direction. b) Variation of the frequency of precession, extracted from the temporal evolution of the magnetization, as a function of the applied magnetic field. Symbols correspond to numerical calculations while the continuous line depicts the analytical result (equation 3.21). c) 3D maps showing the magnetic moments distribution at different times under an applied magnetic field of 1×10^6 A.m^{-1} along with x-direction. Colors encode m_y.

3.2.1 Larmor's precession

Here, we consider a magnetic sphere of radius 10 nm undergoing an applied (external) magnetic field with no dipolar interaction effect ($\vec{H}_{dem} = \vec{0}$). The retained material is the permalloy ($Ni_{80}Fe_{20}$) whose bulk magnetic parameters are: $M_s = 0.8 \times 10^6$ A.m^{-1},

$\mu_0\gamma = 221017$ m.A^{-1}.s^{-1} and $A = 10 \times 10^{-12}$ J.m^{-1}. These parameters lead to an exchange length $\ell_{ex} \approx 4$ nm. Moreover, the Gilbert's coefficient is set to zero ($\alpha = 0$) with the idea to retrieve the well known Larmor's precession. Indeed, under the unique presence of an applied magnetic field (absence of magnetocrystalline, magnetoelastic and dipolar contributions), all the magnetic moments precess at unisson and the precession frequency can be written as:

$$\omega = \gamma\mu_0 H \tag{3.21}$$

where H is the applied magnetic field. This latter is applied along $x-$direction while the initial magnetic moments distribution are kept uniform and oriented along the $[1, 1, 1]$ direction. In Figure 3.1-a), we reported the temporal evolution of the normalized magnetization components ($\langle m_x \rangle$ in blue, $\langle m_y \rangle$ in red and $\langle m_z \rangle$ in green) for two different values of the applied magnetic field (0.1×10^6 and 1×10^6 A.m^{-1}). The curves show an evolving magnetization with a temporal conservation of its norm ($\|\vec{m}\| = 1$) and a unison precession of all magnetic moments around the applied magnetic field along x. This leads to a constant temporal mean value of x-component of the magnetization $\langle m_x \rangle$. The 3D maps of the magnetic moments displayed at different times within one period clearly show this phenomenon (see figure 3.1 -c)). Also, we have reported the precession frequency, calculated from the magnetization oscillations, as a function of $\mu_0 H$ in figure 3.1-b). Comparison with the analytical solution of the Larmor precession depicted by a continuous red line in the figure, shows the good agreement between the two numerical and analytical evaluations, which constitutes a validation of the numerical implementation of the LL (Landau-Lifshitz) equation.

3.2.2 Magnetostatic field

In this example, the validation of the procedure for calculating the demagnetizing field is sought. For that purpose, we choose to apply it for material systems for which there exists closed-form solutions. These material systems are constituted of a ferromagnetic nano-object (Ω_1) that is a disk (2D problem) or sphere (3D problem), deposited on a substrate (Ω_2), all these surrounded by the "whole" universe (Ω_3). From a magnetic point of view, (Ω_2) and (Ω_3) are similar, and the LLG equation is only pertaining to the ferromagnetic nano-object (Ω_1).

The first material system is a 2D one allowing a 2D resolution of the magnetoelastic problem. It is constituted of a ferromagnetic nano-disk of radius 10 nm (Ω_1) homogeneously magnetized ($M_s = 1 \times 10^6$ A.m^{-1}) along $y-$direction, in immediate contact with a half holed-disk of radius 20 nm (Ω_2-substrate). The surrounding environment (Ω_3) is assimilated to a larger disk of radius 50 nm comprising (Ω_1) and (Ω_2) (see figure 3.2-a) for illustration). In Figure 3.2-a), we displayed the 2D map of the magnetostatic field calculated in the three regions. A zoom-in of the simulated system is presented in figure 3.2-b). One can note the continuity of the magnetic field lines between the different regions, which confirms that the magnetic boundary conditions (equations 3.12-3.14) have been numerically well satisfied. This continuity is better illustrated in figure 3.2-c) that presents 1D-profiles of $y-$component of the magnetostatic field H_{ms}^y, the corresponding

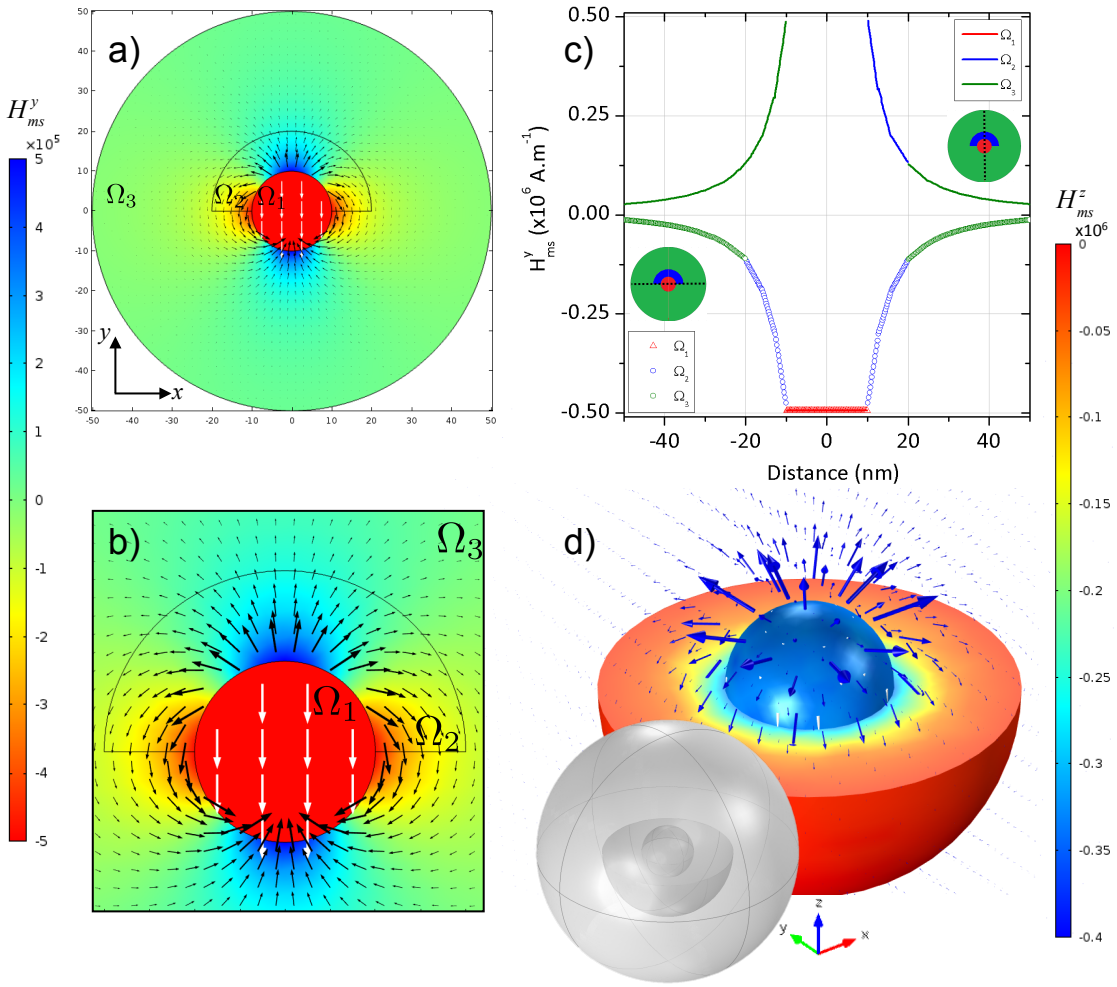

Figure 3.2: a) 2D-map of the magnetostatic field ($\vec{H}_{ms}$) calculated inside (Ω_1) and outside a uniformly magnetized (along y) disk of radius 10 nm. The outside region is divided into two different regions (Ω_2) and (Ω_3) with similar characteristic from a magnetic point of view. Colors encode y-component of the magnetostatic field H^y_{ms}. b) Zoom-in of a). c) 1D-profiles of the magnetostatic field; the corresponding lines are drawn in the graph. Data from $(\Omega)_1$ (resp. Ω_2 and Ω_3) are represented in red (resp. blue and green). For clarity, only H^y_{ms} component is plotted with continuous lines for the vertical cutline and with empty symbols for the horizontal cutline. d) 3D map of $\vec{H}_{ms}$ (blue arrows) where colors encode H^z_{ms} (only in regions (Ω_1) and (Ω_2) for clarity).

cutlines are drawn in the figure (vertical cutline: continuous lines and horizontal cutline: symbols). From those cutlines, it is obvious that H^x_{ms}, which is not plotted for clarity on the graphs, is zero in the three regions. Data from (Ω_1) (resp. (Ω_2) and (Ω_3)) are plotted in red (resp. blue and green). Our results fit well with the well known analytical solutions for this problem, we retrieve for instance that $\vec{H}_{dem} = -\frac{\vec{M}}{2}$ in Ω_1. In fact, in the case of a homogeneously magnetized disk the demagnetizing factor ($N_x = N_y$ because of the radial symmetry) is equal to $\frac{1}{2}$. Note that the demagnetizing factors have to satisfy the condition $N_x + N_y = 1$.
The second studied material system is the 3D counterpart of the former one. The gray sketch in figure 3.2-d) depicts the geometry of the simulated system. Concentric spheres have been used: the bigger sphere (whole universe (Ω_3)) has a radius of 100 nm, the inner sphere (magnetic object (Ω_1)) has a radius of 20 nm and the half hollow sphere (substrate (Ω_2)) has a radius of 50 nm. In this problem, the magnetic object (inner sphere) has been uniformly magnetized along z. Figure 3.2-d), where colors encode H^z_{ms}, displays the 3D map of the calculated magnetostatic field (blue arrows). For clarity, H^z_{ms} has been colored-mapped only in regions (Ω_1) and (Ω_2). As for the 2D problem, we retrieve the well known analytical solution for such a problem of a uniform demagnetizing field $\vec{H}_{dem} = -\frac{\vec{M}}{3}$. Similarly to the precedent case, the demagnetizing factor for an homogeneously magnetized sphere is equal to $\frac{1}{3}$[68, 105].

3.2.3 Comparison with Nmag software

As an additional validation, the developed finite element code under COMSOL Multiphysics® is compared to a micromagnetic dedicated software, viz. Nmag that utilizes the finite element method too [54]. Thus, a similar mesh of the precedently simulated object is adopted. Thereby, the magnetostatic field is taken into account in the LLG equation for the simulation of the magnetization evolution. The considered problem for achieving such comparison concerns the magnetization evolution of an isolated $100 \times 40 \times 5$ nm^3 ferromagnetic nanowire, which is embedded inside a large sphere of radius 200 nm, corresponding to the surrounding environment. It can be noted here that the substrate is not simulated since it is not required for such comparison. Regarding the magnetic parameters, the previously adopted values (bulk permalloy) are again retained here with a Gilbert's damping constant $\alpha = 0.1$. Moreover, the magnetization is initially aligned along y in order to favor a realignment of the magnetic moments along the easy axis (along x) favored by the sample geometry in absence of applied magnetic field. Figures 3.3-a) and 3.3-b) present the results obtained under these conditions.

Figures 3.3-a) and 3.3-b) respectively correspond to the temporal evolution of the mean values of the normalized magnetization components $\langle m_i \rangle$ and of the demagnetizing field $\langle H^i_{dem} \rangle$. As expected, all the magnetic moments are initially aligned along y-direction (at $t = 0$ ns) while they are almost all aligned along x-direction at equilibrium. One can see the magnetization relaxation in figure 3.3-c), which presents top view mapping of the magnetization distribution at different times during the relaxation (colors encode m_x). The Nmag results are also shown in figures 3.3-a) and 3.3-a) (continuous lines). One can

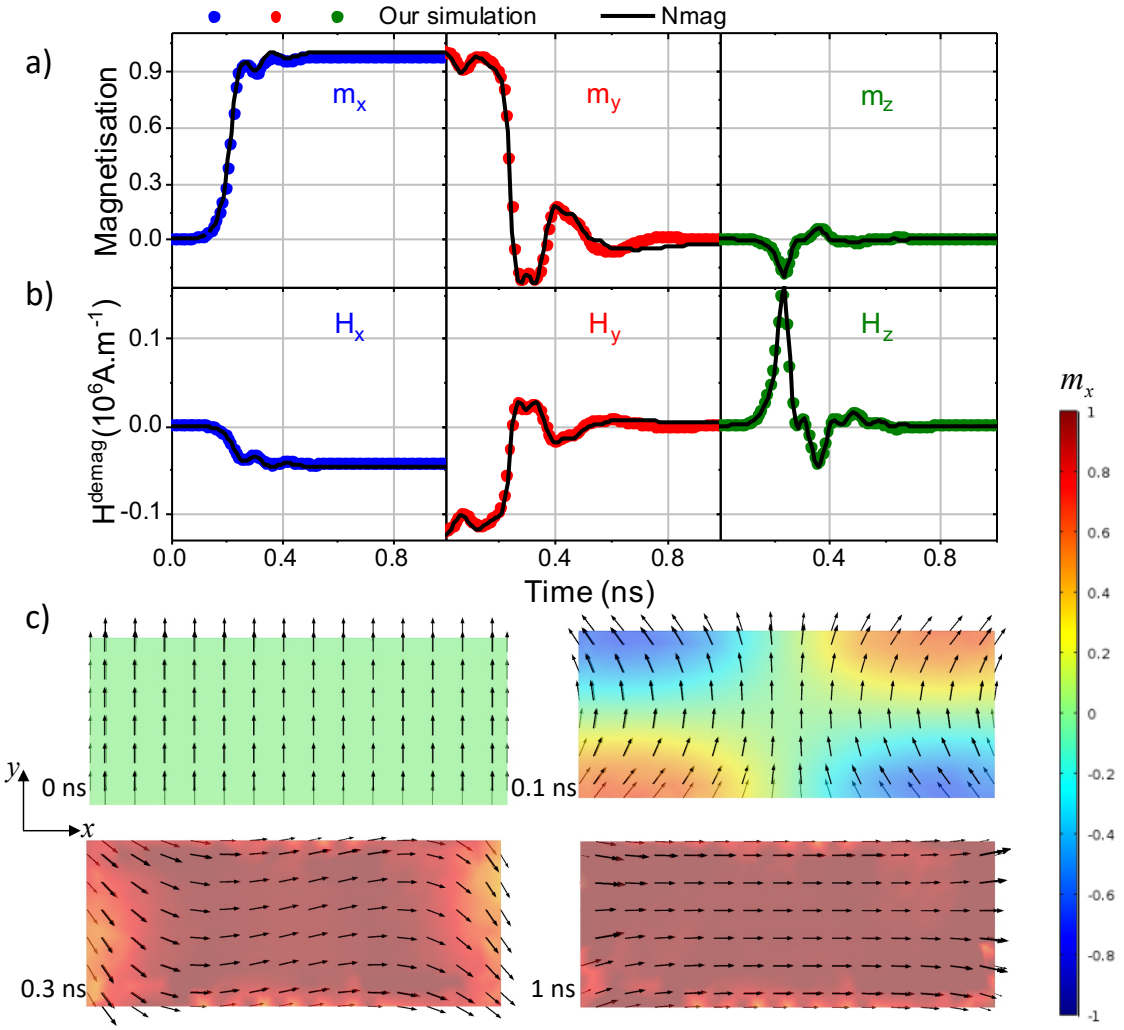

Figure 3.3: a) Temporal evolution of the mean values of the normalized magnetization components. b) Temporal evolution of the mean values of the demagnetizing field components. In a) and b), continuous lines are date obtained with Nmag software while symbols are data obtained using our model. c) Top view (xy) mapping showing the magnetization distribution in the nano-object at different times during the relaxation of the system. Colors encode x-component of the magnetization (m_x).

note the good agreement between the two models with however very slight discrepancies after the magnetization reversal (around 0.4 ns). This may be attributed to the demagnetizing field calculation method. Indeed, the "outside medium" is specifically modeled in our code, under the form of a "large" sphere of 200 nm radius, while the Fredkin and Koehler method [106] is used in the Nmag software. However, these deviations do not fundamentally change the physics nor the possible quantitative values that one could extract from these curves.

3.2.4 Self-supported nanostructure homogeneously strained

Before exploiting the developed code for the simulation of material systems undergoing heterogeneous strains, we focus on a more simpler case where the self-supported nanostructure undergoes homogeneous uniaxial tensile strain, for which there is a closed form solution of the magnetoelastic field. Hence, comparison between the numerical findings and the analytical solution will permit an additional validation of the developed simulation tool. To apply a homogeneous uniaxial tensile strain along the x-direction, the x-component of the displacement vector is symmetrically prescribed on both extremities of the sample. Jointly, the rigid modes are eliminated by assuming appropriate kinematic conditions on the sample. These latter are just right what is required, so as to not under-constrained kinematically the strained object (presence of rigid mode) nor to over-constrain it (no more homogeneous tensile strain). Note that we have used the pre-existing "Solids Mechanics" module of COMSOL Multiphysics® to calculate the stress/strain inside the nanostructure whereupon it was took into account in the LLG equation through the magnetoelastic energy contribution.
The adopted geometry corresponds to a Ni nanostructure of $150\times40\times10$ nm^3 dimensions with $M_s = 0.48 \times 10^6$ A.m^{-1}, $\mu_0\gamma = 221017$ m.A^{-1}.s^{-1}, $A = 10 \times 10^{-12}$ J.m^{-1} and $\alpha = 0.5$. Moreover, in order to avoid mixing different sources of magnetoelastic coupling, we consider isotropic mechanical and magnetoelastic parameters for the nanostructure. In these conditions, the Young's modulus and Poisson's ratio are fixed at $E_N = 200$ GPa and $\nu_N = 0.3$ while the magnetostriction coefficient is fixed at $\lambda = -30 \times 10^{-6}$ [10, 107]. The applied displacement gives rise to a strain ranging from 0 to 0.3%, which corresponds to a stress σ_{xx} ranging from 0 to 0.6 GPa. 3D maps where the colors encode σ_{xx} are presented in figure 3.4-a). These maps highlight the homogeneity of σ_{xx} inside the nanostructure. Thereafter, we have numerically evaluated the magnetoelastic field by using its closed-form expression which is formally derived from the elastic energy density F_{el}[58, 108]:

$$\begin{aligned}\vec{H}_{me} &= -\frac{1}{\mu_0 M_s}\frac{\partial F_{el}}{\partial \vec{m}} \\ &= \frac{1}{\mu_0 M_s}\underline{\underline{\underline{\underline{C}}}} : \left(\underline{\underline{\varepsilon}} - \underline{\underline{\varepsilon}}^m\right) : \frac{\partial \underline{\underline{\varepsilon}}^m}{\partial \vec{m}} \\ &= \frac{1}{\mu_0 M_s}\underline{\underline{\sigma}} : \frac{\partial \underline{\underline{\varepsilon}}^m}{\partial \vec{m}}\end{aligned} \tag{3.22}$$

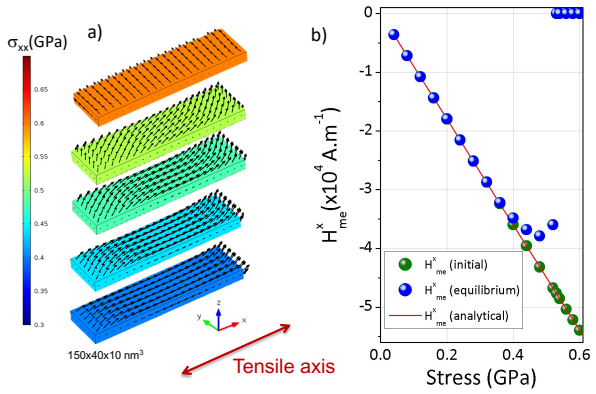

Figure 3.4: a) 3D maps of the magnetization distribution (black arrows) obtained after relaxation (*i. e.* at equilibrium) for different uniform stress states (from 0.3 GPa to 0.6 GPa). Colors encode σ_{xx}. b) Mean x-component of the magnetoelastic field $\langle H_{me}^x \rangle$ as a function of the applied uniform stress. Green and blue sphere symbols correspond to the $\langle H_{me}^x \rangle$ calculated before (at $t = 0$ ns) and after relaxation (at $t = 10$ ns), respectively.

where $\underline{\underline{\sigma}}$ is the stress tensor. According to equations 3.5 and 3.22, if one assumes a uniaxial stress state and a uniform magnetization along x-direction, the magnetoelastic field becomes:

$$\vec{H}_{me} = \frac{3\lambda\sigma_{xx}}{\mu_0 M_s}\vec{e}_x \tag{3.23}$$

The analytical expression (equation 3.23) of the magnetoelastic field can be directly compared to numerical solutions by forcing an alignment of all the magnetic moments along with the x-direction (i.e. before relaxation). Hence, we focus on two configurations of the system; the initial one at $t = 0$ ns where all the magnetic moments are parallel to $x-$direction, and the equilibrium one after precession obtained by calculation sufficiently far from the transitional regime. For both configurations, we have calculated the magnetoelastic field . The black arrows in the 3D maps (see figure 3.4-a)) illustrate to the magnetization distribution inside the nanostructure after relaxation; it seems almost uniform and aligned along with the x direction till ~ 0.4 GPa while it is aligned along with the y direction for higher stress. This is due to the competition between the shape anisotropy field of the nanostructure, which promotes an alignment of the magnetic moments along with the x direction and the magnetoelastic field, which favors an alignment along with the y direction (being given the negative sign of the Ni magnetostriction coefficient).
Figure 3.4-b) shows a good agreement between the analytical variation of H_{me} (red

continuous line) and its numerical evaluation at 0 ns (green symbols). In addition, $y-$ and z-components of the magnetoelastic field are close to zero (order of magnitude: 10^{-10} A.m^{-1}), which tend to confirm the robustness of our modeling. Regarding the H_{me} variation after relaxation (blue symbols), the performed calculations enable us to see that the magnetization evolution can be quite complex especially around the magnetization reversal (at ~ 0.52 GPa). Indeed, we note that H_{me} calculated after relaxation is almost aligned with the analytical variation (at 0 ns) but deviates around the magnetization reversal. Obviously, H_{me} is null for a stress higher than ~ 0.52 GPa because of the magnetization distribution (aligned along with y). The highlighted deviation around the magnetization reversal is due to the magnetization distribution, which proves to be uniform (see 3D maps in figure 3.4-a)). This puts forward the advantage of the proposed modeling that is able to capture magnetoelastic phenomena related to heterogeneous magnetization and/or stress of the studied sample, contrary to the analytical solution, which is confined to homogeneous stress distribution. This point will be discussed further in the next section dedicated to the simulation of the magnetization of a nanostructure deposited on the top surface of a strained polymer substrate.

3.3 Application: effects of heterogeneous strain on the magnetization processes in magnetic nanomembranes

Here, we study the effect of the heterogeneous strain in a prototypical magnetic nanomembrane of Ni on the application-relevant polyimide foil. We took into account the distribution of the magnetoelastic field in the case of the heterogeneous strain and compare it to the case of the free-standing Ni thin film.

These kind of nanostructures are in the heart of novel research directions including flexible magnetoelectronics [109, 46, 110, 14, 111, 112, 113], origami-based strain engineering technologies [114, 115, 116], curvilinear magnetism [1, 117, 118, 119], flexible magnetocaloritronics [?] and straintronics [120, 121, 122] to name just a few. In all these examples, magnetic nanomembranes are mechanically deformed, which leads to pronounced effects of mechanical strain and its impact on the magnetization reversal processes and magnetization dynamics. The performance of the devices based on magnetic nanomembrane is determined by the strain and its distribution across the thin film. The prevailing strain field within the system must be taken into account in the study of these phenomena as it can greatly influence the magnetic energy of such systems [123, 124].
Indeed, even small strains within the magnetic deposit (a few 10^{-3}) can lead to significant magnetoelastic fields (a few tens of mT) if the studied magnetic material has a magnetostriction of the order of 10^{-5}. The assumption of uniform strain is no longer valid for magnetic nanomembranes deposited on a substrate, in particular because of the effects of both the magnetic nanomembrane/substrate interface and the nanomembrane free surfaces [73]. Hence, for the interface effect, the higher the stiffness contrast between the nanomembrane and the substrate, the greater the heterogeneity of the strains. Regarding the free surface, the effect is the opposite, *i.e.* the larger the free surface, the

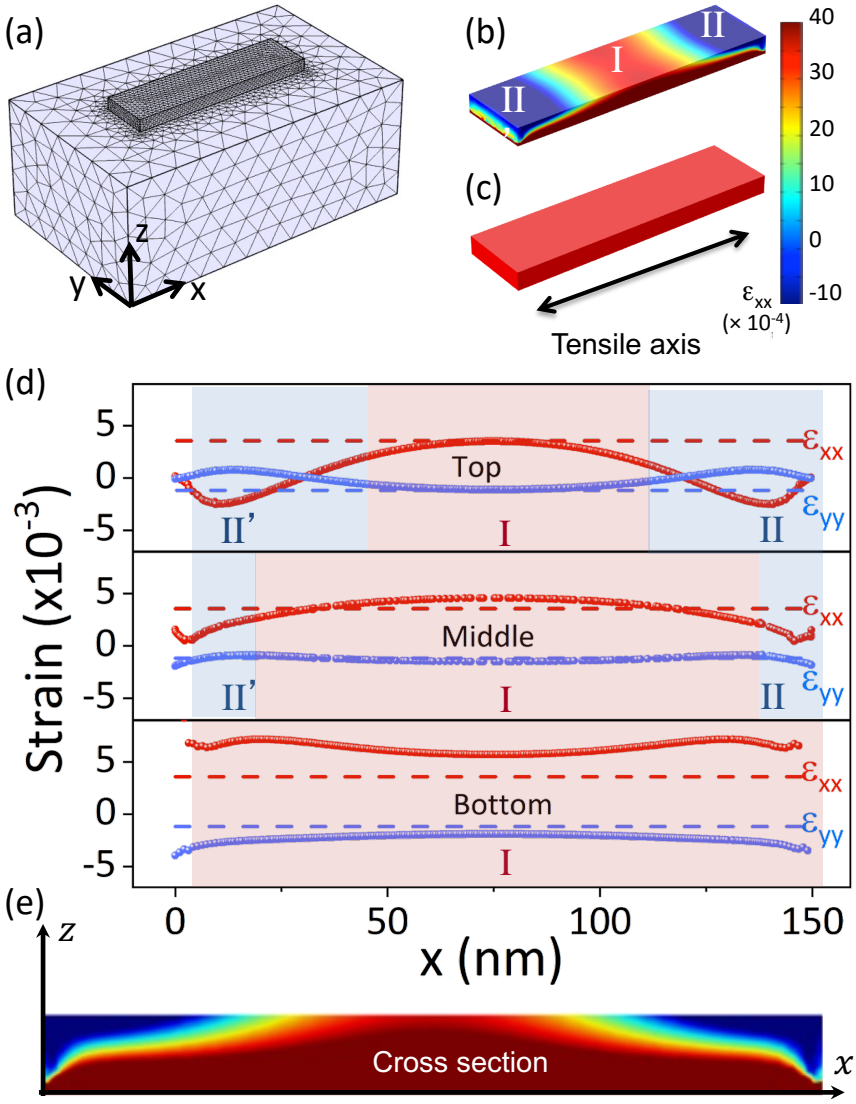

Figure 3.5: a) Modeled Ni/Ka nanomembrane and its finite element meshing. x, y and z denote the reference frame axes used in the whole study. b) Map of ε_{xx} component within the Ni nanomembrane induced by a displacement loading applied to the Ka substrate along x-direction ($\langle \varepsilon_{xx}^{substrate} \rangle = 4.10^{-2}$). (c) Map of ε_{xx} component within the self-supported Ni nanomembrane. The strain value in the self-supported Ni nanomembrane corresponds to the volume average value of the heterogeneous strain inside the Ni nanomembrane strained by Ka ($\langle \varepsilon_{xx} \rangle = 3.5 \times 10^{-3}$). (d) x-profiles of ε_{xx} and ε_{yy} at three different z-positions inside the Ni nanomembrane (top: $z = 0$ nm, middle : $z = 5$ nm and bottom: $z = 10$ nm), showing the heterogeneity in the plane but also the gradient in the thickness.(e) Mapping of the ε_{xx} along the magnetic nanomembrane.

lower the strain at the neighborhood [124]. At the moment, the influence of heterogeneous strain on the magnetic response of magnetic nanomembrane is not addressed. The reason for this missing knowledge is in the lack of platforms, which would allow such an analysis. Therefore, the development of numerical models accounting of these strain heterogeneities is essential for an accurate and reliable prediction and/or description of the static and dynamic magnetization behavior of magnetic nanomembranes[125].

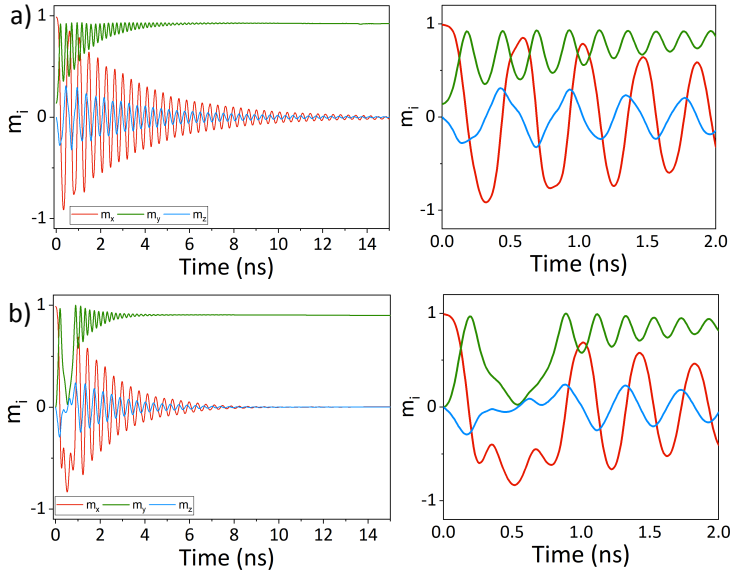

Figure 3.6: a) Temporal evolution of the average values of the magnetization components for heterogeneous (top) and homogeneous (bottom) strain distributions. For both cases, the mean strain components are same: $\langle \varepsilon_{xx} \rangle = 3.50 \times 10^{-3}$, $\langle \varepsilon_{yy} \rangle = \langle \varepsilon_{zz} \rangle = -1.05 \times 10^{-3}$. The right graphs zoom the early phase reversal (between 0 ns and 2 ns).

Here, we investigate the influence of strain heterogeneities on the magnetization reversal of a Ni nanomembrane. To make our results of immediate use for the application-oriented community working on flexible magnetic field sensors, we consider the case of Ni nanomembrane prepared on a polymeric foil with the typical parameters of polyimide (Kapton® (Ka)). Figure 6.6-a) shows the mesh size used during the calculation and its refinement within the magnetic nanomembrane. By comparison of the magnetization processes in heterogeneously strained nanomembrane to those in a free-standing one, we found out that the first stages of magnetization reversal is fully affected by strain heterogeneities.

Before addressing the micromagnetic simulations, the mechanical behavior of the two considered systems is first investigated. Figures 6.6-b) and 6.6-(c) show the spatial distribution of the mechanical strain within the nanomembrane for both the heterogeneous and homogeneous strain states. It can be observed that contrary to the self-supported

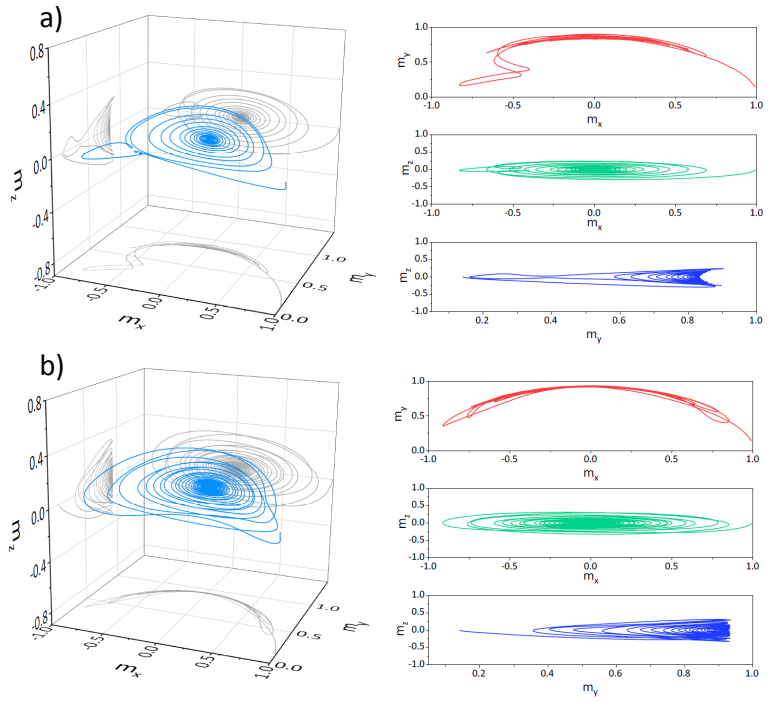

Figure 3.7: a-b) Trajectory of the mean magnetization vector corresponding to the temporal evolution of the average values of the magnetization components presented in figure 3.6 a): heterogeneously strained system and b): homogeneously strained system) . The different projections ($m_y(m_x)$, $m_z(m_x)$ and $m_z(m_y)$) are also presented (right graphs).

configuration, the supported nanomembrane displays distinguishable regions of different strain magnitudes and states. To make it clear and for a quantitative comparison, x-profiles of ε_{xx} and ε_{yy} inside the nanomembrane are represented in figure 6.6-(d) at three different z-heights (for $y = 0$) of the nanomembrane. In these graphs, the symbols and the dashed lines respectively refer to heterogeneous and homogeneous ε_{xx} and ε_{yy} x-profiles. As expected for the self-supported configuration, the strain profiles show that the nanomembrane undergoes the same ε_{xx} and ε_{yy} values everywhere within the nanomembrane. Unlikely, in the supported nanomembrane configuration, these x-profiles are clearly non-uniform and the strain values are position dependent within the nanomembrane. Regarding ε_{xx} distribution (showed also on figure 6.6-b)) large positive values are depicted in the central area (zone I), while the off-center areas are characterized by negative values on the top-face and slightly underneath (zones II and II'). Hence, the spatial strain distribution in the supported nanomembrane exhibits high strain gradient along its length and over its thickness. Moreover, it can be observed in the figure 6.6-(d) that the strain is almost uniform at the bottom-face (and slightly above). The influence of these strain distributions on the magnetic response of the studied system is addressed in

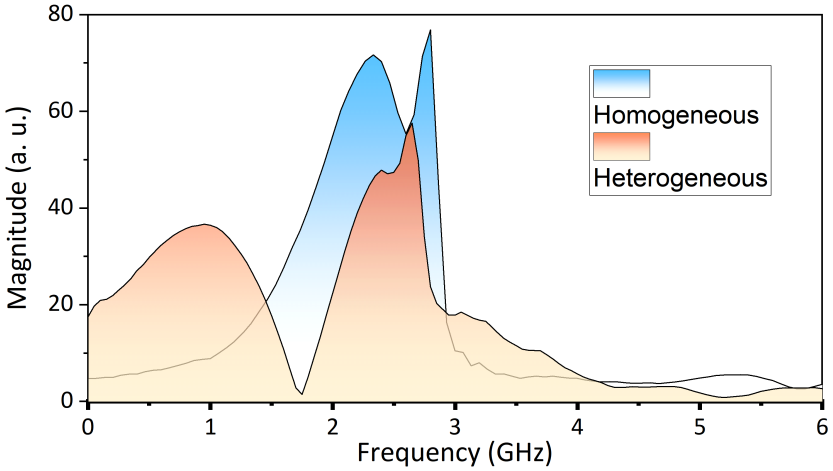

Figure 3.8: Fourier Transform performed on the m_x component in both configurations. This FFT corresponds to the cases illustrated in figure 3.6-a) and 3.6-b).

the following.
The dynamic magnetization of the nanomembrane under the influence of the acting strain, either uniform or non-uniform, and in absence of external magnetic field has been numerically characterized by solving the Landau-Lifshitz-Gilbert (LLG) equations coupled to the mechanical static equilibrium problem (mechanical dynamic effects were not taken into account in this study) [73]. Figure 3.6-a) shows the time-evolution of the mean magnetization components ($m_i = \frac{M_i}{M_S}$ where i denotes x, y or z and $M_s = 0.48 \times 10^6$ A.m^{-1} is the saturation magnetization of bulk Ni) for both strain states (between 0 ns and 15 ns). In these calculations,the gyromagnetic ratio is fixed to $\mu_0\gamma = 221017$ m.A^{-1}.s^{-1} the exchange stiffness to $A = 10 \times 10^{-12}$ J.m^{-1}; the Gilbert damping factor to $\alpha = 10^{-2}$ and finally the effective magnetostriction at saturation is fixed to $\lambda_{\mathrm{Ni}} = -30 \times 10^{-6}$. In addition, during our calculations, no external magnetic field is applied; the magnetization reversals that will be presented are solely due to the presence of a strain induced magnetoelastic field. Ni magnetoelastic behavior has been considered as linearly elastic and isotropic (which is the case at the macroscale for polycristalline Ni) [10, 107]. The strain distribution is first calculated within nanomembrane before running magnetic simulations that lead to a magnetoelastic field, which is time-dependent because of the temporal evolution of the magnetization distribution.

Figure 3.6-a) displays the temporal evolutions of the average values of the magnetization components. For both cases, one can observe a magnetization reversal from x-direction ($\vec{m} = (1, 0, 0)$ at 0 ns) to y-direction ($\vec{m} \approx (0, 1, 0)$ at 15 ns). In both cases, the magnetization reversal is due to an induced magnetoelastic field along y even if the strain is applied along x; which is due the negative magnetostriction of Ni. However, these temporal evolutions show a clear difference regarding the magnetization reversal process; in particular at the early phase (less than 1.25 ns of precession) before turning quite

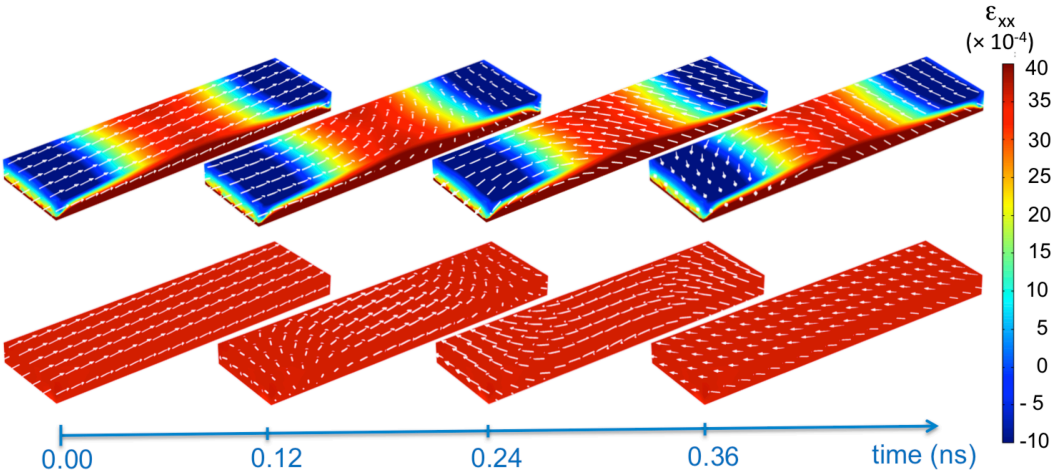

Figure 3.9: Maps of the magnetization distribution for heterogeneous and homogeneous cases, during the early steps of reversal (before the almost uniform precession phase). The color map shows the strain field in heterogeneous (top) and homogeneous (bottom) situations.

similar in term of oscillation frequencies. This magnetization reversal is also represented thanks to the trajectory of the mean magnetization vector in figures 3.7-a) and 3.7-b). It is worth mentioning that the equilibrium is reached earlier in the heterogeneous case (the magnetization oscillations are still visible at 15 ns for the homogeneous case where it is almost zero for the heterogeneous one), probably due to the higher localized magnetoelastic field in the zone I which acts as a nucleation area for the magnetization reversal. In fact, the reversal process seems to be progressive in the case of uniform strain, and rather abrupt in presence of heterogeneous strain. This difference in behavior is naturally explained by the heterogeneity of the internal effective magnetic field, which is as heterogeneous as the strain is. Indeed, the figure 6.6-b) shows distinct strain zones, which should influence the magnetization reversal.

To further illustrate this effect, a 3D spatial configuration of the magnetization reversal process during the first steps of reversal is proposed in figure 3 where the strain distribution is represented by color map and the magnetization vector by white arrows. One can note that the reversal process is fully different between the two cases. In particular, the magnetization switching is more coherent in the homogeneous case, with a spatial distribution that looks similar to that of the classical case of a magnetic ellipsoidal object, submitted to a homogeneous external field. Unlikely, the heterogeneous strain state leads to a more complex path. In this heterogeneous case, the reversal is initiated at the zone II, which is made possible by the strong tensile strain ε_{xx} close to the interface. Then it propagates to the central and opposite (zones I and II' in figure 6.6-b)) by exchange effect. This behavior is the source of the flutter effect observed at the early regime of the

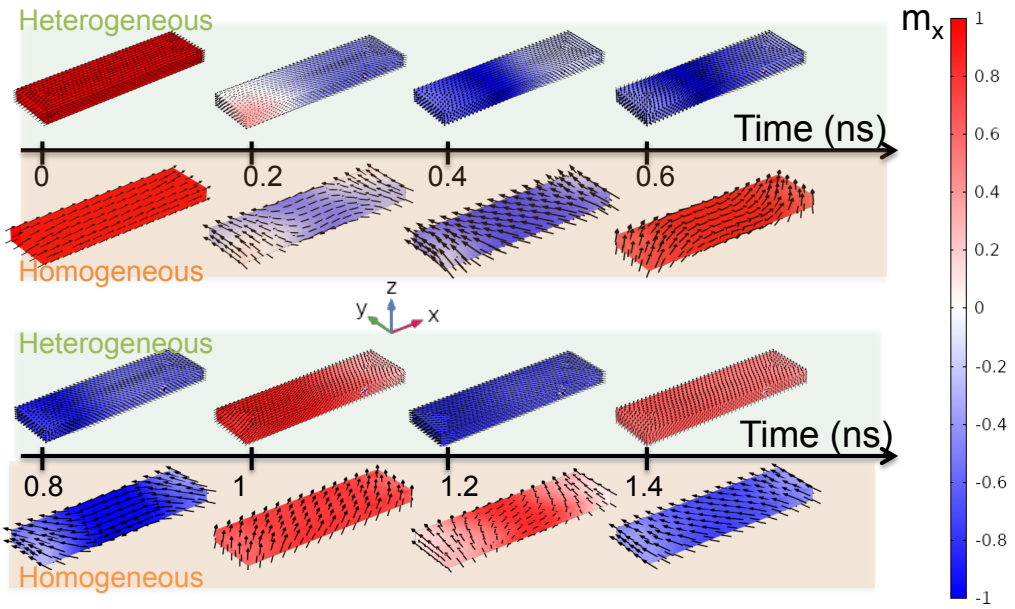

Figure 3.10: Magnetization distribution mapping for heterogeneous and homogeneous cases, during the early steps of reversal (before the almost uniform precession phase). The color map shows $x-$component of the magnetization.

average magnetization oscillations (before 1 ns), as displayed in figure 3.6-a). This dynamic instability is an important parameter to study since it modifies the magnetization reversal process, which is crucial for spintronic applications. Once the reversal has spread throughout the whole nanostructure (about 1.25 ns), a uniform regime of magnetization precession settles in, like in a homogeneously strained nanostructure.
Moreover, the differences in magnetization dynamics due to different strain distributions are also noticeable from an energy point of view. Actually, the Fourier transforms performed on the m_x for both cases (figure 3.8b)) reveal: i) a single principal intensity peak around 2.5 GHz for the uniformly strained nanomembrane (homogeneous case), ii) a secondary mode of lower frequency ($\sim$ 0.8 GHz) is depicted for the heterogeneous case besides the principal one at almost the same frequency ($\sim$ 2.5 GHz) as the homogeneous case but comparatively of lower magnitude. The occurrence of the "highest" frequency mode is assigned to the central zone of the nanomembrane, *viz* zone I in figure 6.6-b), undergoing the highest strain (high magnetoelastic anisotropy). The lowest frequency ($\sim$ 0.8 GHz) mode arises from the oscillations occurring in the nanomembrane region where the strain is lower because of the free-surface effect (zones II and II' of figure 6.6-b)) leading to a lower magnetoelastic anisotropy field. Thus, this structure, heterogeneous in terms of strain, behaves like an object whose internal field is not uniform (multido-

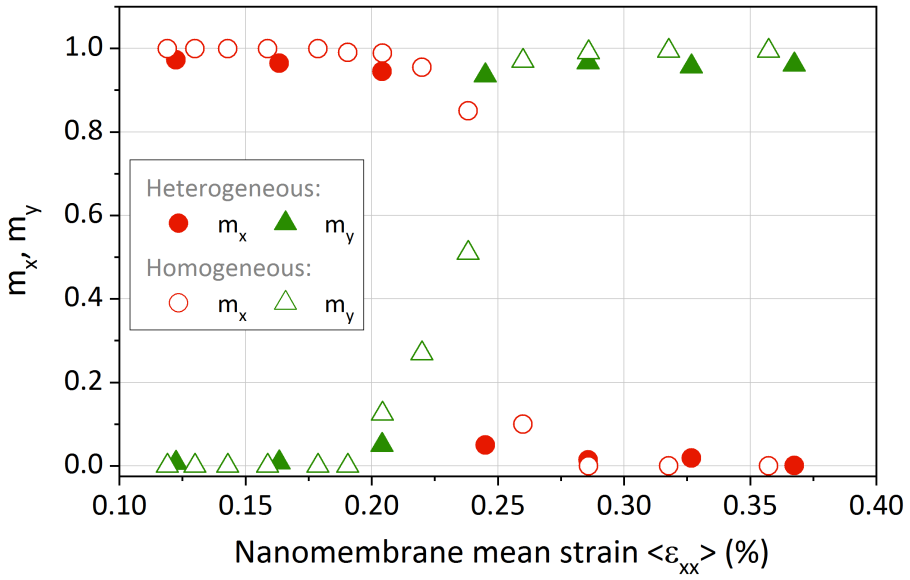

Figure 3.11: m_x and m_y values at equilibrium as function of the x-component of the mean strain $\langle \varepsilon_{xx} \rangle$ within the nanomembrane. Homogeneous and heterogeneous strain cases are represented by open and filled symbols, respectively.

main). Nonetheless, it is worth noting that the under spectrum areas for both cases standing as the magnetic energy, are almost the same (around 144 a.u. and 142 a.u. for the homogeneous and heterogeneous cases respectively). This suggests a conservation of the whole magnetic energy that seems to be dependent only upon the average imposed strain in the present study. Note that the strain heterogeneities are strongly dependent on the geometry of the magnetic structure. It is particularly the ratio of thickness to lateral dimensions that influences the heterogeneities in the plane and in the thickness [124]. In the case of realistic magnetic sensors, the dimensions are of the order of 100 nm in thickness and 1 μm in lateral dimension, a ratio that approaches the geometrical conditions of this work. We can therefore expect that the results of this work can be applied to magnetic sensors. Furthermore, the substrate thickness of flexible magnetic sensors can vary from 1 μm to 100 μm. In the case of very small substrate thicknesses, strain heterogeneity is still expected, but the strain transmission from substrate to the rigid magnetic structure will be much less important. The effect of substrate thickness on magnetization reversal will therefore be very much related to the average strain value. In addition to the study of magnetization reversal for a mean strain sufficient to generate this phenomenon ($\langle \varepsilon_{xx} \rangle = 3.50 \times 10^{-3}$), the study also concerned the determination of the critical applied strain for this reversal to take place. Several equilibrium calculations for variable average strains were performed for homogeneous and heterogeneous cases. These results are shown in figure 4. For the two cases, the same ratio between $\langle \varepsilon_{xx} \rangle$ and the two other components were kept the same ($\frac{\langle \varepsilon_{yy} \rangle}{\langle \varepsilon_{xx} \rangle} = \frac{\langle \varepsilon_{zz} \rangle}{\langle \varepsilon_{xx} \rangle} = -0.3$).

The equilibrium magnetization as function of the applied strain $\langle \varepsilon_{xx} \rangle$ in the nanomembrane was investigated in order to capture the critical strain value at which the reversal is favored. For this purpose, m_x and m_y components at the equilibrium state for each applied strain are reported in figure 4. It can be observed a very small difference regarding the critical values between the homogeneous and heterogeneous cases. Indeed, this critical value is around $\langle \varepsilon_{xx} \rangle = 2.4 \times 10^{-3}$ for both cases. This is due to the fact that the final equilibrium mainly depends on the mean internal magnetic field (here a competition between mean demagnetizing and magnetoelastic fields) and is only slightly affected by very local magnetoelastic field concentrations. The small discrepancies are probably due to slightly different magnetization distribution at equilibrium (heterogeneity effects at the edges, slight gradients in thickness in zones II and II', etc).
In conclusion, the effect of strain heterogeneity on the magnetization reversal in a nanomembrane was investigated in this work. The findings show that the heterogeneous strain field has a strong influence on the dynamic reversal, and more particularly at the initial stages. Indeed, a more abrupt initiation of the magnetization reversal is observed for the heterogeneous case with the appearance of a secondary mode at a lower frequency. However, the study of the equilibrium as a function of the applied mean strain shows that the heterogeneity weakly influences the final equilibrium configuration of the magnetization. The numerical simulations suggest that the heterogeneous strains, which generally arise in deformed nanomembranes, has a significant effect on the magnetization dynamic properties but much less on the static ones which mainly depend on the global mean internal magnetic effective field.

4 Experimental methods

Contents

During this thesis, the magneto-mechanical properties of thin films and nanostructures have been mainly studied through broadband ferromagnetic resonance (FMR) spectroscopy measurements combined with *in situ* micro-mechanical testing. As explained in the introduction, our systems are magnetic thin films or arrays of magnetic nanostructures deposited on polymer substrates. The micro-mechanical testing are performed by cementing our systems on $PbZr_{1-x}Ti_xO_3$(PZT) actuators. As a consequence, this chapter is devoted to the presentation of the setup used during this thesis that combines FMR measurements and mechanical testing as well as to the presentation of the nanofabrication methods used to obtain arrays of magnetic nanostructures.

4.1 *In situ* ferromagnetic resonance spectroscopy

In this section, we succinctly present the ferromagnetic resonance setup before presenting some details on how we applied elastic strains to our systems (magnetic thin films and nanostructures) during this thesis.

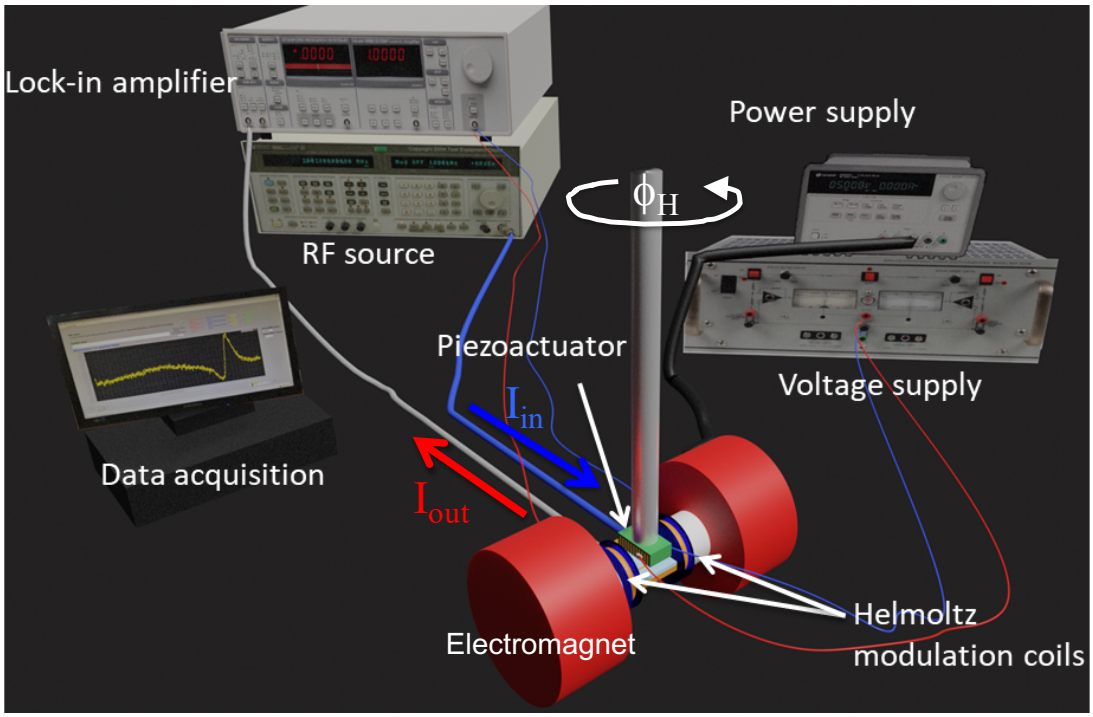

Figure 4.1: a) Sketch of the FMR setup used during this thesis showing the principal components of the setup. Illustrative image showing a magnetic thin film/Kapton®/PZT-actuator system inside the electromagnet used during the FMR measurements. The support on which the system is placed allows modifying the angle between the applied magnetic field and the studied sample. I_{in} and I_{out} corresponds to the current injected to the microstripline and the output one, respectively. This last one is finally connected to a Schottky to convert it into voltage for the demodulation through the lock-in amplifier.

4.1.1 Generality

The ferromagnetic resonance (FMR) spectroscopy is the oldest and most widely used technique to date to study the magnetization dynamics in thin ferromagnetic films and nanostructures. This technique consists in placing the magnetic sample in a resonant cavity in the microwave range[18, 81]. The working frequency is then fixed: it is that of an eigen-mode of the cavity (typically from 1 GHz to 100 GHz). The cavity is supplied *via* a waveguide at the working frequency and the reflected power is measured as a function of an external applied magnetic static field. When the frequency of the magnetic mode considered coincides with the working one, the power absorbed has a maximum, which corresponds to a minimum of reflected power[126, 127, 128]. The main advantage of this technique is its sensitivity. In fact, despite the small volume occupied by the magnetic material, the quality factors of a few thousand achieved for this type of cavity have made it possible to measure the dynamics of magnetic layers whose thickness is of the order of a nanometer. Note however that this technique has the disadvantage of a fixed working frequency, and limits for example the broadband study of the magnetic damping phenomenon of thin films or the study of quantized magnetic modes in nanostructures. Another disadvantage of this FMR cavity technique is that the cavity makes it very difficult to carry out *in situ* measurements with actuators (such as the ones used during this thesis) due to the geometrical confinement.
This is the reason why we have adopted a broadband (0.01-20 GHz) FMR technique despite its lower sensitivity, as compared to this "classical" setup, to study the magneto-mechanical properties of our thin films and nanostructures. Actually, our broadband FMR offers a sensitivity allowing to detect a net magnetic moment down to 10^{-5} emu which is sufficient to detect a signal in our systems. Furthermore, since we aspire to study the magneto-mechanical properties of magnetic thin films and nanostructures, our magnetic systems have been cemented onto PZT actuators that have been mechanically characterized by using a non contact optical technique (namely the Digital Image Correlation (DIC) technique developed during M. Gueye's thesis[**?**])[10, 16, 24]. More technical characteristics are given in the following subsections.

4.1.2 Technical characteristic of the FMR setup

The basic components of our FMR spectrometer are shown in figure 4.1. The excitation of the sample magnetization is performed thanks to a microstripline (with an impedance $Z = 50\ \Omega$ to avoid losses)[129, 130, 131]. Indeed, a synthesized sweeper (rf-source in the figure 4.1) generates microwaves that travel down a coaxial cable to the microstripline where some of microwave energy are absorbed by the specimen. The microstripline is placed inside a 3 kOe electromagnet which supplies the required uniform dc magnetic field $\vec{H}_0$. The sample is placed at the top surface of the microstripline where the rf magnetic field $\vec{h}_{rf}$ is supposed almost homogeneous (even if it is more complex as it can be seen in figure 4.2-a). The transmitted microwave beam travels back along the coaxial cable to a Schottky diode whose output voltage, V_t, is a function of the amplitude of the transmitted microwave electric field. The data collection system is dedicated to

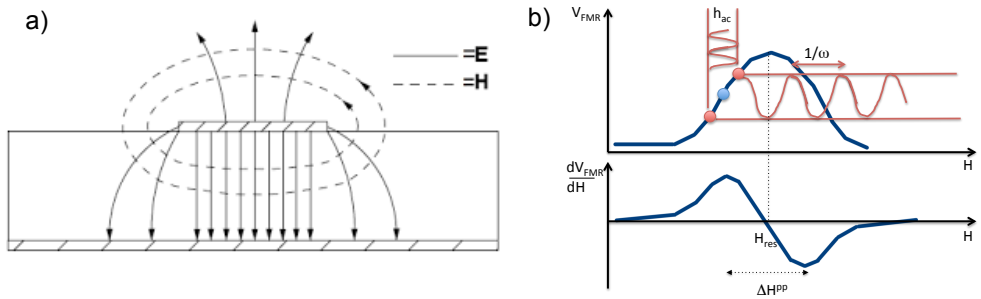

Figure 4.2: a) Sketch of the cross section of a microstipline showing the rf magnetic and electric fields generated when a rf current is applied. b) Illustration of the modulation of the dc magnetic field H_0 by an ac one h_{ac}; let us consider the value H_0 at the blue point, the detected signal (down graph) is periodic and reflect the excursion of V_{FMR} around the blue point (between the two red ones).

measure the variation of this diode voltage as a function of the applied magnetic field $\vec{H}_0$. The variations in the diode voltage that are due to changes in the energy absorption by the magnetic sample as $\vec{H}_0$ is swept through $\vec{H}_{res}$ are small and superimposed to a large constant background. In order to emphasize the variations of V_t with $\vec{H}_0$, the applied dc field is weakly modulated thanks to an ac magnetic field $h_{ac} \simeq 5$ Oe at 170 Hz (see modulation coils in figure 4.1) and a lock-in amplifier is used to detect and amplify the 170 Hz component of the diode voltage. After demodulation, the resulting signal corresponds to the derivative of the absorbed power. Then, the output of this amplifier is connected to a data collection computer. A control program is written using the LABVIEW graphical programming language. The program provides flexibility for a real time control of the magnetic field sweep direction, sampling time, data acquisition in real time and visualization. Therefore, the microwave frequency is kept constant and the applied magnetic field is varied over a field range in which microwave absorption is expected.

In these conditions, with this setup, we measure the derivative of the microwave absorption power absorbed by a specimen as function of an applied dc magnetic field $\vec{H}_0$, i.e. the derivative of a Lorentzian curve as schematically presented in figure 4.2-b). The resulting curve is described by a resonance field, H_{res}, that corresponds to maximum power absorption, and by a peak to peak absorption linewidth, ΔH^{pp}. The FMR (derivative) absorption signal of a ferromagnetic thin film is a function of the applied field H_0 and intrinsic magnetic properties of the film. The latter include the magnetic anisotropies, the spectroscopic $g-$factor, the magnetic damping parameter (that is responsible for the finite linewidth ΔH^{pp}), and the quantity of interest such as the saturation magnetization M_S or exchange stiffness A. A typical FMR spectra is represented in figure 4.2-b) that

illustrate the effect of the modulation technique. As a resume, the measured signal is proportional to:

$$\frac{1}{2}\frac{\mathrm{d}V_{FMR}(\vec{H}_0)}{\mathrm{d}H_0}h_{ac}\cos(\phi) \tag{4.1}$$

where $V_{FMR}(H_0)$ corresponds to the FMR absorption signal which depends on the (static) applied magnetic field H_0 and ϕ corresponds to the phase of the weak modulation magnetic field $h_{ac}(t) = h_{ac}\cos(\omega t + \phi)$. As a result, one can see that the amplitude of the obtained signal is proportional to h_{ac}. We could be tempted to increase this field in order to ameliorate the signal to noise ratio, but it should be kept in mind that this latter must indeed remain weak in front of the H_0 field so that this field remains a modulation field on the one hand and on the other hand because it can artificially increase the linewidths of the spectra. With our setup, we have experienced that this field should not be higher than 5 Oe in order to be influenceless in the linewidth spectra. In equation 4.1, we also note that the measured signal is proportional to $\cos(\phi)$ that can be controlled by the low frequency generator of the lock-in (we indeed used the lock-in to modulate and demodulate the absorption signal). This phase is determined during the calibration process for each sample in order to find the phase angle resulting in a maximum signal intensity of the spectra.
In addition to this phase, the lock-in allows us to choose a time constant and a sensitivity that can affect the signal to noise ration if those parameters are not well chosen. The time constant is the integration time of the signal at the output of the lock-in, therefore at a given frequency. The time constant should be much larger than the period of the output signal (generally 300 ms with our setup). Concerning the sensitivity, it allows measuring weak signals, however, the flip side is that it decreases the signal to noise ratio. Finally, another way to increase the signal is not seen directly in equation 4.1 but is in fact hidden in the $V_{FMR}(\vec{H}_0)$ part. Indeed, it corresponds to the absorption of the microwave power by the samples which is in first approximation proportional to the magnetization precession amplitude. Thus by increasing the excitation rf field $\vec{h}_{rf}$ (by increasing the I_{rf}^{in} power, see figure 4.1-b)), one can increase $V_{FMR}(\vec{H}_0)$. Indeed, the amplitude $V_{FMR}(\vec{H}_0)$ strongly depends on the amplitude of the torque exerted by $\vec{h}_{rf}$ on the sample magnetization. However, a too higher torque can lead to (undesired) non linear effect (increasing of the ΔH^{pp} or generation of low-wave vector spin waves,...)[132, 133, 134].

4.1.3 Strain characterization

The magneto-mechanical properties of the different thin films and nanostructures studied during this thesis have been probed by performing FMR measurements under applied elastic strains. These strains have been applied thanks to a PZT actuator on top of which the system constituted by a magnetic film (or array of nanostructure) deposited onto a polymer substrate has been cemented. This methodology has already proved its worth during M. Gueye's thesis [**?**] and it makes it possible to finely control the elastic

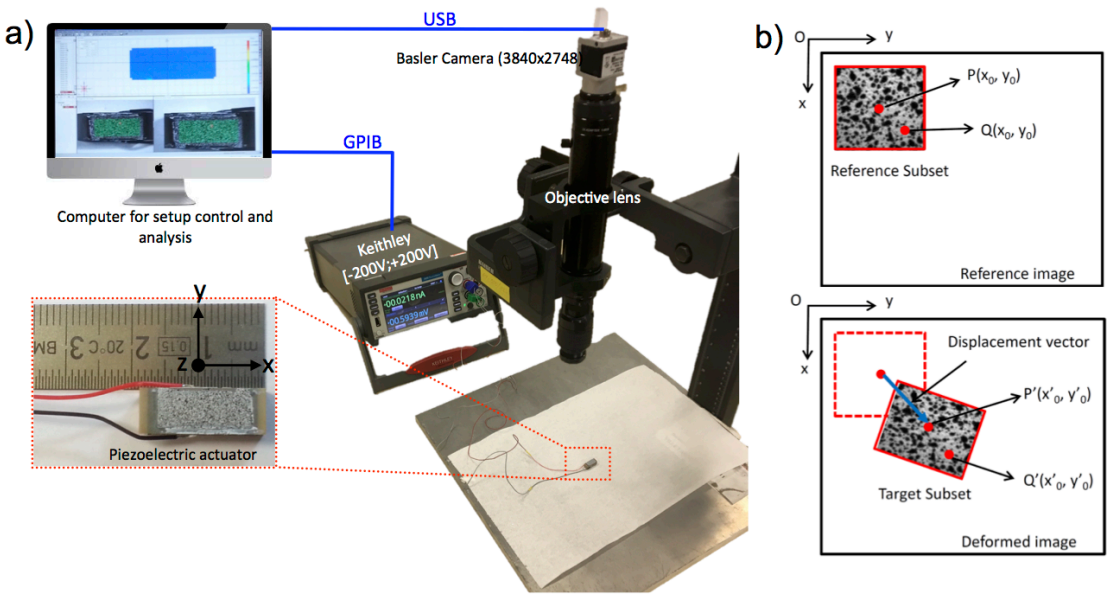

Figure 4.3: a) Digital image correlation setup. The electric field inside the actuator is generated thanks to a voltage applied by using a KEITHLEY bipolar power supply. The ARAMIS software is used to analyze the images. The zoom-in is a picture showing the ferromagnetic thin film cemented on the actuator with a randomly speckle pattern of the system. b) Schematic illustration of reference square subset before deformation and a target subset after deformation..

strains applied to the system. In the case of thin films, the strains are measured thanks to Digital Image Correlation (DIC) technique. Thereby, the film/polymer substrate systems are cemented thanks to an epoxy glue (resin and harder) on top of commercially available ferroelectric actuators (PZT) with dimensions $1.8\times0.7\times0.7$ cm^3, as shown in figure 4.3-a). A voltage applied across the actuator results in its deformation which is then transferred to the film. A good contact between the film/substrate and the actuator is necessary in order to completely transmit the in-plane strains. Owing to the converse piezoelectric and electrostrictive effect inherent in PZT, a mechanical expansion (resp. contraction) along the dominant elongation direction (along x-axis) when a positive (resp. negative) voltage is applied across it. In particular, a positive voltage results in an elongation with a related uniaxial strain $\varepsilon_{xx} > 0$ along x. Due to elasticity, this tensile strain is accompanied by compressive strains $\varepsilon_{yy}, \varepsilon_{zz} < 0$ along the orthogonal in-plane direction y and the orthogonal out-of-plane direction z. To convert the voltage applied across the PZT actuator into strains, we have developed a Digital Image Correlation (DIC) setup. DIC is a non-contact and *a priori* non-destructive optical technique for microscale even nanoscale surface displacement and strains of an object under different loading conditions. In DIC, a single camera (2D-DIC) or even a couple of camera (3D-DIC) is used to determine the displacement and strain of a planar or non-planar surfaces. It works by doing comparison of set of digitized images of a surface at two different states before deformation (reference image) and after deformation. However, to achieve this, the surface of the studied object has to be randomly spray-painted in order to have a random pattern or must have an intrinsic pattern at its surface. An area of interest on the surface of the specimen is selected and subdivided into subsets. Typically, a reference subset of $(2M+1)\times(2M+1)$ pixels centered at the current point $P(x_0, y_0)$ from the left image is chosen to find its corresponding location in the right image. Once the location of the target subset in the right image is found, the disparities of the reference and target subset centers can then be determined. As schematically shown in figure 4.3-b), a set of neighboring points in a reference subset within the left image are assumed to remain as neighboring points in the target subset within the right image. Thus, it is reasonable to assume that each of these points $Q(x, y)$ around the subset center $P(x_0, y_0)$ in the reference subset can be mapped to point $Q'(x', y')$ in the target subset. Myriad of commercial and laboratory-made softwares based on digital image correlation are available (Granu [135], Sept D [136], Ncorr [137], Moire [138], Matchid [139], Correli [140], Correla [141],...), among them the Aramis [142, 143] and Correla [141] have been used in this manuscript.
This technique has been simple to set up. The only constraint is that the samples must be previously spray-painted. Indeed, for the DIC calculations, the specimen surface must have a random gray intensity distribution (*i. e.* random speckle pattern). It is important to point out that the spatial resolution is related to the grain size; the smaller the grain the higher is the resolution. Moreover, whatever the specimen and loading conditions, the grains have to be fixed and well-adherent in order to facilitate the follow-up of the material deformation. Therefore, the surface of the studied object has been randomly spray-painted in order to have a random pattern consisting of black and white random grain field as shown in figure 4.4-a). Our setup is schematically presented in figure 4.3-

a). As shown in this figure, the PZT actuator is connected to a Keithley power supplier allowing to apply DC voltages in the range [−200 V;+200 V] with 0.001 V resolution. For each applied voltage, an image of the top surface of the sample is recorded. The images, which will serve to determine the in-plane field strains as function of the applied voltage, are recorded thanks to a 3840×2748 pixels CCD Basler camera vertically positioned at the top of the surface sample. The objective lens has been chosen to have a field view of around 1×1 cm^2. A first image (reference image) is taken at zero applied voltage; then, a sequence of images is taken at different applied voltages and is compared to the reference. Then, the field strain at the surface of the system is extracted for each applied voltage by performing DIC calculations, which are performed by using the reference image and the different images coming from the sequence. The DIC calculations have been performed by using ARAMIS and CORRELA that are commercially available software packages [141, 142]. From the field strains, the mean in-plane strains are extracted as function of the applied voltage. When performing our experiments, images are collected by applying voltages using the following path: 0 V to 100 V and 100 V to 0 V. The frame is generally of about 0.1 FPS; the step of applied voltage can also be varied. Furthermore, we have estimated statistical errors of our DIC setup by measuring several images in absence of applied voltage; it is estimated to be around 5×10^{-6}. Moreover, different images have been taken as a function of time at 0V after saturating the actuator at 100 V. After approximately 5 h, a difference of about 4×10^{-5} in the in-plane strains values is found; this value rises to 1×10^{-4} after several days (which is relatively high). This difference is due to training effect of the actuator polarization[17].

Now, we present results obtained from a magnetic film (20 nm)/Kapton® (125 μm) system cemented onto a PZT actuator. We have employed our technique to measure in-plane strains in this system. The voltage was applied from 0 V to 100 V and 100 V to 0 V with a 2 V step. Afterwhat, ARAMIS has been used to calculate the DIC in two different (around 2×5 mm^2) regions: an uncoated area of the actuator and an area located at the top of the film (see figure 4.4-a)). Figure 4.4-b) presents the extracted mean in-plane strains ε_{xx} and ε_{yy} from these two regions. It is interesting to note that similar homogeneous (the maps are not shown here) strain fields as function of the applied voltage have been calculated from these two regions. Thus, we can conclude that a 100% in-plane strain transmission in between the PZT actuator and the film is observed. Non linear variations are observed for both ε_{xx} and ε_{yy}, which is due to the intrinsic properties of the ferroelectric properties of PZT. One can note that ε_{xx} is found to be positive and ε_{yy} is found to be negative in the voltage range [0–100 V]. Moreover, it is interesting to note that a linear variation of ε_{xx} as a function of ε_{yy} is found $\varepsilon_{xx} \simeq -0.65\varepsilon_{yy}$. The maximum achieved values of ε_{xx} and ε_{yy}, (1×10^{-3} and -0.5×10^{-3} at 100 V, respectively) show that the film is not deteriorated by the plasticity regime because it is obtained for higher values: this is experimentally confirmed by the excellent reproducibility (see figure 4.4-c)) of the experiments (even after several days). Finally, note that the shear strains are found to be negligible and will be neglected thereafter in the rest of the manuscript. Obviously, to interpret the FMR results thereafter, we use the mean values of the elastic strains.

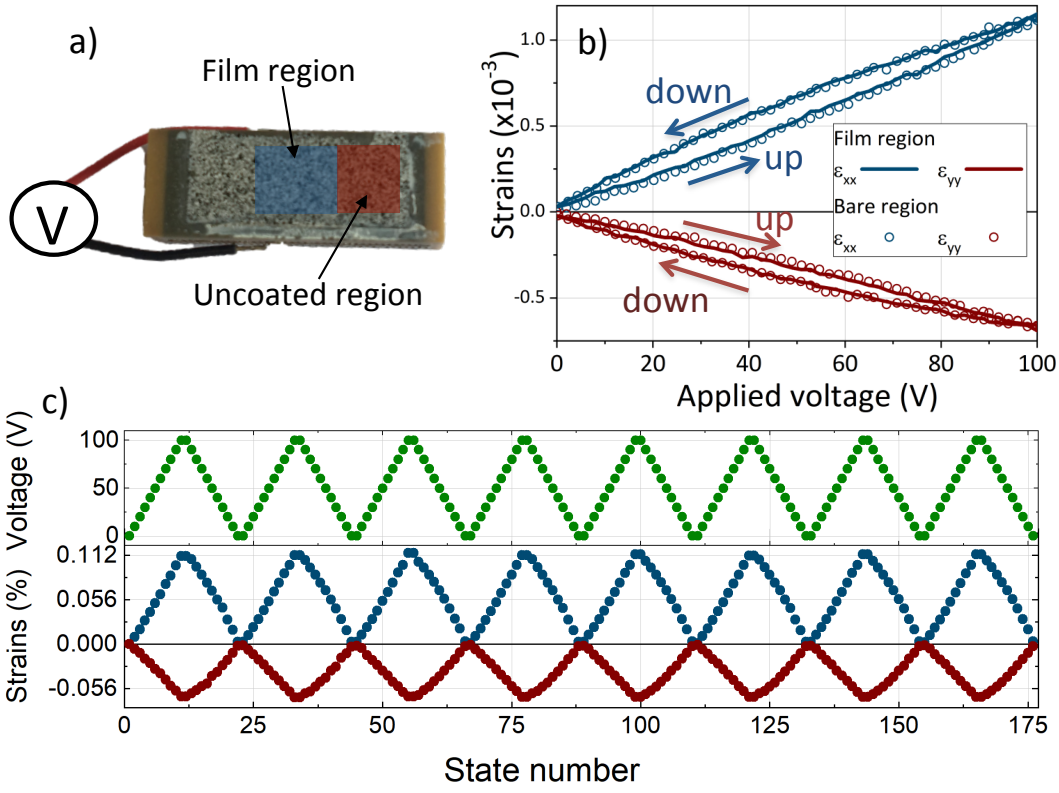

Figure 4.4: a) Sketch showing the selected region of interest on the surface of the film and actuator for the analysis of the strain transmission. b) Mean in-plane strains (ε_{xx} and ε_{yy}) in the film and actuator regions as function of the applied voltage (0 to 100 V and 100 V to 0 V). c) Mean in-plane strains (ε_{xx} and ε_{yy}) calculated in the film region for a repeating number of non-symmetrical path (0 V to 100 V and 100 V to 0 V).

4.2 Illustrative example: CoFeB/Pd bilayer system

In this section, we present a study realized on CoFeB/Pd system deposited either on Kapton® (125 μm) or Silicon (500 μm) substrates. The series is characterized by a fixed CoFeB thickness of 6 nm while the Pd thickness varies from 2 to 30 nm. This series of samples allows studying the spin pumping phenomenon at the interface between the Pd and Co layer which is currently of great interest in the magnetism community. Indeed, spin pumping is an efficient method to generate a spin current and therefore to tune the magnetic damping. Spin pumping is found in magnetic film/non-magnetic metallic film systems such as CoFeB/Pd system. The magnetization precession in the magnetic layer generates spin in the non-magnetic layer through the interface by means of exchange. A spin accumulation is then generated in the metallic layer and extends over a characteristic length called the spin diffusion length (ℓ_{SD}). This is one of the means of generating spin

current used in spintronic devices. Indeed, there are other ways of producing a purely spin-polarised current such as the transfer of the spin moment, spin Hall effect, optical angular momentum transfer,... As a resume, we can say that spin pumping is a widely used method because it consists of a magnetization excitation that can produce a spin current without electric charges transfer. This make possible to manufacture electronic devices with high performance and reduced energy consumption. Indeed, in this process only the spin moment is transferred which results on a zero Joule effect during this process. It is not a question here of entering into the detailed theoretical description nor of demonstrating the effectiveness of this process, works have already shown the effect of this spin pumping, the optimization of the efficiency of the process and the influent parameters on it. The objective here is to present a standardized FMR study on a similar system deposited either on a rigid or flexible substrate to show the performance of our FMR setup.

4.2.1 Theoretical background

Actually, the damping is related to the FMR linewidth through the following relation[129, 144]:

$$\Delta H^{pp}(f) = \Delta H_0(f) + \Delta H_{Gi}(f) \tag{4.2}$$

Where $\Delta H^{pp}(f)$ represents the frequency evolution of the peak-to-peak linewidth directly measured on FMR spectra. This linewidth can be decomposed into two contributions: $\Delta H_0(f)$ that is the intrinsic linewidth (itself composed of several contributions) and the Gilbert contribution $\Delta H_{Gi}(f)$ that is related to the spin-pumping phenomenon, respectively. The Gilbert contribution is frequency dependent and takes the form[24, 129, 145, 146]:

$$\Delta H_{Gi} = \frac{2}{\sqrt{3}} \frac{2\pi}{\gamma} \alpha f \tag{4.3}$$

The multiplying factor $1/\sqrt{3}$ is the correction between the full width at half maximum and the peak to peak linewidths for the line shape of a Lorentzian. The former relation include the intrinsic damping and the spin pumping torque on the damping of the precessional motion of the magnetization. So, the Gilbert damping takes the form[147]:

$$\alpha = \alpha_{int} + \alpha_{pump} \tag{4.4}$$

The right side in the damping equation gives the two contributions to the relaxation phenomenon. The first one is related to the material, α_{int}, the second one is related to the spin pumping process. The first one can be extracted from the frequency evolution of the linewidth using the formula 4.2, the second one, α_{pump}, is related two the magnetic layer thickness through[144, 145, 148]:

$$\alpha_{pump} = \frac{g\mu_B g_{eff}^{\uparrow\downarrow}}{M_S} \frac{1}{t_{FM}} \left(1 - e^{-\frac{2t_{\mathrm{Pd}}}{\ell_{SD}}}\right) \tag{4.5}$$

where g, μ_B, $g_{eff}^{\uparrow\downarrow}$, M_s and t_{CoFeB} the Landé factor, the Böhr magneton, the effective spin-mixing conductance, the saturation magnetization and the CoFeB film thickness,

respectively. Then, one can conclude that the spin pumping effect can be characterized by following the evolution of the damping as function of the Pd thickness.
In addition, equation 4.5 also gives the spin pumping efficiency through the spin-mixing conductance $g_{eff}^{\uparrow\downarrow}$. Indeed, this factor tells us about the scattering in the interface and the rate of the spin moment torque injected through this later. This characteristic is important in spin transport application like spin information processing devices based and spin transfer devices. As defined bellow, the spin pumping in the present structure, composed of a ferromagnetic film adjacent to heavy metal film with high spin-orbit coupling, results in a spin accumulation near the interface during the spin-pumping process. This accumulation is characterized by a characteristic length called spin-diffusion length and noted ℓ_{SD}. This characteristic length is the mean length between two successive spin-flip events.

4.2.2 Spin pumping and magnetization dynamics studied by FMR

CoFeB(6nm)/Pd(t) bilayers were grown at room temperature on thermally oxidized Si and on Kapton® substrates at rates of around 0.07 nm/s in a chamber with a base pressure lower than 2×10^{-8} Torr, the Ar working pressure during sputtering was 1mTorr. The series consists in a 6 nm thick CoFeB film capped by a Pd layer of various thicknesses ($t_{\mathrm{Pd}} = 2, 4, 6, 8, 12, 20$ and 30 nm). This series allow the determination of both the spin mixing conductance ($g_{eff}^{\uparrow\downarrow}$) and of the spin diffusion length (ℓ_{SD}) through the analysis of the FMR linewidth as function of t_{Pd}. As seen in the small introduction paragraph, the determination of $g_{eff}^{\uparrow\downarrow}$ and ℓ_{SD} requires knowing precisely the saturation magnetization M_S and the Landé factor (g) that is related to the gyromagnetic ratio γ. The $g$values can be easily obtained by performing out-of-plane FMR measurements. Indeed, in first approximation, the uniform mode frequency in out-plane-plane geometry for a thin film is simply equal to[24]:

$$f_{\perp} = \left(\frac{\gamma}{2\pi}\right)(H - 4\pi M_{eff}) \tag{4.6}$$

In this equation, $4\pi M_{eff} = 4\pi M_s - H_{\perp}$ where $H_{\perp}$ is an out-of-plane magnetic anisotropy. The g-values are then obtained by determining the slopes of the different experimental out-of-plane frequency dependencies since the slopes correspond to $\gamma/2\pi$. The analysis of the different slopes in the out-of-plane $f(H)$ dependencies give a γ value that is almost thickness independent and therefore, a unique value of $\gamma = 31.3$ GHz.kOe^{-1} will be used during our analysis. Concerning M_S, it should be noted here that the precise determination M_S with solely FMR measurements is almost impossible because it is difficult to discriminate an out-of-plane magnetic anisotropy from the demagnetizing field resulting from the geometry of the thin film geometry ($H_{demag} = 4\pi M_S$). This is the reason why we have combined our FMR data with VSM (Vibrating Sample Magnetometry) measurements. From VSM measurements, we found a saturation magnetization of about $M_S = 800 \pm 50$ emu.cm^{-3} for all films and we have deduced from the FMR measurements the presence of a more or less weak out-of-plane anisotropy (around 0.3

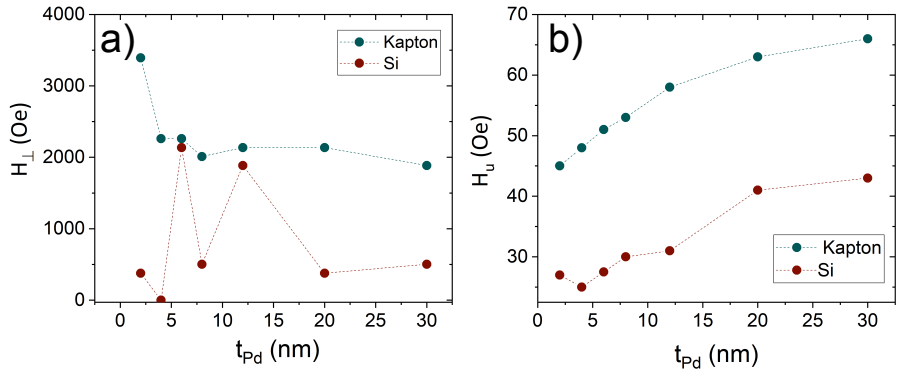

Figure 4.5: Variation of $H_\perp$ (a) and H_u (b) as function of the Pd thickness for the CoFeB/Pd bilayers on Si and Kapton substrate deduced from the out-of-plane frequency dependencies (a) and from the in-plane angular dependencies (see figure 4.6). The dashed lines are guide for the eyes.

kOe for Si substrate and 2 kOe for Kapton® substrate) which will not be discussed later because of its random character as function of the Pd thickness and because it does not enter in consideration in the determination of $g_{eff}^{\uparrow\downarrow}$ and ℓ_{SD}. Figure 4.5-a) presents the variation of the $H_\perp$ as function of the Pd thickness; as previously discussed, the films deposited on Kapton® present a more intense out-of-plane anisotropy that is most probably due to the presence of roughness at the Kapton®/magnetic interface that leads to an inhomogeneity of the demagnetizing field and in fine to a lower out of plane resonance field.

As presented in the small introduction of this section, the spin pumping phenomenon can be "directly" measured though the analysis of the in-plane FMR linewidth that is related to the magnetic damping. This last parameter controls the speed at which the magnetization of a ferromagnetic medium can be reversed or reoriented and therefore constitutes an important technological parameter. Information on damping, and therefore on the relaxation mechanisms, can be obtained by measuring the FMR linewidth in the small magnetization precession amplitude regime. Indeed, the FMR linewidth is caused by two mechanisms: the intrinsic damping (the so-called Gilbert damping) of the magnetization and extrinsic contributions (such as two magnons scattering, mosaicity, ...). Generally, only the extrinsic contributions are eventually tunable. The deconvolution between intrinsic and extrinsic contributions can be done by performing in-plane angular and frequency dependencies FMR measurements. Indeed, the Gilbert damping contribution to the linewidth is in principle isotropic while the extrinsic ones depend on several parameters such as the thickness of the films, their crystallinity, ... that can be separately determined by finely analyzed the angular and frequency dependencies of the FMR linewidth. However, since the aim of this illustrative study is the determination of $g_{eff}^{\uparrow\downarrow}$ and ℓ_{SD}, we will simply choose the in-plane direction where these extrinsic contributions are the weaker to determine the apparent damping parameter assuming that *in fine* they will be almost zero (or very minimal). However, we will see that this assumption

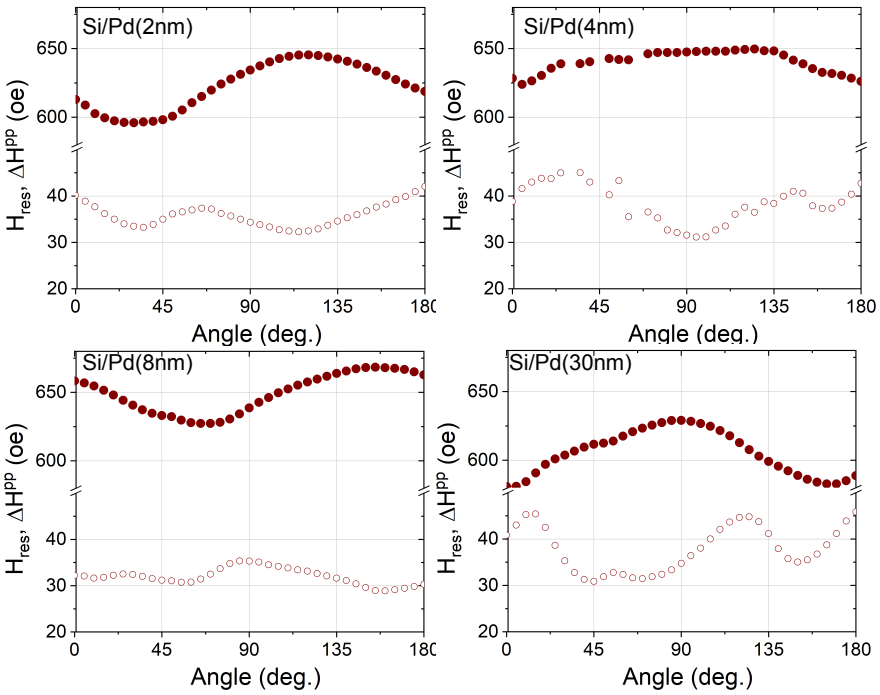

Figure 4.6: Variation of the resonance field (H_{res} in filled symbols) and of the peak to peak FMR linewidth (ΔH^{pp} in open symbols) as function of the in-plane angle for different values of the Pd thickness (2, 4, 8 and 30 nm) for the CoFeB/Pd bilayers on Si substrate. The driving driving frequency is fixed at 8 GHz.

is not totally justified for the systems deposited on Kapton® probably because of the higher roughness of the films when Kapton® is used as a substrate. Figure 4.6 presents typical in-plane angular dependencies of the uniform precession mode: resonance field H_{res} as function of φ_H (filled red symbols) and the associated linewidth ΔH^{pp} variation as function of φ_H (open red symbols). For clarity, only data from the Si substrate are represented. One can note the presence of a uniaxial anisotropy field in all cases, the evolution of this in-plane uniaxial anisotropy H_u amplitude as function of t_{Pd} is represented in figure 4.5-b) for both substrates. One can note higher values for the system deposited on Kapton® as compared to the system deposited on Si. Indeed, for a Pd thickness of 30 nm, we measure $H_u \simeq 65$ Oe and $H_u \simeq 40$ Oe, respectively. Gueye et al. [**?**] already observed this phenomena in ferromagnetic films deposited on polymer substrate and they correlate this effect to to the magnetostriction character of the ferromagnetic medium combined with the slight curvature of the substrate during deposition and eventually during subsequent manipulations. This phenomenon, although slight, induces an important in-plane anisotropy field if the magnetostriction is significant.

The associated frequency dependencies for a magnetic field applied along this in-plane

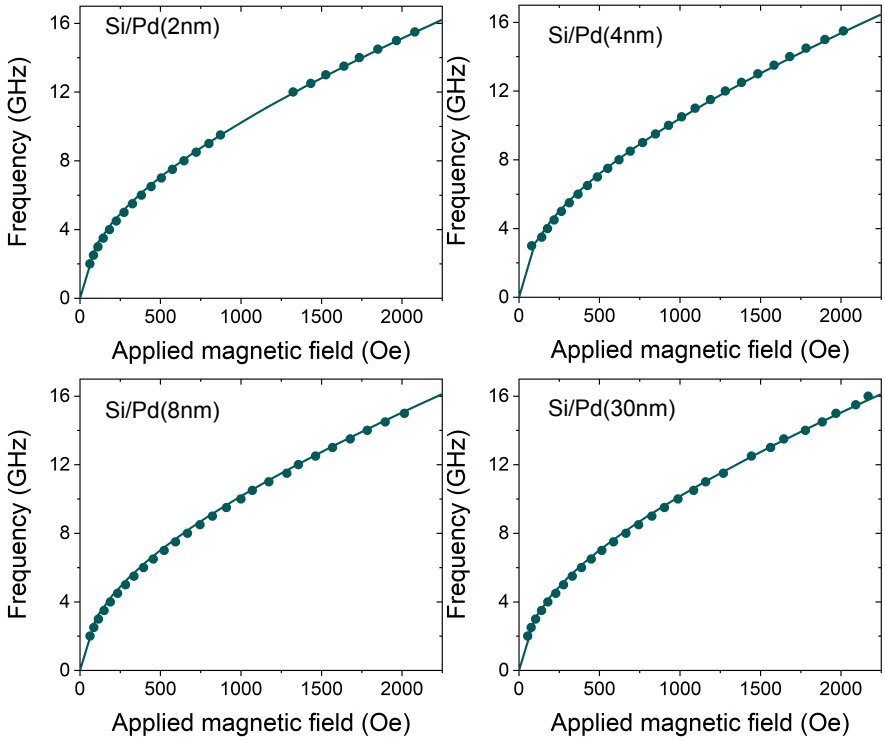

Figure 4.7: Variation of the uniform precession mode frequency as function of an in-plane applied magnetic field for the same bilayers than in figure 4.6. The symbols refer to experimental data while the solid lines are fits to the experimental using equation 4.7.

direction giving the minimal ΔH^{pp} are illustrated in figure 4.7, where the continuous lines are fits to the experimental data. These dependencies have been fitted using the following relation of the uniform precession mode for an in-plane applied magnetic field with the presence of a uniaxial anisotropy field H_u[23]:

$$f_{\parallel} = \left(\frac{\gamma}{2\pi}\right)\sqrt{\left(H\cos\left(\varphi-\varphi_H\right)+H_u\right)\left(H+4\pi M_{eff}+H_u\right)} \tag{4.7}$$

Finally, from these frequency dependencies, we have extracted the ΔH^{pp} variation as function of the frequency. The results are presented in figure 4.8-a) for the thinner and thicker thickness of Pd (2 nm and 30 nm) in both substrates. It is worth mentioning that, for clarity, we have extracted the frequency independent extrinsic residual linewidth (ΔH_0^{pp}) contribution that is represented as an insert in figure 4.8-a). This value varies from a few Oe to several tens of Oe, especially for samples in Kapton substrate. This is most probably due to the higher roughness at the Kapton®/magnetic interface. In figure 4.8-a), the observed linear behavior confirms the main intrinsic contribution to damping. Indeed, some of extrinsic contributions are also frequency dependent such as the two magnons scattering contributions that leads to non linear behavior in the

ΔH^{pp} variation as function of the frequency. As a result, to extract the Gilbert damping constant α, we suppose that ΔH^{pp} presented in figure 4.8-a) is solely due to Gilbert damping and can be written as[129]:

$$\Delta H^{pp}(f) = \frac{2}{\sqrt{3}} \frac{2\pi}{\gamma} \alpha f \tag{4.8}$$

In addition to a higher mean value of ΔH_0^{pp} for Kapton® systems, the difference between the quasi-absence of a Pd (2 nm) and a thick layer of Pd (30 nm) is not as obvious as with Si systems. Indeed, the slope of $\Delta H^{pp}(f)$ is almost divided by two for Si systems (see figure 4.8-a)) while it is almost constant for Kapton ones. Finally, by using equation 4.8, we have deduced the variations of α as function of t_{Pd}. These latters are represented in figure 4.8-b) for both systems. We have the confirmation that the variation is very weak for Kapton® while it is more clear in the case of Si systems. However, for a thickness of 30 nm, the values of both systems seem to converge. This reveals that the Gilbert damping constant increases linearly with $1/t_{\mathrm{Pd}}$ due to the spin accumulation current induced in Pd by the FMR precession of the magnetization and thus a decrease of the angular momentum. The amount of spin pumping is closely related to the spin orbit coupling through the spin flip relaxation time and the interface quality ($g_{eff}^{\uparrow\downarrow}$), which we aim to determine. Finally, we have used equation 4.5 to fit the data; the continuous lines in figure 4.8-b) correspond to the best fit to experimental data. The deduced values for ℓ_{SD} and $g_{eff}^{\uparrow\downarrow}$ are as follow: $\ell_{SD} \simeq 1.11$ nm (respectively $\ell_{SD} \simeq 5.22$ nm) for Kapton® (respectively Si) system and $g_{eff}^{\uparrow\downarrow} = 6.55$ nm^{-2} (respectively 5.9 nm^{-2}).

4.2.3 Magnetostriction coefficient determination

Initially, we wanted to study the effect of an applied elastic strain on the spin-orbit coupling and *in fine* on the spin pumping efficiency of this system. The obtained results are not conclusive and we did not observe any significant evolution of the FMR linewidths as a function of the applied elastic strains. In what follows, we present a methodology which was developed during M. Gueye's thesis and which finally allows to determine the magnetostriction coefficient of thin ferromagnetic films deposited on polymer substrates[149]. Indeed, the determination of the magnetostriction coefficient is also an important parameter if we want to quantitatively analyze the results obtained in arrays of nanostructures. The determination of the magnetostriction coefficient was carried out by making the assumption of elastic and magnetoelastic isotropy (which is justified in all the samples presented in this manuscript). To do this, we glued the film/substrate system onto a PZT actuator[149, 99]. The idea is to record resonance spectra at different strain states by imposing a voltage on the piezoelectric actuator. The transmission of planar deformations from the actuator to the thin film is measured by digital image correlation; for thin films 100% of the in-plane strains are transferred. The different stress states have been obtained by applying a voltage from 0 V to 100 V in steps of 10 V[99, 25].

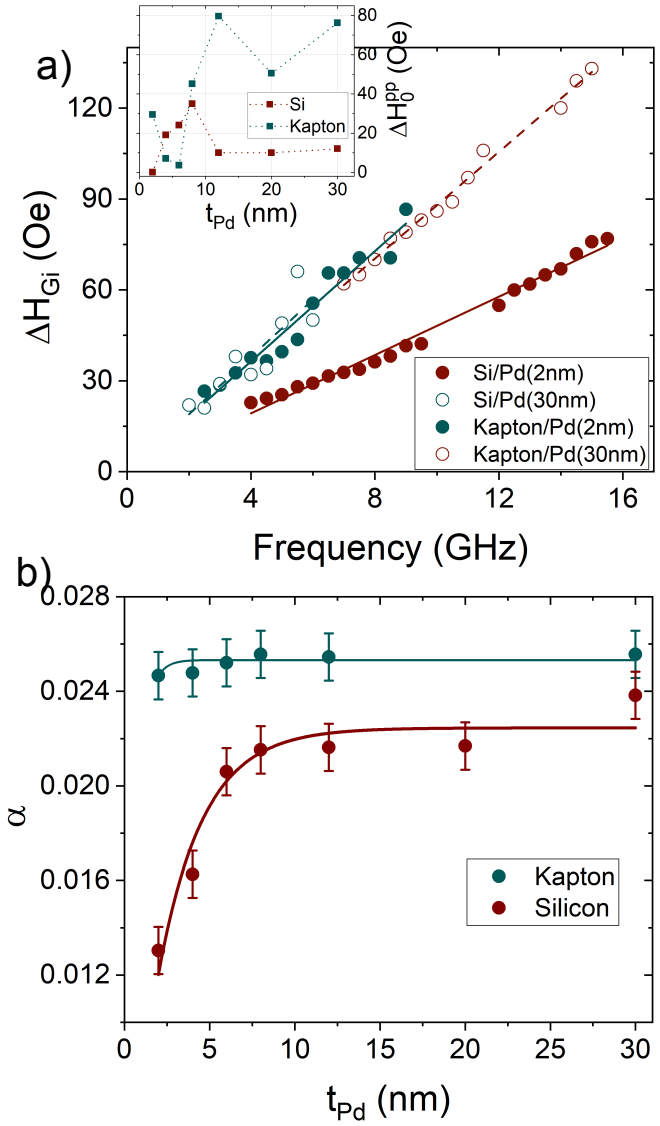

Figure 4.8: a) Peak to peak FMR linewidth variation as function of the frequency of the CoFeB/Pd bilayer systems with a the thinner and thicker Pd thickness (2 and 30 nm, respectively) for both substrate, red symbols are experimental data from the Si substrate while green symbols are data from the Kapton substrate. The open symbols correspond to $t_{\mathrm{Pd}} = 30$ nm while the filled ones correspond to $t_{\mathrm{Pd}} = 2$ nm. The magnetic field is applied in the direction where ΔH^{pp} is minimal (see figure 4.6). The solid lines correspond to linear fits. The ΔH_0 contribution to the linewidth were systematically substracted for a more easier comparison, this contribution is represented in the insert of this graph for all thickness where the variation of ΔH_0 as function of t_{Pd} is plotted for both substrates (the dashed lines are guide for the eyes). b) Variation of the Gilbert damping as function of t_{Pd} deduced from a) using equation 4.8. Symbols refer (red for Silicon substrate and green for Kapton one) to experimental data while solid lines are fits using equation 4.5.

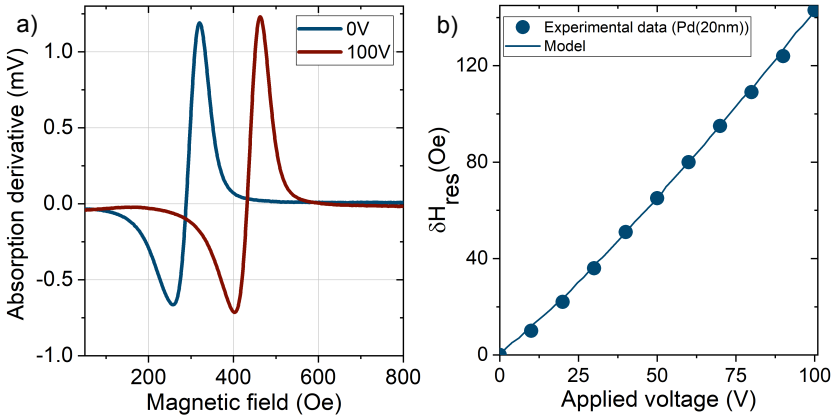

Figure 4.9: a) Typical FMR spectra of the CoFeB(6nm)/Pd(20nm)/PZT-actuator system showing an energy shift when a voltage is applied to the piezoelectric actuator. b) Resonance field shift (δH_{res}) as a function of the applied voltage for the same system. The solid line corresponds to the adjustment obtained using equation 4.9 with $\lambda = 17.5 \times 10^{-6}$.

Figure 4.9-a) shows two typical spectra of the CoFeB(6nm)/Pd(20nm) system in absence of voltage (0 V) and in presence of an applied voltage (100 V) recorded under similar conditions: driving frequency of 6 GHz and the magnetic field applied along the main axis of the PZT actuator. A clear energy shift is observed when a voltage is applied. We then define this resonance field shift as $\delta H_{res} = H_{res}(V) - H_{res}(0)$. This shift is negative for all the thin films studied and already constitutes a first result. Indeed, we can deduce from this that the magnetostriction coefficient λ is positive. As a matter of fact, the magnetoelastic energy for a thin film subjected to a uniaxial stress σ_{xx} (even if it is slightly biaxial here) can be written: $F_{me} = -\frac{3}{2}\lambda(\alpha_x^2 - \frac{1}{3})\sigma_{xx}$[16, 25] where α_x is the magnetization direction cosine. Thus, a magnetoelastic field $\vec{H}_{me} = -\vec{\nabla}_{\vec{M}} F_{me}$ can be introduced. For positive λ and σ_{xx} values, this field is aligned along the main axis (x) of the PZT actuator. This induces an easy axis for the magnetization along x. This ultimately induces a decrease of H_{res} when the field is applied along x ($\varphi_H = 0$) and an increase in H_{res} when the field is applied along y ($\varphi_H = \pi/2$) as experimentally observed. The quantitative determination of λ is possible by fitting the evolution of δH_{res} as function of the applied voltage. This evolution is shown in figure 4.9-b) for the CoFeB(6nm)/Pd(20nm) system. The adjustment of this (continuous line) was possible by introducing the full form of the energy in the formulation of Smith and Beljers ($F_{me} = \frac{3}{2}\lambda\left((\alpha_x^2 - \frac{1}{3})\sigma_{xx}(V) + (\alpha_y^2 - \frac{1}{3})\sigma_{yy}(V)\right)$ and using the isotropic Hooke's law to connect the components of the stress tensor $(\sigma_{xx}(V), \sigma_{yy}(V))$ to the the strain tensor components of $(\varepsilon_{xx}(V), \varepsilon_{yy}(V))$. The values of the Young's modulus and the Poisson's ratio are 160 GPa and 0.3, respectively. Under these conditions, the resonance field is given by the expression[16, 25]:

$$H_{res} = \sqrt{(2\pi M_S)^2 + \left(\frac{2\pi f}{\gamma}\right)^2 + H_1 H_2} - 2\pi M_S - \frac{3\lambda}{M_S}(\sigma_{xx} - \sigma_{yy}) \qquad (4.9)$$

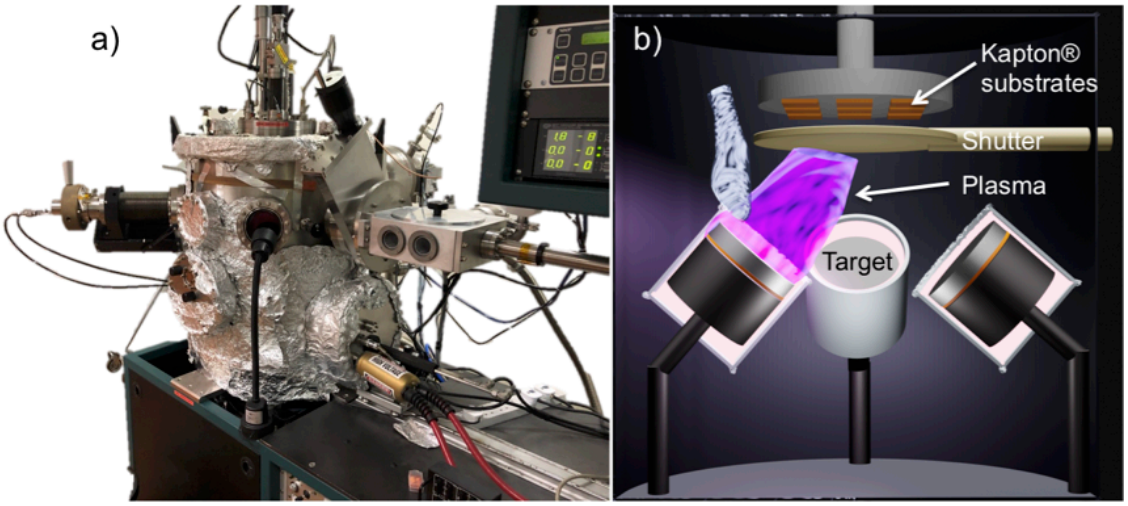

Figure 4.10: a) Photo of the multi-target apparatus from AJA International (NUS Singapore, Pr. Adeyeye's group). b) Sketch showing the interior of the deposition chamber with 3 targets (instead of 6 targets).

where $H_1 = \frac{3\lambda}{M_S}\left(\sigma_{xx}\sin^2\varphi - \sigma_{yy}\cos^2\varphi\right)$ and $H_2 = 4\pi M_S + \frac{3\lambda}{M_S}\left(\sigma_{xx}\sin^2\varphi - \sigma_{yy}\cos^2\varphi\right)$. In addition, φ is the angle between the main axis of the PZT actuator and the magnetic field (here $\varphi = \pi/2$). In this expression, the only unknown parameter is the magnetostriction coefficient λ which can be determined by fitting the experimental data to this model. We found a value of $\lambda = 17.5 \times 10^{-6}$.

4.3 Nanofabrication techniques

In this section, we briefly describe the different nanofabrication techniques that have been implemented to obtain the arrays of magnetic nanostructures studied during this thesis. Two complementary technique have been employed: the interference lithography (IL) and the nano-stencil lithography (SL). Before presenting those nanofabrication techniques, we present in a concise way the deposition of ferromagnetic thin films on polymer substrate. Indeed, for each nanostructure arrays, a thin film of the same thickness was also deposited and which will serve as a reference during the various analyzes.

4.3.1 Elaboration of thin films on polymer substrates

The deposition of our thin films were made using a multi-target apparatus from AJA International (see figure 4.10-a)). The deposition chamber (50 liters) contains 6 target holders which each have their own shutter. This allows a better control when multilayer systems are fabricated. The substrate is placed on a support fixed by a rotating shaft, this allows better control of deposits in the development of multilayer systems. The substrate is placed on a support fixed by a rotating shaft, this allows for multi-target deposition uniform in chemical composition along the thickness, and those by adjusting

the rotation speed of the substrate. A sketch showing 3 targets is represented in figure 4.10-b)[150, 151].
The thin films were deposited on 125 μm thick Kapton® substrates. Before placing the substrates inside the chamber, it is necessary to clean them. Indeed, the Kapton® sheets have been handled during cutting and given their electrostatic properties, they tend to capture impurities. In order to avoid any contamination, these substrates were cleaned in a clean room. They were immersed in Isopropanol in a beaker and placed in an ultrasonic bath for 10 minutes. Following this, they were cleaned using distilled water and a nitrogen gun, before being stored in a clean plastic case. The deposition were made under vacuum (residual pressure of 2×10^{-8} Torr), at an argon pressure of 1mTorr. Furthermore, the substrates were once again cleaned using a plasma (plasma etching) ($Ar+O_2$) at 3 mTorr for 120 seconds just before the deposition. This in order to eliminate any organic residues and improve the adhesion of the films to the substrate[152].

4.3.2 Interference lithography

Interference lithography is a mask-less nanofabrication technique, which has been used widely to synthesize large area magnetic nanostructures. The basic principle of IL involves the use of interference patterns generated from two obliquely incident beam paths (i.e. direct and reflected beams) to expose a photoresist layer. The patterned area and resolution are related to the beam source diameter and wavelength respectively[153, 154]. The IL method allows multiple exposure steps to form a specific pattern on a resist. For example, in order to fabricate dot (or antidot) arrays, a second exposure after rotating the substrate through 90° is needed[154].

A schematic showing the principle of interference lithography is presented in figure 4.11-a). To generate interference fringes on the surface of the photosensitive resin, the substrate is placed on an arm of a Lloyd's mirror interferometer. The second arm of the interferometer contains a square aluminum mirror. The two arms of the interferometer are exposed to a continuous 325 nm beam generated by a Helium-Cadmium (He-Cd) laser ($\Lambda = 325$ nm). The laser beam is focused through a lens into a 10 μm diameter hole which helps eliminate noise and provides a Gaussian profile to the beam. After passing through this spatial filter, the beam propagates towards the sample. The light from the source beam interferes with the light reflected from the mirror to form a standing wave pattern with alternating maxima and minima of intensities. The periodicity of this alternation is equal to[155, 156, 157]:

$$p = \frac{\Lambda}{2 \sin \theta}$$

It is proportional to the half-wavelength of the laser ($\Lambda/2$) and is inversely proportional to the sine of the relative angle θ of the two beams[155]. Figure 4.11-b) displays a typical atomic force microscopy (AFM) image of the top surface of an array of $Ni_{80}Fe_{20}$ on a Kapton® substrate fabricated using the IL process. A profile showing the periodicity of the array is presented in figure 4.11-c). The obtained periodicity is around 600 nm

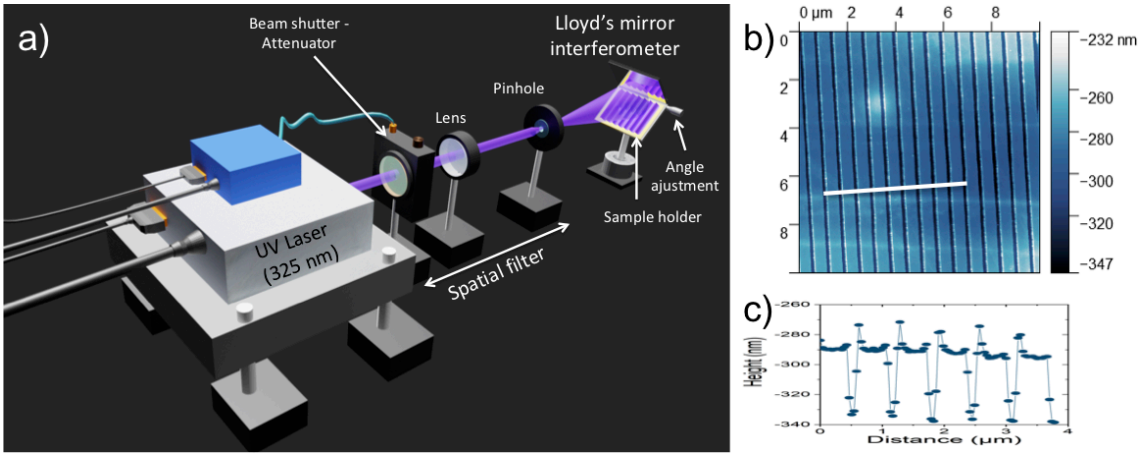

Figure 4.11: a) Schematic of the laser interference lithography setup showing an UV Laser, a beam shutter, a convergent lens (LS), a pinhole (PH) and the Lloyd's mirror interferometer. b) AFM image of an array of $Ni_{80}Fe_{20}$ nanowires (rectangular cross section) fabricated using the IL process. The periodicity is around 600 nm with a nanowire width of about 400 nm. c) Profile (height as a function of the distance) corresponding to the white line in image b) highlighting a thickness of around 40 nm for this array of nanowires.

(nanowire width: 400 nm with an interspacing of 200 nm). To obtain this array of nanowires, a 127.5 µm thick Kapton® layer was first spin coated with an Ultra-i 123 I-Line positive photoresist and then mounted on one arm of a Lloyd's-mirror Interferometer. The interference between the light from the source beam and the light reflected from the mirror form a standing wave pattern with alternating maxima and minima of intensity. After exposition, the photoresist was developed in CD-26 from MicroChem company for 45 seconds, then rinsed in DI water and dried using a nitrogen gun. In this condition, a nanowire pattern is obtained on top of the Kapton® layer. Then, a 20 nm $Ni_{80}Fe_{20}$ film was deposited using the RF sputtering at a fixed Ar pressure of 3 mTorr. Lift-off of the deposited film was carried out in isopropyl alcohol (IPA). Completion of the lift-off process was determined by the color contrast of the patterned $Ni_{80}Fe_{20}$ area[99].

4.3.3 Nanostencil lithography

Nano-stencil lithography (SL) is a high-resolution shadow-mask nanofabrication technique used for patterning surfaces at the micro and nanometer scales[158, 159, 160]. It is a one-step technique that eliminates resist-related processing steps, which is common in a standard lithographic process. Actually, it is exactly the same principle used in prehistoric frescoes on which handprint paintings have been found. Indeed, a stencil (membrane with apertures) is placed (aligned if necessary) and clamped to a substrate. The clamped

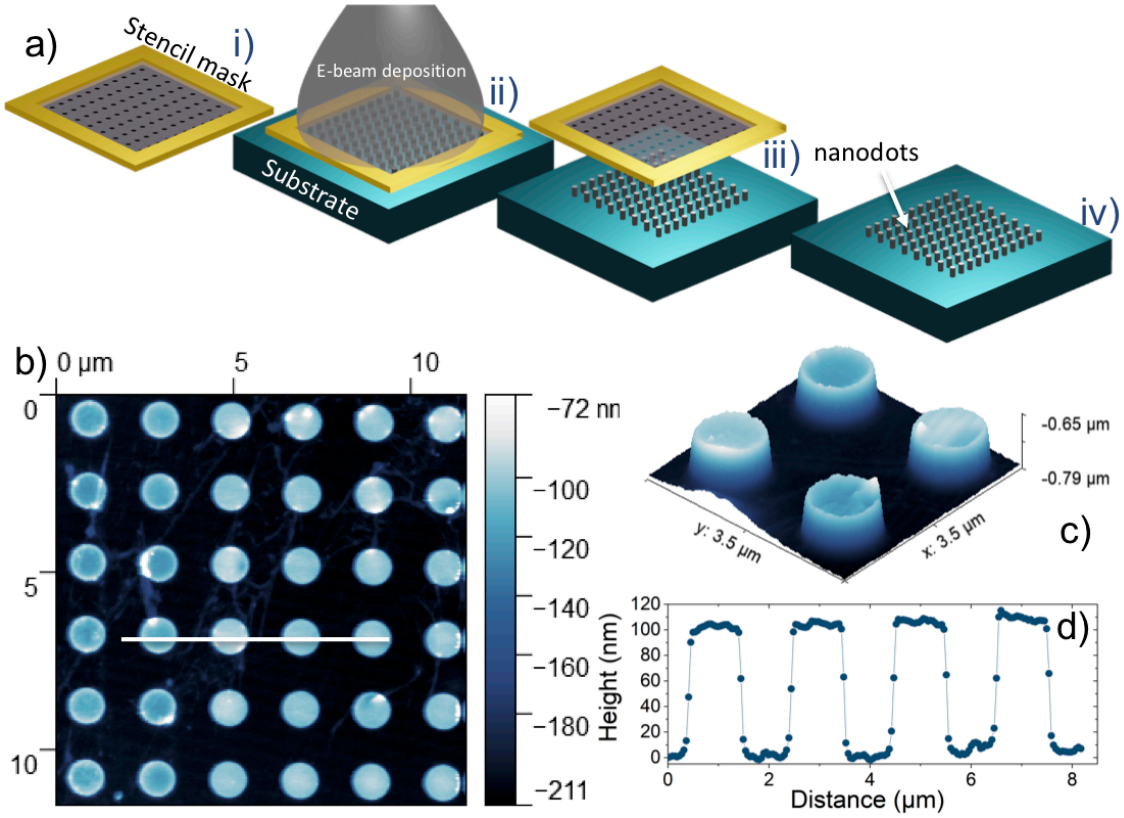

Figure 4.12: a) Schematics of the stencil lithography process: i) sketch of a patterned membrane for stencil. For the sake of clarity, the pattern dimensions are exaggerated. The stencil mask consists of a rigid part supporting a SiN membrane on which the desired pattern is etched. ii) E-beam deposition though the stencil mask. iii) The stencil mask is then removed. iv) An array of antidots is obtained. b) AFM image of a square array of $Ni_{80}Fe_{20}$ circular dots fabricated using the nanos-stencil process. The periodicity is around 2 μm with a dot diameter of about 1 μm. c) 3D AFM image of four $Ni_{80}Fe_{20}$ dots. d) Profile corresponding to the white line in image a) highlighting a thickness of 100 nm for this array of dots.

set is placed in a deposition chamber where materials are evaporated through the stencil's apertures onto the substrate as illustrated in figure 4.12-a). SL is a very promising approach for synthesizing high quality magnetic nanostructures without using solvent and etching thus reducing contamination sources. It is particularly useful for fabricating complex and multilayer nanostructures at elevated temperature because no resist is involved.
Figure 4.12-b) presents an AFM image of an array of $Ni_{80}Fe_{20}$ circular dots obtained thanks to the nano-stencil process. It corresponds to a square array with a periodicity of 2 μm; the diameter of the dots is around 1 μm. Figure 4.12-d) corresponds to a profile obtained from this image (white line in figure 4.12-b)) highlighting the periodicity and the thickness (100 nm) of this specific array. To conclude, figure 4.12-c) presents a 3D AFM image of four $Ni_{80}Fe_{20}$ dots.

5 1D arrays of ferromagnetic nanowires submitted to almost homogeneous strain

Contents

Strain heterogeneities in nanostructure/polymer substrate systems due to the lateral patterning [161, 162, 163] can strongly influence the whole static and dynamic magnetic response. Surprisingly, the quantization of these effects is still poorly reported in the literature and must be studied in depth.
In this context, we have carried out experiments describing the evolution of the magnetic response by ferromagnetic resonance (FMR) during controlled *in situ* straining of magnetic nanostructures deposited on Kapton® substrate. Therefore, large arrays of $Ni_{60}Fe_{40}$ nanowires have been fabricated by interference lithography (IL) [164](see chapter 2) and their behavior has been compared to continuous films of the same thickness (20 nm). The micromechanical tests have been performed thanks to piezoelectric actuators, allowing a good knowledge of the macroscopic strains applied to the Kapton® substrate, which have been measured by digital image correlation (DIC) . Moreover, numerical simulations based on finite elements method (FEM) have been carried out to explain the discrepancies observed between the different systems. Especially, we have considered the transferred strain rate from substrate to magnetic nanostructures, numerically calculated, to adjust the magnetostatic model to the experimental data.

5.1 Magnetization dynamics in absence of applied strain

An in-plane angular dependence measurement of the resonance field was performed on the nanowire arrays. Figure 5.1 shows the obtained results with the corresponding mod-

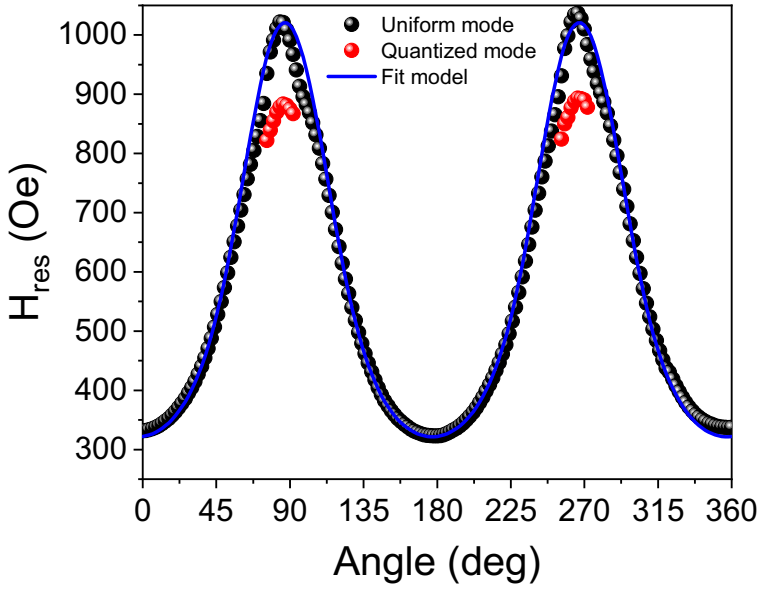

Figure 5.1: Nanowire arrays $Ni_{60}Fe_{40}$ angular dependence of the measured resonance field at 8 GHz. The perpendicular configuration in which the applied field is along the nanowires width corresponds to 90 and 270 degrees.

elization of the magnetic resonance field. The initial orientation in the present case correspond to a magnetic fiel applied in the parallel direction of the nanowires and the a radiofrequency excitation in the transversal direction. One can see a splitting point when the applied field is perpendicular to the principal axis of the nanowires[164, 165]. This spiting is extended over 6 or 7 degrees besides of the perpendicular configuration and consist of the appearance of a quantified mode[164, 166, 167].

As described in the second chapter, micromagnetic simulations were performed using OOMMF software. The methodology used is always the same, the equilibrium situation is first calculated and used as the starting point for the dynamical response. A 2400 $\times$2400 $\times$20 nm^3 patterned area of four nanowires was created using the OOMMF mesher. A size of meshing cuboid element of 10 nm^3 has been chosen during the simulation for both the static and dynamic studies. The two situations, perpendicular and parallel configurations, have been simulated. Figure 5.2 shows some of the calculated spectra obtained in the case of a steady field applied in the perpendicular direction of the nanowires (transversal direction to the length of the nanowires).

The simulations are compared to the experimental results obtained in the parallel and perpendicular configurations in FMR. As one can see in figure 5.3, our simulations are in a good agreement with the experimental results for both the principal modes (red and black scatters) and the first quantified mode (white scatters). There is also a frequency softening of the principal mode and the quantified one near 400 Oe in the experimental

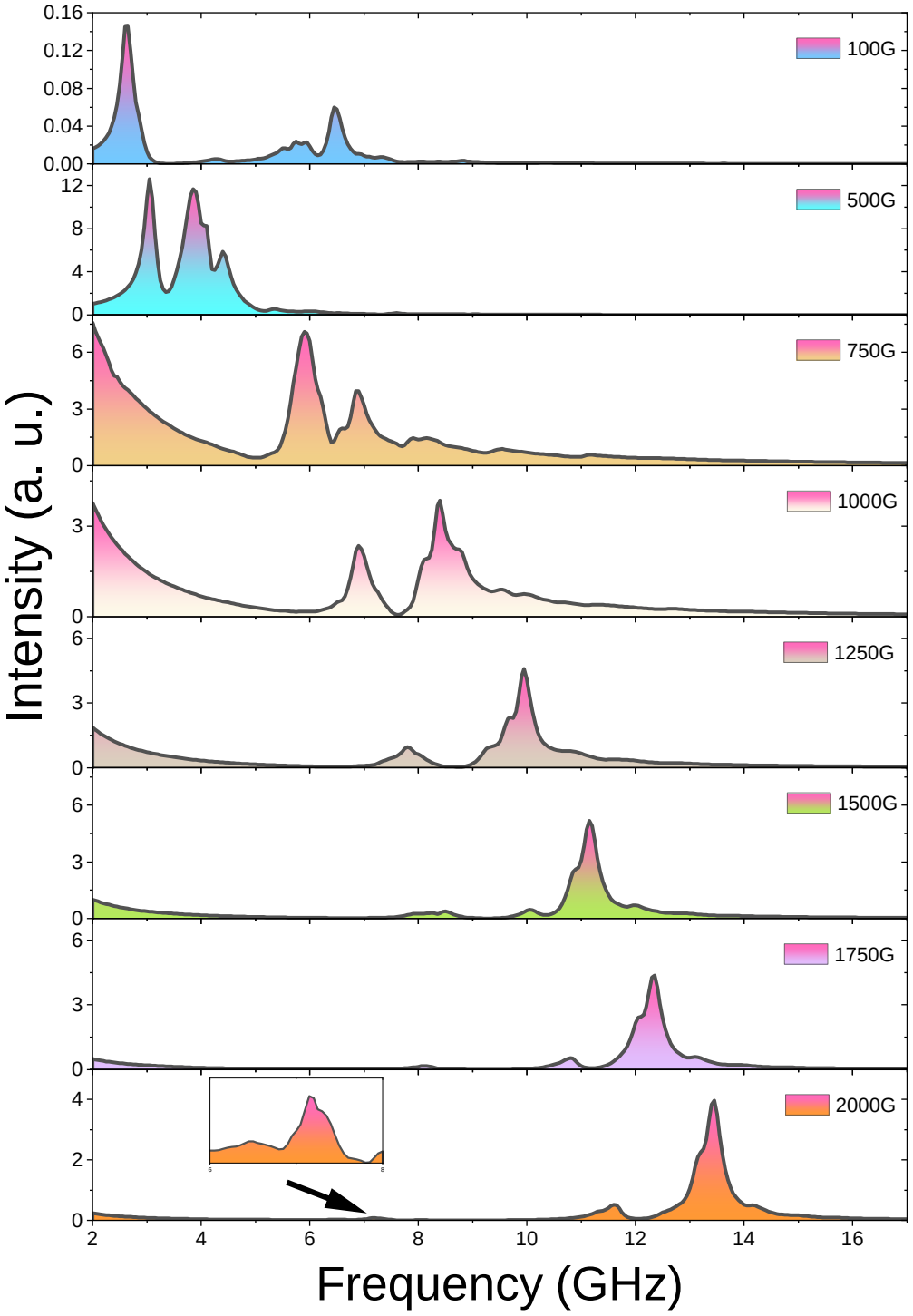

Figure 5.2: Fast Fourier transform spectra of the $Ni_{60}Fe_{40}$ nanowire arrays in tranversal configuration. The steady in-plane magnetic field, swept from 100 G to 2000 G by 50 G step, is applied perpendicularly to the length of the nanowires.

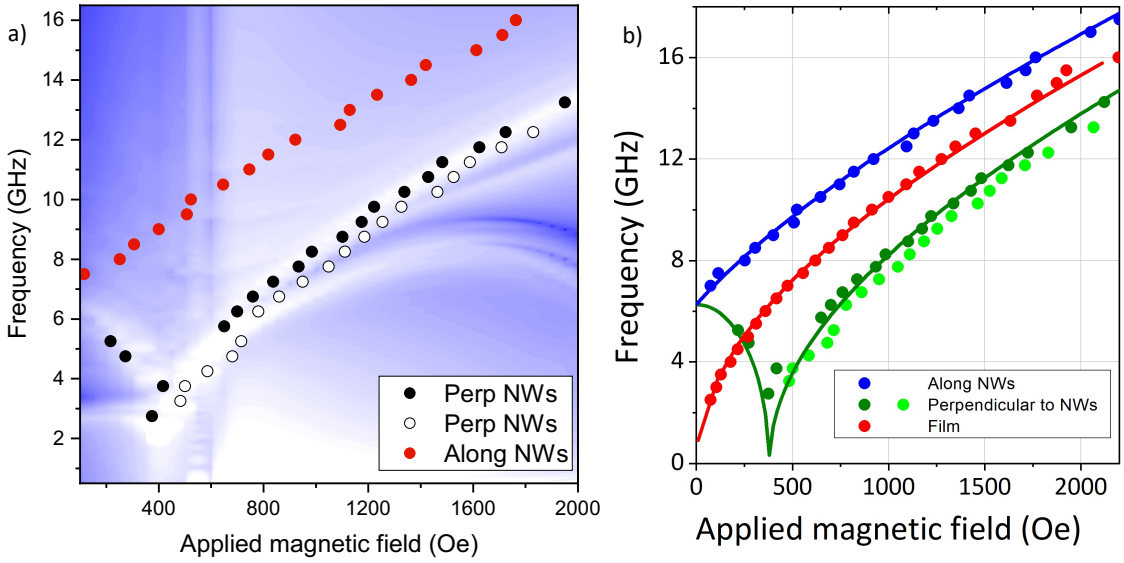

Figure 5.3: a)Mapping of the simulated frequency dependence in the perpendicular configuration and the experimental measurements corresponding to the two configurations, perpendicular and parallel to the nanowires length. For the sake of clarity, simulations in the parallal configuration is not shown here. b) The corresponding frequency dependance represented in dots. The continuous lines correspond to the fitting.

results which was also predicted by the simulations[168]. However, the third mode and its softening (among 2000 Oe) are not visible in the experiment despite its good visibility on the numerical results. This invisibility can be explained in two different way, the first supposition is that the spatial extension of the concerned mode, which is localized in the corner sides of the transversal nanowire section, is very small and this give rise to small intensity peak in FMR spectra. The second supposition, is the most plausible explanation, is that the nanowire section is not rectangular but it is more rounded corner section or rough edges [169, 170, 171].

5.2 In situ FMR measurements

A 3D schematic of the formed heterostructure is presented in figure 5.4-a). Two different systems have been studied. In the first one, the nanowires axis is aligned along the principal axis of the actuator (x direction, see sketch in figure 5.5-b)), this system is defined as "Parallel Nanowires" thereafter. The second one is defined as "Perpendicular Nanowires" with the nanowires axis aligned along y direction (see sketch in figure 5.5-c)). During the experiments, the static magnetic field was applied along the piezoelectric

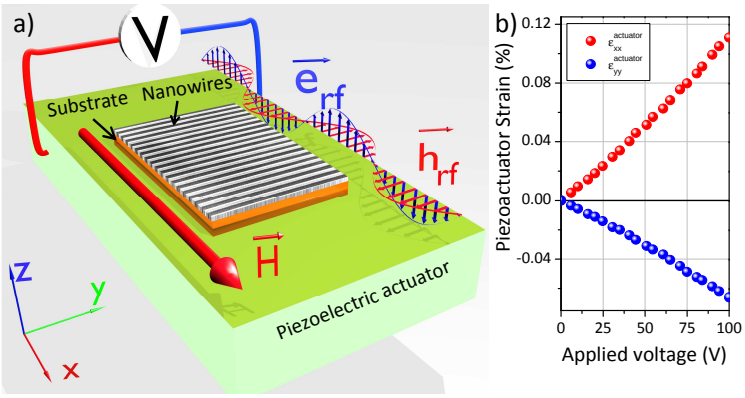

Figure 5.4: a) Schematic of $Ni_{60}Fe_{40}$ nanowires array on a Kapton® substrate, glued on the top of a piezoelectric actuator (green). $\vec{H}$ corresponds to the applied magnetic field while $\vec{h}_{rf}$ and $\vec{e}_{rf}$ are the radio-frequency fields generated by the frequency generator (10 MHz-20 GHz) and the stripline. $\vec{H}$ was applied along the main axis (x) of the piezoelectric actuator and perpendicular to $\vec{h}_{rf}$. b) Mean in-plane strains ($\varepsilon_{xx}^{actuator}$ and $\varepsilon_{yy}^{actuator}$) at the back surface of the actuator as calculated using DIC technique [17]. Red and blue symbols correspond to $\varepsilon_{xx}^{actuator}$ and $\varepsilon_{yy}^{actuator}$, respectively. The applied voltage is ranging from 0V to 100V with increments of ~ 5 V.

actuator. The principle of these *in situ* measurements is to deform the magnetic media through the voltage applied to the actuator, the strains being transmitted from the actuator to the substrate supporting the magnetic media [31].

Figure 5.5 displays typical FMR spectra obtained at 0 V (green spectra) and at 100 V (red spectra) for the three systems under a driving frequency $f = 8$ GHz. A small sketch is added in each graph. For clarity, the spectra have been horizontally shifted by the resonance field in absence of applied voltage. In all cases, we clearly observe a resonance field shift ($\delta H_{res} = H_{res}(0V) - H_{res}$) of the spectra. However, the amplitude of this shift varies from a system to another. It is maximal ($\delta H_{res} \sim 100$ Oe) for the continuous film and minimal for the "Perpendicular Nanowires" system ($\delta H_{res} \sim 50$ Oe). In addition, we note the presence of two modes in figure 5.5-c). This is due to the lateral size reduction that leads to wave-vector quantization (q_n) of the propagating spin wave [166, 167, 88]. Thereafter, these modes will be called $n = 1$ and $n = 2$ modes. These modes are the so-called "bulk modes" and are localized in the entire cross section only excluding the nanowire edges [172, 173]. As in ref. [164], we observe that the mode $n = 1$ is always observable while the mode $n = 2$ is only observable when the applied field is perpendicular to the nanowires. This is the reason why we observe only one mode ($n = 1$) in the spectra of the "Parallel nanowires" system (see figure 5.5-b)). It should be mentioned that if we apply the magnetic field along y direction, we observe the presence

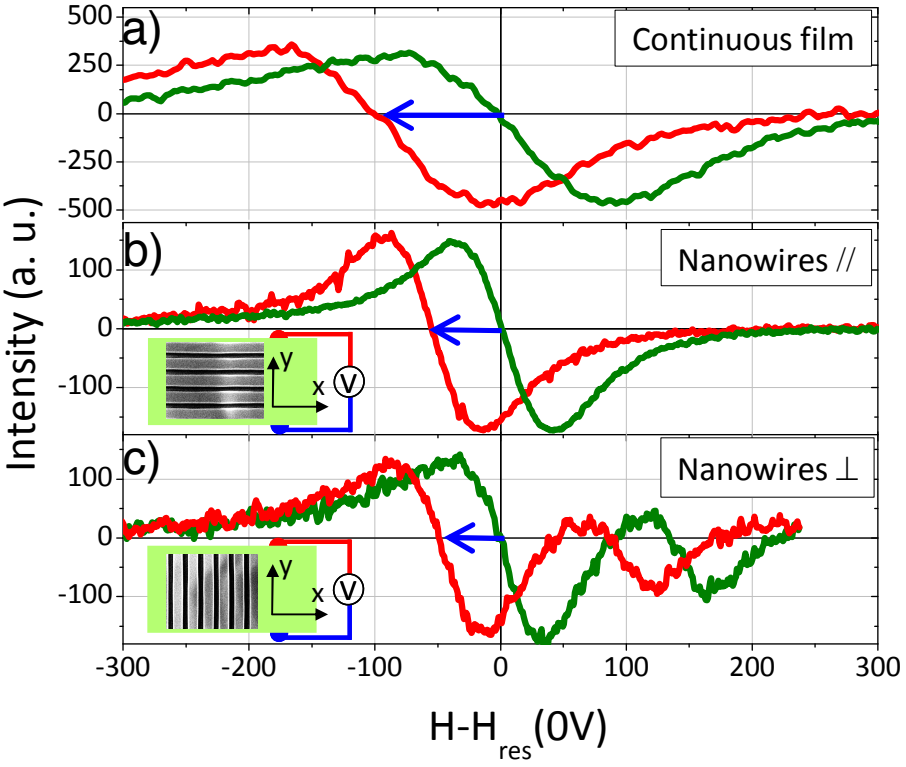

Figure 5.5: a-c) Typical FMR spectra obtained at 0 V (green) and under 100 V (red) for the continuous film (a), the "Parallel Nanowires" (b) and the "Perpendicular Nanowires" (c) systems. Small sketches representing the "Parallel Nanowires" and the "Perpendicular nanowires" systems are drawn.

of the two modes in the "Parallel Nanowires" system and one for the "Perpendicular Nanowires" system (and *vice versa*). Interestingly, the δH_{res} variations corresponding to the two modes are very close one to each other.

Keeping in mind that the resonance field shift principally depends on the magnetostriction coefficients and the saturation magnetization (M_S), we assume here an isotropic magnetostriction coefficient (λ) since the elastic and magnetoelastic properties are considered as isotropic. Indeed, the fabricated films and nanowires have been checked to be isotropic from a microstructural point of view (polycrystalline microstructure with a random orientation of the grains). In these conditions, the magnetoelastic energy can be written as[31]:

$$F_{me} = \frac{3}{2}\lambda\left(\left(\alpha_x^2 - \frac{1}{3}\right)\sigma_{xx}(V) + \left(\alpha_y^2 - \frac{1}{3}\right)\sigma_{yy}(V)\right) \tag{5.1}$$

$\sigma_{xx}(V)$ and $\sigma_{yy}(V)$ being the in-plane principal stress tensor component in the magnetic medium while α_x and α_y are the direction cosines of the magnetization. The relations between the stress components ($\sigma_{xx}(V)$, $\sigma_{yy}(V)$) and the strains ($\varepsilon_{xx}(V)$, $\varepsilon_{yy}(V)$) of the magnetic medium are given by the (isotropic) Hooke's law with the Young's modulus and the Poisson ratio of the magnetic phase equal to $Y_f = 205$ GPa and $\nu_f = 0.3$, respectively. These parameters have been calculated by homogenization method [174] from the bulk elastic coefficients of $Ni_{60}Fe_{40}$ material taken from ref. [175]. Finally, the relation between strains and voltage is given by data on figure 5.4-b). In these conditions, the resonance field for a magnetic field applied along $x-$axis is given by [16, 176, 149, 177]:

$$H_{res} = \sqrt{\left(2\pi M_S + \frac{3\lambda}{M_S}\sigma_{yy}\right)^2 + \left(\frac{2\pi f}{\gamma}\right)^2} - 2\pi M_s - \frac{3\lambda}{M_s}\left(2\sigma_{xx} - \sigma_{yy}\right) \tag{5.2}$$

Where γ is the gyromagnetic factor. We have carried out standardized FMR measurements in absence of applied voltage (not shown here) on the "Continuous Film" system to determine $M_S = 950$ emu.cm^{-3}and $\gamma = 1.822 \times 10^7$ Hz.Oe^{-1} values. Moreover, from the δH_{res} variation as a function of the applied voltage, it is possible to quantitatively determine λ [17, 10, 31] in the case of continuous film. Indeed, being given Y_f, ν_f, M_S and γ values, the only fitting parameter is λ. Under these conditions, the red continuous line in figure 5.6 corresponds to a fit (using equation 5.2) of the experimental data for the "Continuous Film" system allowing the determination of $\lambda \simeq 11.5 \times 10^{-6}(0.5 \times 10^{-6})$. More details about magnetostriction coefficient determination can be found in ref. [176, 10].

5.3 Mechanical simulations coupled with magnetic analytical model

In ref. [164], we have verified that M_S is not influenced by the lithography process, one may conclude to similar behavior for λ. Thus, the observed dependence of δH_{res} to the system should be imputed to another physical process. We think it is due to a lower transmission of the in-plane strains from the polymer substrate to the magnetic media in the case of nanowires systems. To confirm this assumption, we conducted numerical simulations with COMSOL Multiphysics® software (Structural Mechanics Module). Figure 5.7-a) gives a sketch of the simulation main idea and findings. Due to limited RAM memory and based on mechanical observations, the substrate has been satisfactory approximate as a cuboid of dimensions ($10 \times 10 \times 10$ µm^3) whereas the simulated arrays of nanowires are thus limited to around 15 nanowires. Moreover, we verified that it is acceptable to consider such limited number of nanowires as there is no evolution of the numerical results after adding supplementary nanowires. Figures 5.7-b-e) show the distribution of the transmitted in-plane strains (ε_{xx} and ε_{yy}) at a given

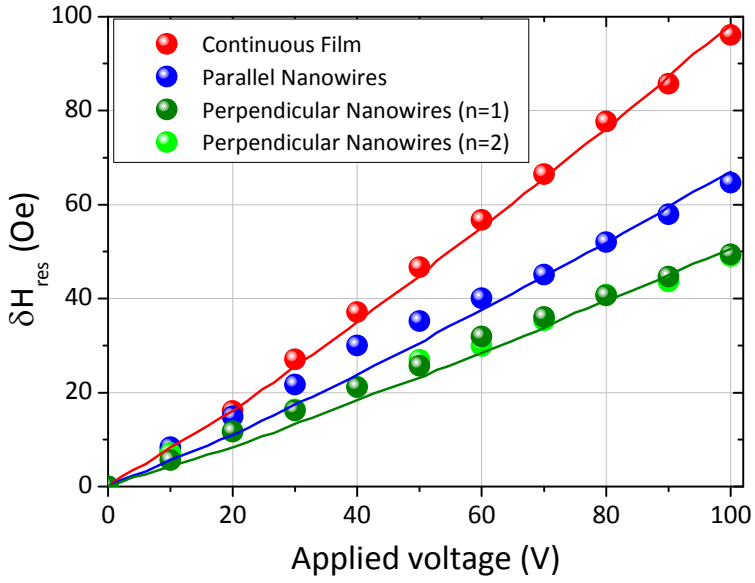

Figure 5.6: Resonance field shift δH_{res} variation as function of the applied voltage for the different systems. Full lines are calculated lines using α_{xx} and α_{yy} determined from COMSOL Multiphysics® simulations (see text).

Sample	α_{xx} (%)	α_{yy} (%)
Continuous film	100.0	100.0
Parallel nanowires	97.8	62.5
Perpendicular nanowires	27.0	97.7

Table 5.1: Strains transmission factors α_{xx} and α_{yy} for the different systems.

deformation state of the substrate; here $\varepsilon_{xx}^{substrate} = 1 \times 10^{-3}$ and $\varepsilon_{yy}^{substrate} = -0.5 \times 10^{-3}$ which correspond to the deformation state at 100 V[177, 178, 17].

The numerical simulations show that the strains in the nanowires and the substrate can be very different in contrary to the continuous film [179]. Two interesting cases can be highlighted: (i) when we probe the strain component tangent to the nanowires, *e.g.* ε_{xx} if the nanowires are aligned according to x (figure 5.7-d)) and ε_{yy} when the nanowires are aligned along y direction (figure 5.7-c)), we find the transmission of the strains is almost perfect (between 97% and 98%), (ii) when we probe the strain component perpendicular to the nanowires, *e.g.* ε_{yy} when the nanowires are aligned according to x direction (figure 5.7-e)) and ε_{xx} if the nanowires are aligned along y (figure 5.7-a)), then the transmission of strains is much worse. However, we can see from figure 5.7-f) that the transmitted in-plane strains are almost homogeneous inside the nanowires. Therefore, whatever the location of the magnetic modes in the nanowires, the strain undergone remains about the

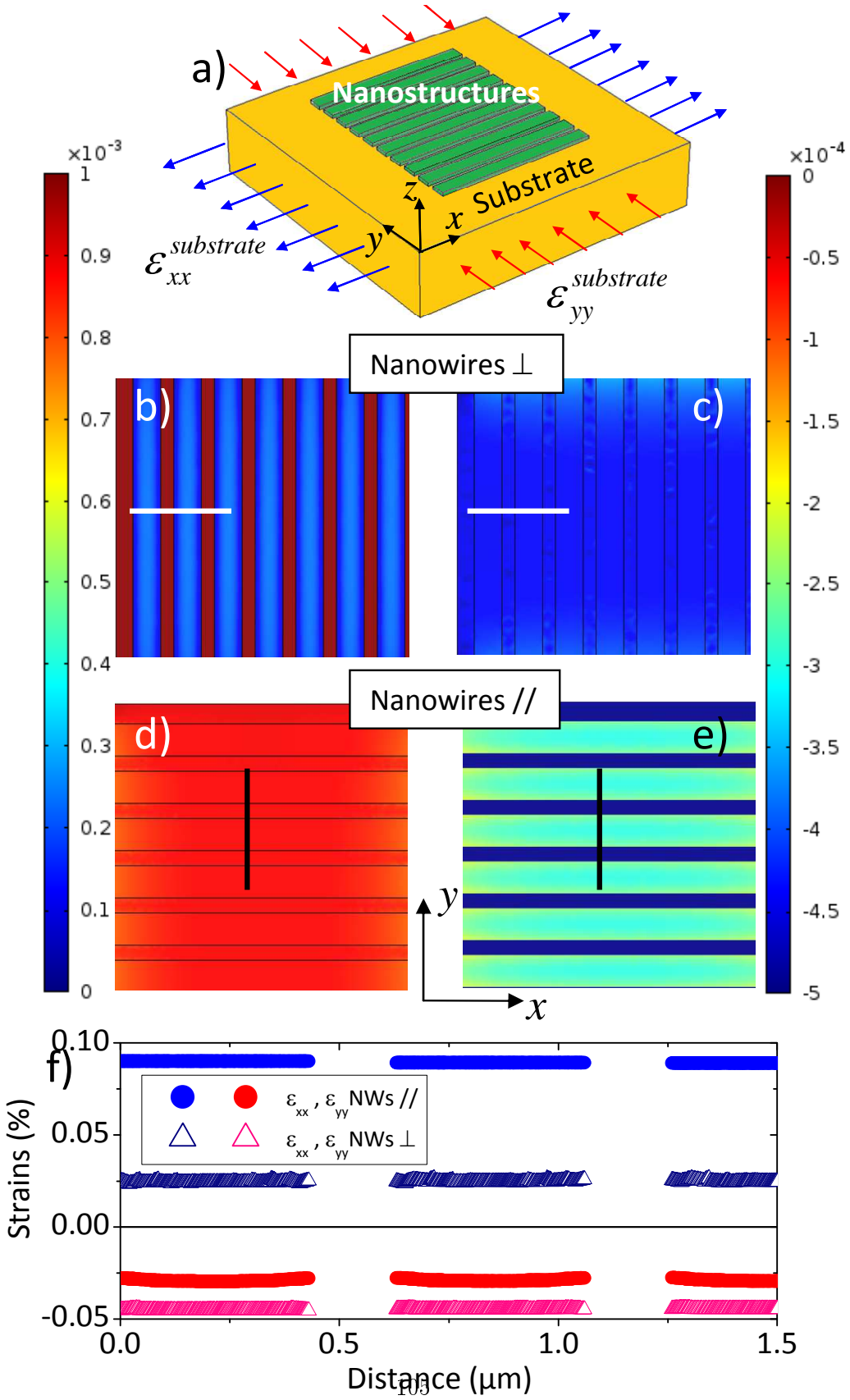

Figure 5.7: a) Sketch of a simulated system. The imposed $\varepsilon_{xx}^{substrate}$ and $\varepsilon_{yy}^{substrate}$ are the ones determined from DIC measurements. b-e) Maps of the calculated in-plane strains (ε_{xx} and ε_{yy}); b) and d) correspond to ε_{xx} maps while c) and e) correspond to ε_{yy} maps. f) Profiles of the calculated in-planes strains extracted from the corresponding lines in graphs b-e). The imposed strains are $\varepsilon_{xx}^{substrate} = 0.1\%$ and $\varepsilon_{yy}^{substrate} = -0.05\%$.

same. In addition, as previously mentioned, the two probed modes here are not "edge" modes but rather "bulk" ones [172, 173].
It is undoubtedly the poor transmission of strain with respect to the components normal to the nanowires which explains the disparities of magnetoelastic behavior between the continuous film and the two geometric configurations of the nanowires. Thus, we can define two factors that express the mechanical transmission rate between the two average values, namely:

$$\alpha_{xx} = \frac{\varepsilon_{xx}}{\varepsilon_{xx}^{substrate}} \text{ and } \alpha_{yy} = \frac{\varepsilon_{yy}}{\varepsilon_{yy}^{substrate}} \tag{5.3}$$

Table 5.1 summarizes the extracted α_{xx} and α_{yy} factors. The use of these factors is meaningful only if the strains can be supposed as homogeneous inside the nanowires, as in the present case. Now, incorporating these factors into the equation governing the resonance field to correct the transmitted strains, $\alpha_{xx}\varepsilon_{xx}^{substrate}(V)$ and $\alpha_{yy}\varepsilon_{yy}^{substrate}(V)$ instead of the previous ones for the arrays of nanowires and M_S, λ, γ, Y_f and ν_f of the film system allow us to obtain fits in figure 5.6-b). One can note the good agreement between the experimental data and the calculations.
The numerical simulations allowed us to interpret the experimental data obtained by ferromagnetic resonance. Thus, the large differences in resonance fields obtained for the continuous thin film and for the nanowires in different geometries are closely related to the effects of discontinuities with respect to the strain components. This purely mechanical effect, from the strong mechanical contrast between $Ni_{60}Fe_{40}$ and Kapton®, could be exploited in other studies. Indeed, one can imagine being able to optimize the distribution of these material discontinuities to control both the desired magnetic properties while minimizing the harmful effects of strains in highly stretchable systems. The methodology used for nanowires can be easily extended to two-dimensional nanostructures for which one can consider small strain transmission in any in-plane (xOy) direction. Indeed, the relevant parameter for a 2D nanostructure adherent to a flexible substrate is the ratio between its thickness (t) and its lateral dimensions (L for a square dot). The higher is this ratio (t/L), the lower are the strain transmission factors (α_{xx} and α_{yy}). To illustrate this purpose, we have calculated the mechanical transmission rates for arrays of square nanostructures (nanodots) with various aspect ratios during a homogeneous uniaxial tensile test with $\varepsilon_{xx}^{substrate} = 0.03\%$. Moreover, to go further in the analysis, we considered two different materials for the substrate, namely Kapton® and PDMS, which are characterized by very different Young's moduli.
Thus, we have performed FEM simulations on a finite array of Ni nanodots (with $L = 200$ nm) fixed at the top surface of a polymer substrate (either PDMS or Kapton®) of thickness of 5μm. It should be noted that the substrate thickness has substantial effect on the strain transmission only if it is of the same order of magnitude than the nanostructure dimension. For simplicity, isotropic mechanical behaviors have been considered for the two chosen substrates and for the nanodots. The Young's modulus of the nanodots is fixed at 200 GPa with a Poisson's ratio of $\nu = 0.3$ while it was fixed at 4 GPa and 7.5×10^{-4} GPa for Kapton® (with $\nu = 0.3$) and PDMS (with $\nu = 0.49$), respectively.

Figure 5.8 displays the strain transmission factors *versus* the nanostructures aspect ratio. In the case of Kapton® substrate, α_{xx} and $\alpha_{yy}$are relatively high for thinner (1 nm) simulated nanostructures ($\alpha_{xx} \sim 0.75$ and $\alpha_{yy} \sim 0.55$) and decrease very sharply when increasing the aspect ratio (t/L). For example, if the aspect ratio $t/L > 5\%$ ($t > 10$ nm in our case), then the strain transmission factors are inferior to 0.1. This means that bidimensionnal nanostructuration on Kapton® substrate can be preserved from strong magnetomechanical effects for relatively moderate thicknesses. Moreover, in the case of PDMS substrate, the strain transmission factors are almost zero already from the lower values of the aspect ratio (t/L). This is explained by the PDMS Young's modulus relatively low value. All these effects are explicitly illustrated by 3D maps of ε_{xx} in the whole simulated material system (see figure 5.8, note that only the top surface of the substrate is shown). We can clearly see from this figure the effects, on the strain distribution in the nanodots and their very close neighborhood in the substrate, of both the substrate mechanical properties and the aspect ratio . These results are consistent with recent experimental results [180]. Moreover they look similar to other in-plane geometries like cylinders . As a consequence of these simulations, it can be concluded that the 2D nanostructuration stands as a way to avoid eventual undesirable magnetomechanical effects in sheapable magnetoelectronics devices [109], additionally to the one consisting in prestretching an elastomeric substrate such as PDMS[181] .

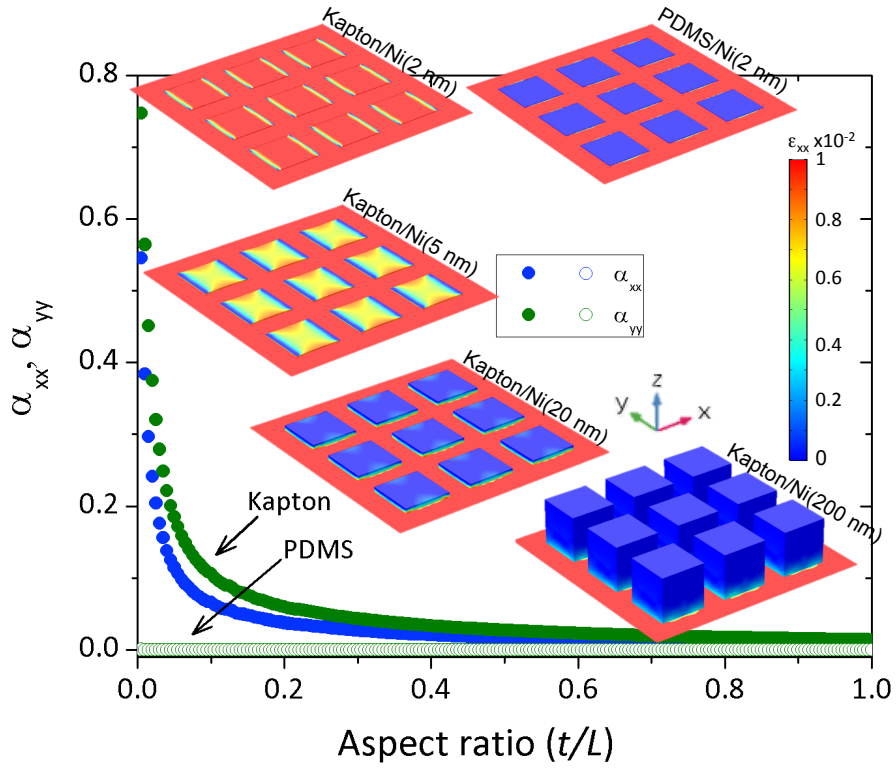

Figure 5.8: Simulation of a finite array of nickel (Ni) nanodots deposited on the top of a polymer substrate (either PDMS or Kapton®). The thickness of the polymer substrate is 3 µm whereas the thickness of the nanodots is varied from 1 to 200 nm (aspect ratio from 0 to 1). Typical 3D maps, where colors encode $x-$component of the strain tensor, are shown. Note that only the top surface of the substrate is shown for clarity. The graph corresponds to the variation of the mean strain transmission factors (α_{xx} and α_{yy}) as function of the nanodots thickness. Open and full symbols correspond to values obtained with PDMS and Kapton®, respectively.

6 2D arrays of ferromagnetic antidots submitted to heterogeneous strain

Contents

One can imagine controlling separately these spatially localized spin wave modes by applying local magnetic fields [182]. While it is not straightforward to control a magnetic field at the scale of mode localization, it is possible to take advantage of the geometrical (and thus mechanical [183]) heterogeneity to obtain a position-dependent magnetoelastic field. To achieve this goal, antidot-type systems are well suited because an external macro-strain will be periodically distributed in a non-homogeneous manner[184], as well as the localization of magnetic modes [185, 186, 187, 188, 189]. This is all the more the case as a supporting layer is compliant since it should accommodate the strain heterogeneities that are known to take place in holed structures [124]. Furthermore, the differentiated sensitivity to the strain field of the magnetic modes may depend on the orientation of the system with respect to the external strain.

we propose a concept using two levels for tailoring individually the magnetic modes, *e.g.* the mechanical contrast between antidots and supporting layer and the geometrical features of the system. This approach is still unexploited in the literature. It has been validated by the study of strain fields and magnetic mode energies in $Ni_{60}Fe_{40}$ antidot arrays. In order to optimize strain heterogeneities, the antidots have been first fabricated on a supporting compliant polyimide layer and then cemented onto a ferroelectric substrate generating macroscopic strain (figure 6.1). The correspondence between the localization of mechanical and magnetic quantities was analyzed by numerical modeling in order to predict the differentiated change in spin wave mode frequencies as a function of the external strain (figures 6.1a-b)). Magnetic antidot arrays present both magnetic heterogeneities (through localized magnetic modes due to in-plane invariance break) and mechanical ones (due to the presence of free surfaces and to the mechanical contrast

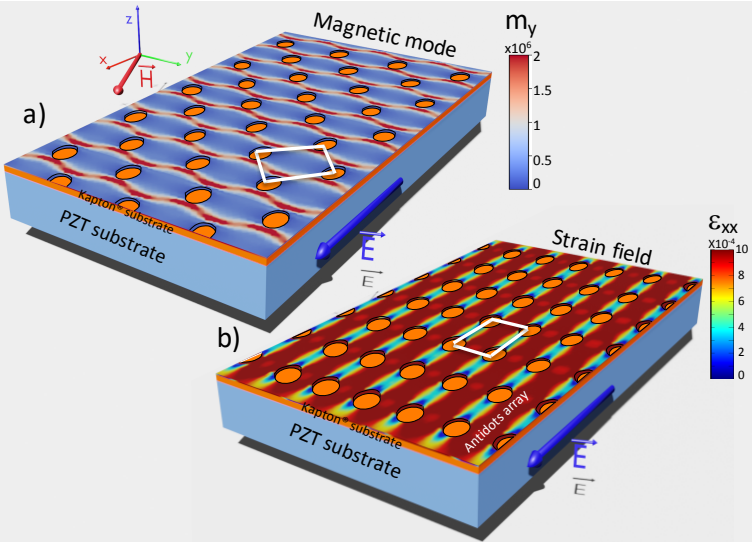

Figure 6.1: Sketch of the two studied systems (magnetic antidots/Kapton®/PZT substrate); the array is either aligned along x-axis of the PZT substrate (Square Array -SA- system) in b) or it makes a 45° angle with respect to the x-axis (Centered Square Array -CSA- system) in a). Illustration of magnetic mode and strain field distributions mapping in a) and b), respectively . The map corresponds to the profile (m_y component) of one of the studied magnetic mode obtained with a static magnetic $\vec{H}$ applied along x in the CSA system in a). A red color in the mapping means a high amplitude spin precession while a blue color means zero amplitude. b) Example showing a mapping of calculated strain field distribution (ε_{xx} component here) in the array of antidots when an electric field is applied to the PZT substrate in the SA system.

between Kapton® and $Ni_{60}Fe_{40}$ material)[184, 190]. We have used double numerical modeling to spatially locate the different magnetic modes with their energies (6.1-a)) and to quantitatively determine the in-plane strain distributions (6.1-b)) in the antidot arrays. Then, the local magneto-mechanical coupling can be estimated using a "classical" magnetoelastic formalism. The magnetic problem was solved by performing 3D micromagnetic simulations thanks to OOMMF package [55] and the mechanical one was solved by using COMSOL Multiphyics® software[92]. The experiments have been performed by *in situ* ferromagnetic resonance (FMR) spectroscopy[191, 16, 26]. Analysis of the data shows that the different magnetic modes can have their frequency modified, the shift being strongly dependent on their localization (difference of several tens of %). Furthermore, the rotation of the system as referred to the external strains (and magnetic field) causes a strong modification of this dependence since it changes the localization of the magnetic modes and the mechanical strains. In the remainder of this paper, we first present the experimental setup used and the methodology adopted to study the phenomena of interest, then the magnetic behavior of the studied system is reported including the numerical comparison. Then, the strain localization in the corresponding structure is studied to finally adjust a magnetoelastic model to reproduce the magnetic behavior of the localized modes.

6.1 Localized magnetic modes in absence of elastic strains

Usual magnetic characterizations were carried out in the present study. Typically the angular resonance field dependence and the frequency resonance dependence. Figure 6.2displays the angular dependence obtained at 8 GHz dynamic field frequency and mostly three intense modes were pointed out. Similar study was carried out on hexagonal antidot arrays with different holes diameters and reported ref.[192] . Two major modes have opposite angular dependencies (black and blue dots) and the third one is almost linear and doesn't show high variation with respect to the applied field direction.

Depending on the angle between the antidots array and the main axis of the ferroelectric substrate, two configurations have been studied. The first one has been obtained by gluing the antidot array along the main axis ($x-$axis) of the ferroelectric substrate while the second one has been obtained by gluing the antidot array at 45° with respect to $x-$axis; a sketch of each configuration is presented in figures 6.1-a) and 6.1-b). Thereafter, the first configuration will be called Square Array (SA) system and the second one will be called Centered Square Array (CSA) system. This two extreme configurations have been defined in order to obtain significantly different strain heterogeneity maps, as described in the following sections. Finally, for comparison, a reference 20 nm thick $Ni_{60}Fe_{40}$ continuous film has been also fabricated and studied.
FMR response of the antidot arrays was measured at room temperature by sweeping the applied magnetic field in the range 0-2500 Oe at different fixed frequencies (from 0.1 to 15 GHz). In figure 6.3-b), a typical FMR spectrum recorded at 8 GHz from the SA

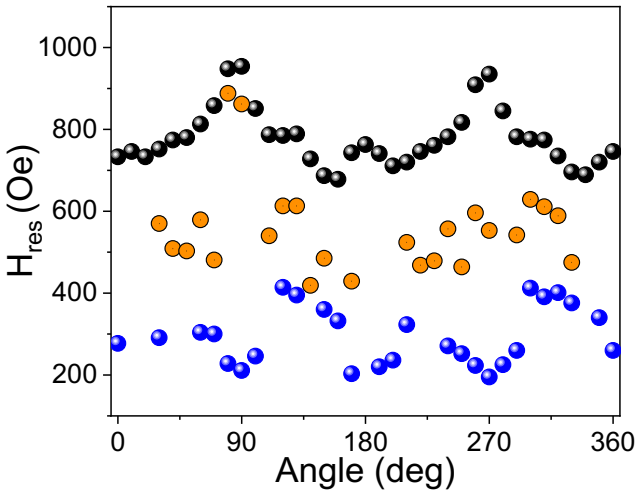

Figure 6.2: Angular resonance field dependence of the studied antidot arrays. Measurement was carried out at 8 GHz excitation field frequency with aimutal angle vaying from 0 to 360 degrees.

system is presented. A multi-modal response (see stars) is clearly observed as compared to the reference continuous film which presents a unique mode (not shown here). In this spectrum, we observe two prominent peaks and two weaker ones (highlighted by a zoom-in). This difference in intensity between peaks suggests that they originate from fundamental resonance of different spatial regions of the antidot system [193, 194, 195, 196, 169]. We have plotted the whole experimental frequency peak positions in figure 6.3-a) that are represented by open symbols. At low frequencies (below 6 GHz), some modes (open black symbols) with very weak intensities are present at high magnetic field that are generally due to a dynamic precession at the edge of the nano-holes [195, 197, 198]. At higher frequencies (above 7 GHz), the two major peaks (blue and red stars in figure 6.3-b)) are easily detectable in almost the entire range of frequencies (7-14 GHz) while the weaker ones were only intermittently detectable, certainly due to their weaker initial intensity. Micromagnetic simulations giving the frequency positions and relative intensities are also presented in figure 6.3-a) using a relative color mapping from 0 to 1. One can note the good agreement between experimental and simulated data at a high frequency (above 7 GHz) while small discrepancies appear for the modes represented with black open symbols. However, these discrepancies are not surprising since these modes are certainly very localized (edge modes) and are known to be strongly sensitive to small defects [170, 199, 171] (roughness of the nano-holes, small variation of the nano-holes diameter or in the composition just near the nano-holes,...) that are difficult to simulate precisely. Similar results have been obtained in the CSA system. A typical spectrum recorded at 8 GHz is presented in figure 6.3-e) showing again two pronounced peaks (red and blue stars) and one weaker peak (green star). We note that the peaks are closer in term of energy. Indeed, the difference between the two pronounced modes is $\sim$ 300 Oe for the

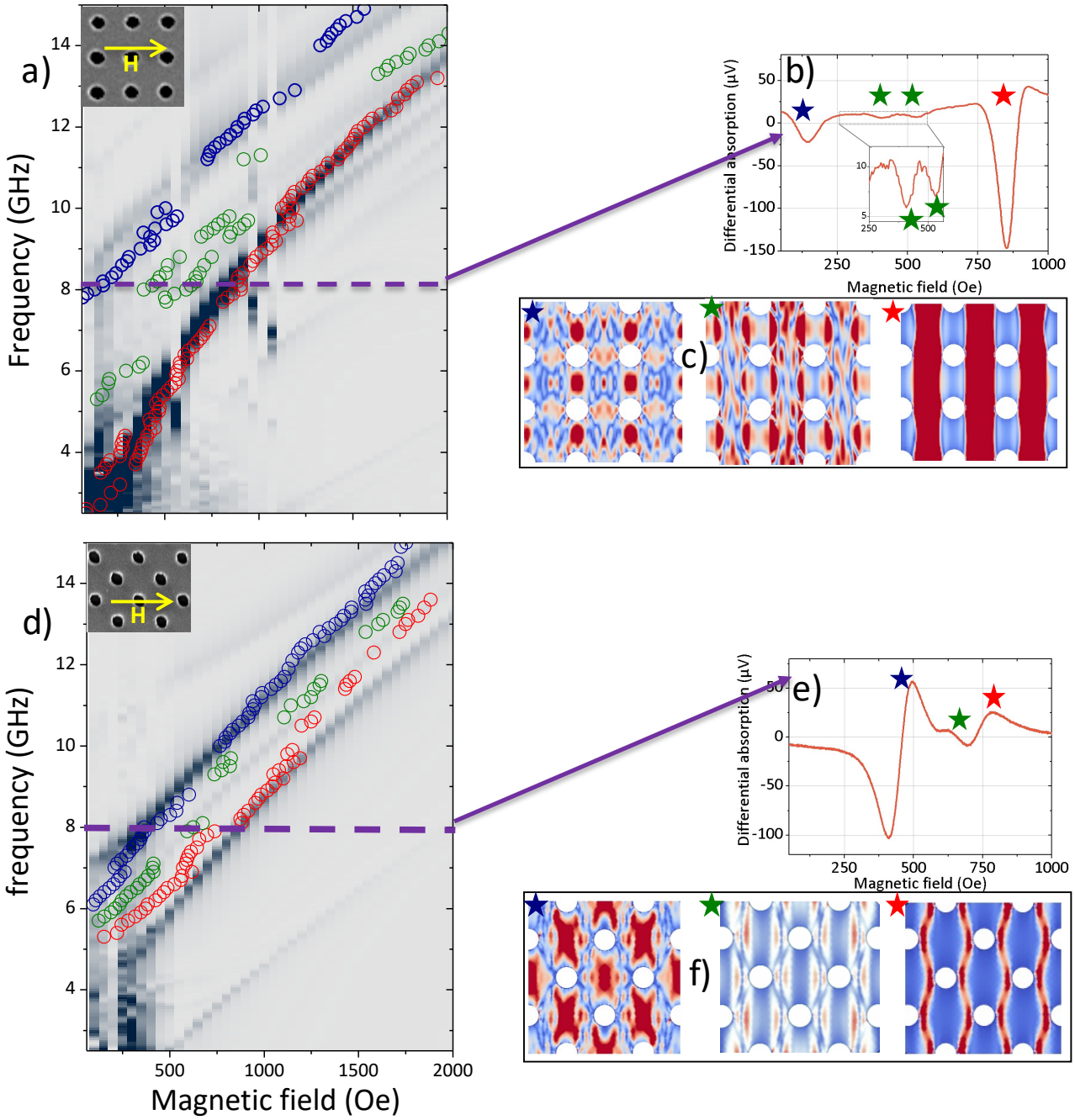

Figure 6.3: Experimental and numerical results obtained with a magnetic field applied along x-axis in absence of electric field for the two studied systems. a-c) SA system and d-f): CSA system. a),d)) Frequency as function of the applied magnetic field. The colors correspond to the relative power spectrum density obtained by micromagnetic simulations while the open symbols are experimental data. b),e) Typical experimental spectrum recorded at 8 GHz, the stars are used to identify the different peaks. c),f) Spin precession amplitudes at $H = 750$ Oe (applied along $x-$axis) obtained by micromagnetic simulations (spatial Fourier transform) showing the localization of the modes identified in the FMR spectra. The colors encode m_y component, the red part reflects a high precession amplitude while the blue one means zero precession amplitude. The stars inside the images correlate the mode profiles with positions in the FMR spectra (a) and d)).

CSA system (see figure 6.3-e)) and ~ 800 Oe for the SA system (see figure 6.3-b)). This shrinking of the FMR spectra is confirmed by the whole frequency dependence (see figure 6.3-d)) where the experimental data are represented by open symbols. In addition, we also note a permutation in the relative intensities between the higher frequency (blue star) peak and the lower frequency (red star) one as compared to the SA system. For instance, in figures 6.3-b) and 6.3-e), the intensity ratio between the higher frequency peak and the lower frequency one is $\frac{I^{blue}}{I^{red}} \simeq 0.18$ for the SA system whereas it is $\frac{I^{red}}{I^{blue}} \simeq 0.19$ for the CSA system. In order to precisely determine the microscopic origin of each peak of both systems (SA and CSA), we have used spatial Fourier transform imaging. The main results are presented in figures 6.3-c) and 6.3-f) where mappings of the spin precession calculated for a magnetic field of 750 Oe are presented. The colors encode m_y component, the red part reflects a high spin precession amplitude while the blue one means zero spin precession amplitude. For both systems, all the modes correspond to spin excitation that are localized in more or less extended regions.
Concerning the SA system, we have the confirmation that the higher peak (red star) in intensity corresponds to a mode localized in a broader region than the other ones. This mode corresponds to a "spin wave" that extends through the antidot array and can be considered as a backward volume type mode [198, 200]. Indeed, in first approximation, an effective quantized wave-vector can be associated to this mode along x-axis, i.e. in the direction of the applied magnetic field $\vec{H}$ (and to the static magnetization that is almost homogeneous, at least above 500 Oe) [200]. On the other hand, the higher frequency mode is related to the spin excitation located between neighboring nano-holes and can be considered as a Damon-Eshbach-type mode [88, 201]. Indeed, in this case, an effective quantized wave-vector can be associated to this mode along y-axis, i.e. in the direction perpendicular to the applied magnetic field [200]. Concerning the CSA system, it is interesting to note that higher and lower frequency modes possess profiles quite resembling those obtained for the SA system and can be explained if one remembers that the difference between SA and CSA in the subsection is only a 45° rotation of the applied magnetic field. Furthermore, one can note that the higher frequency mode (blue star) profile is now more extended than the lowest frequency one, explaining the intensity inversion in the FMR spectra. Finally, it is worth noting that the profile evolutions displayed for SA and CSA systems show that the lower frequency mode profile is sharpened along x (and presents an oscillatory profile along y) while the higher frequency one is broadened along y. The effective wave-vector associated to these mode profiles is thus enhanced for the lower frequency mode (red stars) when switching from SA to CSA system while it is reduced for the higher frequency mode (blue stars). Consequently these evolutions yield an increase of the lower frequency mode energy and a decrease of the higher frequency mode energy because of exchange contribution and can explain the closeness of the FMR peak modes in the CSA system as compared to the SA one.
After this magnetic mode identifications, it is important to link it with the strain distributions in the antidot systems induced by the application of an electrical voltage inside the PZT substrate. This evaluation has been performed thanks to full-field modeling and is presented in the next subsection.

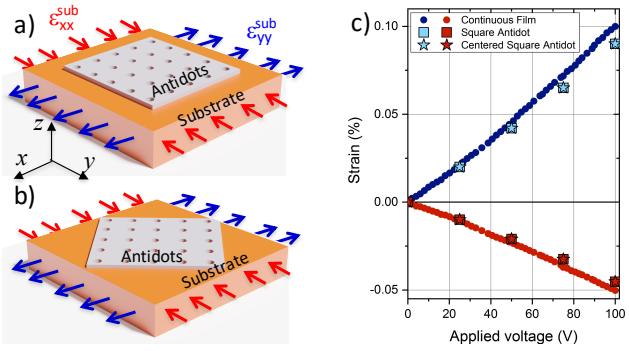

Figure 6.4: a-b) Sketches of the simulated systems, SA and CSA . The imposed strains to the Kapton® layer $\varepsilon_{xx}^{\text{sub}}$ and $\varepsilon_{yy}^{\text{sub}}$ are the ones determined from digital image correlation measurements in the continuous film system.c) Mean values of in-plane strain components (ε_{xx} and ε_{yy}) measured in the film system and calculated in the SA and CSA systems.

6.2 Heterogeneous strain fields and the substrate/ film mechanical contrast effects

As discussed in the introduction, the voltage induced strain field distribution is heterogeneous in our antidot arrays due to the presence of free surfaces and is enhanced by the mechanical contrast between Kapton® and $Ni_{60}Fe_{40}$ material as we will see in this subsection. We have first characterized the strains in the continuous film that are totally transmitted between the PZT substrate and the top surface of continuous film by using the Digital Image Correlation technique from optical tracking of the mottled surface; more details about this technique can be found in ref. [17]. The deduced mean in-plane strain components (ε_{xx}^{sub} and ε_{yy}^{sub}) as a function of the applied voltage (by step at around 2 V) are presented in figure 6.5-b) (blue and red circles). One can note that ε_{xx}^{sub} is found to be positive and ε_{yy}^{sub} is found to be negative in the range (0-100 V) and that they vary almost linearly. The maximum values at 100 V are found to be $\sim 0.1 \times 10^{-2}$ for ε_{xx}^{sub} and $\sim -0.05 \times 10^{-2}$ for ε_{yy}^{sub}. Moreover, non-linear and hysteretic behaviors for ε_{xx}^{sub} and ε_{yy}^{sub} can be observed if the voltage is swept backward from 100V to 0V (not shown here) due to the intrinsic properties of the PZT substrate [202]. DIC measurements performed in the antidot systems show similar results. Indeed, the resolution of our DIC technique was not sufficient to depict local strain heterogeneities at the surface of the antidot systems. This is the reason why we have decided to perform numerical simulations using COMSOL Multiphysics® software [92].
Figures 6.4-a) and 6.4-b) show a schematic presentation of the simulated systems: SA (a) and CSA (b). The strain values imposed on the Kapton® layer are those derived from DIC measurements. We have applied four pairs of strains to the Kapton® layer corresponding to applied voltage of 25, 50, 75 and 100 V. In the simulations, we assumed

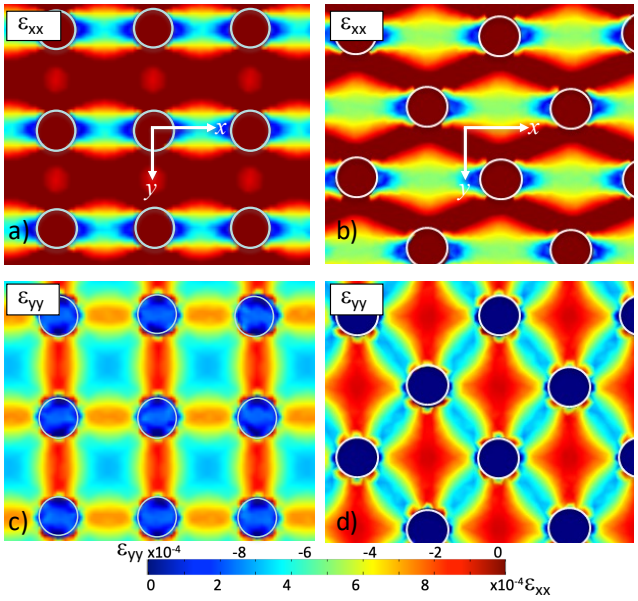

Figure 6.5: 2D mapping of the in-plane strains (ε_{xx} and ε_{yy}) in the SA (a-b) and CSA (c-d) systems. These maps have been obtained with imposed strains corresponding to a voltage of 100V.

isotropic mechanical properties for both Kapton® ($Y_{\text{Kapton}} = 4$ GPa for the Young's modulus and $\nu_{\text{Kapton}} = 0.3$ for the Poisson's ratio) and $Ni_{60}Fe_{40}$ materials ($Y_{Ni_{60}Fe_{40}} = 205$ GPa and $\nu_{Ni_{60}Fe_{40}} = 0.3$ obtained by a homogenization method from the bulk material [174]). As experimentally observed by DIC, the mean in-plane strains calculated in the antidot arrays are close to the one of the continuous film. Indeed, in figure 6.5-b), we have reported the calculated mean in-plane strains inside the antidot systems (square symbols correspond to the SA system while stars correspond to the CSA system). In addition, we have also estimated the mean strains for a continuous film of the same xy dimensions, one can note that the calculated mean strains are also very close to the one imposed by the Kapton® layer.

However, while the strain distributions are homogeneous in the continuous film, they are very heterogeneous in the antidot systems. For instance, figures 6.5-a-c) and 6.5-b-d) show the calculated strain distributions at the top surface of the SA and CSA systems under 100 V. We clearly observe local strain variations of several tens of percent. Note that the scale color of ε_{xx} is positive while it is negative for ε_{yy}. Interestingly, one can see that to some extent, the strain fields mimic the magnetic profiles whatever the direction of the imposed principal strain and the static applied magnetic field, respectively. Indeed, for instance, we retrieve the oscillating behavior of the low frequency mode in the CSA system through an oscillating ε_{xx} strain field and the more localized profile of the high frequency mode between nano-holes in the CSA system through the ε_{yy} strain field .

Moreover, as for the magnetic mode profiles evolution between SA and CSA system, we found that the ε_{xx} strain field is sharpened while the ε_{yy} strain field is broadened. These behaviors are certainly due to the symmetry of the antidot array which imposes in a certain sense these magnetic and mechanical "confinements" of the magnetic modes and of the strain fields, respectively. Afterward, we will take advantage of this symmetry to study the influence of these local strains on the magnetic mode energies because this will impose heterogeneous magnetoelastic fields that *in fine* will mimic the strain distributions.
Finally, as written before, this heterogeneity is *a priori* enhanced by greater mechanical contrast between the antidot and the Kapton® strained by the PZT substrate. In this highly mechanically contrasted system ($Y_{Ni_{60}Fe_{40}}$ = 205 GPa, Y_{Kapton} = 4 GPa), we obtain a range of strains that can vary over two orders of magnitude. However, we wanted to show that this heterogeneity is indeed much lower for the systems with lower mechanical contrast. For this purpose, simulations varying the Young's modulus of the supporting layer were carried out. The results are shown in figure 6.6 representing the 2D strain field for a Kapton® layer and a 1D profile for substrates of various Young moduli, for ε_{xx} (figure 6.6-a)) and ε_{yy} (figure 6.6-b)). It is clearly seen that the amplitude of the strain variation decreases as the Young's modulus increases, *i.e.* as the mechanical contrast decreases. In this case, for an applied voltage of 100 V, the strain state in the substrate is given by ε_{xx} = 0.1% and ε_{yy} = -0.05%. Even if the homogeneous strain state is never reached because of the nano-holes, it is still approached when the Young's modulus of the substrate is close to that of the antidot, as it would be the case for a rigid substrate (around 200 GPa). And, on the contrary, when the supporting layer is very compliant like Kapton®, the strains can be much higher or much lower than those imposed on the substrate. This shows that the high substrate compliance is a determining factor in the search for highly contrasted local magnetoelastic fields over the entire surface of the antidot, thus allowing very diverse variations in localized mode frequencies to be obtained by controlling strain heterogeneities in antidot systems.

6.3 Strain control of the localized magnetic modes

As discussed before, mapping of the elastic strain field and of the magnetic modes has highlighted some similarities that will be very helpful in this subsection. Indeed, due to obvious square-symmetry reasons, the magnetic mode profiles remain unchanged if a transverse in-plane magnetic field is applied (i. e. along y-axis), except that their localization pattern undergoes a 90° rotation [198]. On the other hand, the elastic strain field remains unchanged because it is not sensitive to this applied magnetic field. Thus, a given magnetic mode can be studied under two distinct strain states geometry by successively applying the magnetic field along x and y.

Figures 6.7-a-c) present typical FMR spectra at zero applied voltage (blue lines) and at 100 V (red lines) from the reference continuous film, the SA and the CSA systems,

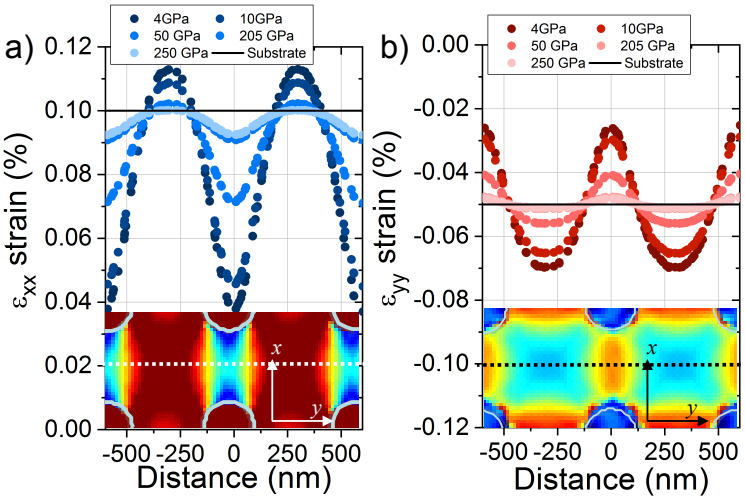

Figure 6.6: Evolution of the strains heterogeneities as function of the mechanical contrast between the antidots and the substrate: a-b) Profiles of in-plane strains (ε_{xx} (a), ε_{yy} (b)) for different values of the Young's modulus substrate, from 4 GPa to 250 GPa. The cut-lines are indicated by dashed lines in the maps. The in-plane strains of the substrate have been fixed at $\varepsilon_{xx} = 1 \times 10^{-3}$ and $\varepsilon_{yy} = -0.5 \times 10^{-3}$.

respectively. These spectra have been recorded in similar conditions, i.e. at 8 GHz and by applying a static magnetic field along x. All the spectra present a shift of all the absorption peaks. As previously mentioned, the continuous film presents a unique peak which corresponds to the uniform precession mode. We observe an up-shift of its resonance field ($\sim$ 96 Oe at 100 V) which means that the magnetostriction coefficient is positive. By applying the methodology presented in ref. [16], one can quantitatively determine the magnetostriction coefficient λ. Thus, the resonance field shift $\delta H_{res} = H_{res}(0) - H_{res}(\mathrm{V})$ can be well fitted using the following relation for an applied magnetic field along x [124, 202]:

$$H_{res} = \sqrt{\left(2\pi M_s - \frac{3\lambda}{M_s}\sigma_{yy}^{sub}(\mathrm{V})\right)^2 + \left(\frac{2\pi f}{\gamma}\right)^2} - 2\pi M_s - \frac{3\lambda}{M_s}\left(2\sigma_{xx}^{sub}(\mathrm{V}) - \sigma_{yy}^{sub}(\mathrm{V})\right) \tag{6.1}$$

where $\sigma_{xx}^{sub}(\mathrm{V})$ and $\sigma_{yy}^{sub}(\mathrm{V})$ are the in-plane principal stress tensor components of the film calculated from the measured in-plane strains $\varepsilon_{xx}^{sub}(\mathrm{V})$ and $\varepsilon_{yy}^{sub}(\mathrm{V})$ and the Hooke's law [10]. Under these conditions, the magnetostriction coefficient is found to be $\lambda = 12\times10^{-6}$. This value has been obtained by fitting the whole δH_{res} voltage as presented in figures 6.8 and 6.9 where the black symbols are experimental data and the black line is the calculated fit. In the following, we assumed that λ is the same for $Ni_{60}Fe_{40}$ antidots which have been elaborated at same time.

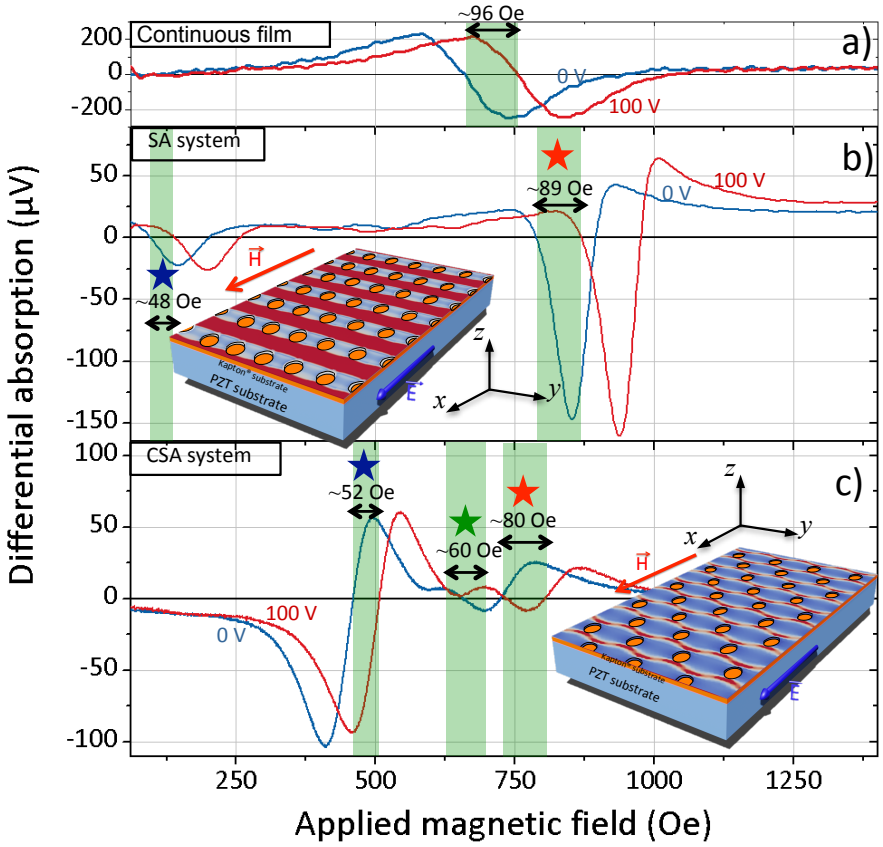

Figure 6.7: Typical 8GHz-FMR spectrum obtained at 0V (blue lines) and at 100 V (red lines) for the continuous film (a), the SA system (b) and the CSA one with a magnetic field applied along x. Sketches presenting the SA and CSA system are also depicted to see the coordinates; the mapping correspond to the low frequency mode in both cases (red stars in the spectra).

Concerning the SA and CSA spectra presented in figures 6.7-b) and c), we clearly observe that all the modes also present an up-shift which is however lower in magnitude than that in the continuous film. In addition, the shifts are not similar for all peaks in a specific system. For instance, in the SA system, the high frequency mode (blue star) presents a shift of $\sim$ 50 Oe while it is around 90 Oe for the low frequency one (blue star). A similar tendency is observed in the CSA system, the high frequency mode (blue star) presents a $\sim$ 50 Oe shift while it is around 80 Oe for the low frequency one. The weaker mode in intensity (green star) presents an intermediate shift of around 60 Oe. Thus, we have conducted FMR measurements in the range 0-100 V with a step of 1V at 8 GHz. Figures 6.8-a) and 6.9-a) present the resonance field shifts of the different modes as a function of the applied voltage. It should be noted that, for the SA system, we do not plot the results of the two satellite peaks (green stars in figure 6.3) because of their weak intensities giving too dispersed results as a function of the applied voltage. This can be seen in the δH_{res} voltage dependence of the CSA modes: the higher the initial intensity of the modes, the lesser noise is generated by the voltage dependence. We have the confirmation that lower field shifts are obtained for the antidot systems as compared to the continuous film. Interestingly, the FMR shift is very different for the high frequency and low frequency modes in both antidot systems. We are convinced that this is due to their spatial localization and consequently to the local magnetoelastic field that is strongly heterogeneous as discussed in the precedent subsection. To confirm this assumption, we have taken advantage of the square-symmetry to perform measurements with an applied magnetic field along y. All other things being equal, only the magnetic modes have their localization rotated by 90° [198], notwithstanding the quality of the arrays that we have tested by FMR. Indeed, at zero applied voltage, the frequency dependencies as a function of an applied magnetic field obtained at 0 and 90° are very similar in both systems (not shown here). This can be seen in the mapping of the strain field and of the the magnetic mode profiles presented in figures 6.8-a and 6.9-b). In each figure, we have plotted the ε_{xx} and ε_{yy} strain fields as well as the profile of each studied magnetic modes. We clearly see that a specific mode (the high frequency mode of the SA system for instance) sees its profile rotate by 90° while the strain fields remain unchanged. The corresponding δH_{res} voltage dependencies are presented in figures 6.8-a) and 6.9-b) for the SA and CSA systems, respectively. To more directly compare the results, we have plotted $-\delta H_{res}$ values.

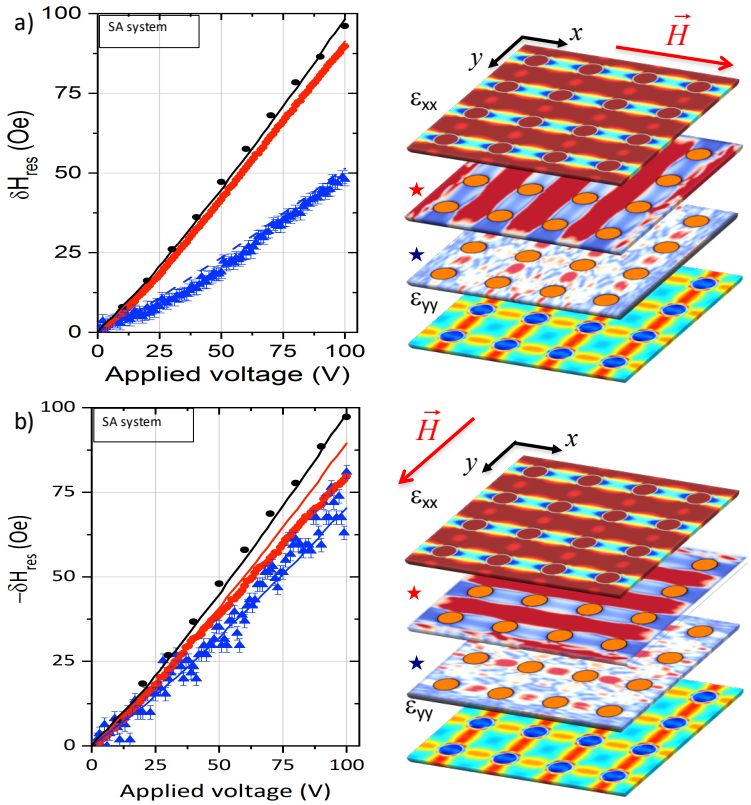

Figure 6.8: Resonance field shift as function of the applied voltage for the two systems with a magnetic field applied along (a-b) and perpendicular (c-d) to the PZT substrate. The different magnetic mode profiles are represented by maps where the colors encode either m_y (in a) or m_x (in b) components. We also present the maps of the in-plane strains (ε_{xx} and ε_{yy}) calculated in the antidot array systems. The colored symbols correspond experimental data while the color lines are calculated using the different α_{xx} and α_{yy} (see table 6.1). The black lines and symbols (full and dotted) correspond to experimental data and simulated line for the continuous film .

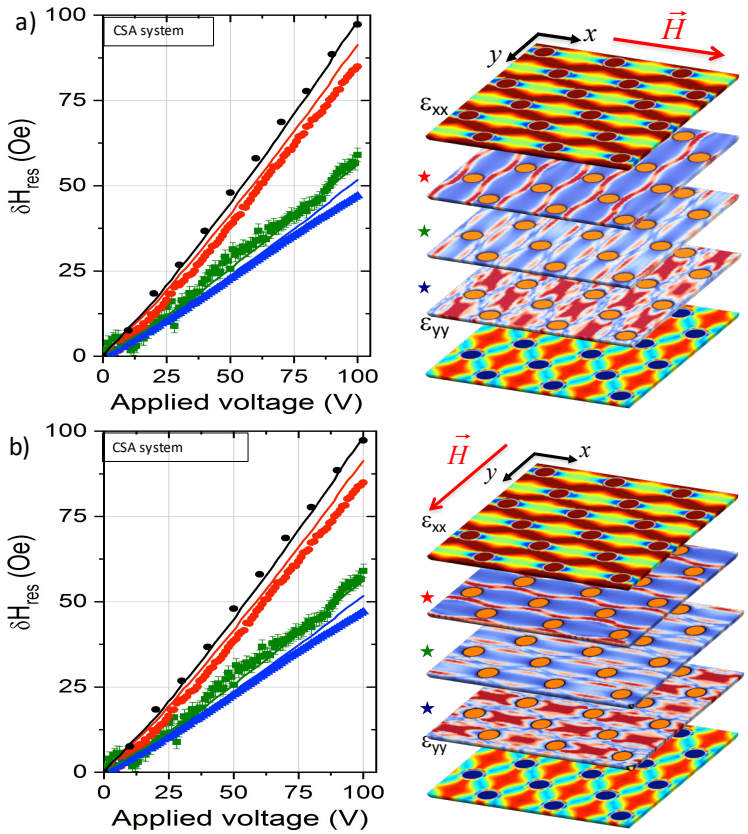

Figure 6.9: Resonance field shift corresponding to the CSA system with the steady magnetic field applied along (in a) or perpendicularly (in b) to the PZT substrate. Magnetic and strain spatial cartographies calculated in the two cases (parallal and perpendicular applied field to the PZT substrate axes).

Magnetic mode	$\vec{H} \parallel \vec{x}$		$\vec{H} \parallel \vec{y}$	
	α_{xx}	α_{yy}	α_{xx}	α_{yy}
	Continuous film			
Uniform Mode	100	100	100	100
	Square Array			
High Frequency Mode ★	0.67	0.55	0.92	0.43
Low Frequency Mode ★	0.79	1.03	0.94	0.92
	Centered Square Array			
High Frequency Mode ★	0.59	0.47	1.05	0.85
Satellite Mode ★	0.56	0.72	1.01	0.69
Low Frequency Mode ★	0.78	1.01	0.66	0.54

Table 6.1: Strain transmission factors α_{xx} and α_{yy} for the different modes and configurations , i. e. $\vec{H}$ along or perpendicular to the main axis of the PZT substrate (along x or y).

For the SA system, the low frequency mode (red star) is only slightly affected by this rotation (δH_{res} evolves from $\sim$ 90 Oe to $\sim$ 80 Oe at 100 V) while the high frequency one (blue star) is more seriously affected (δH_{res} evolves from $\sim$ 50 Oe to $\sim$ 85 Oe at 100 V). This also applies to the CSA system, we clearly see that three studied modes are differently affected. Indeed, the low frequency mode then the high frequency one and finally the "satellite" mode are increasingly affected by this rotation. Indeed, the δH_{res} amplitude at 100 V increases by $\sim$ 5, $\sim$ 10 and $\sim$ 25 Oe, respectively. So, we have an evidence that the differentiated evolution of these modes depends on the local strain field experienced by each mode. Thus, from the results obtained in the two previous subsections, we extracted the local strain field by making a mask for each magnetic mode which we stick on the elastic strain distribution maps to extract mean values for $\langle \varepsilon_{xx}^{mode} \rangle$ and $\langle \varepsilon_{yy}^{mode} \rangle$. Then, one can define two factors that express the strain localization (α_{xx} and α_{yy}) [124]:

$$\alpha_{xx} = \frac{\langle \varepsilon_{xx}^{mode} \rangle}{\langle \varepsilon_{xx}^{sub} \rangle} \qquad \text{and} \qquad \alpha_{yy} = \frac{\langle \varepsilon_{yy}^{mode} \rangle}{\langle \varepsilon_{yy}^{sub} \rangle} \tag{6.2}$$

The different extracted values are reported in table 6.1 for each mode. One can note good correlation between α_{xx} and α_{yy} values and the FMR peak shift of each corresponding mode. For instance, the α_{xx} and α_{yy} values of the low frequency mode are bigger in the four studied situations in comparison to the low frequency mode values which effectively presents higher δH_{res} variations. Those values also corroborate the wide δH_{res} variations of magnetic modes when applying the magnetic field at 0° and 90°. It is for instance the case for the high frequency mode in the SA system whose maximum values of δH_{res} at 100

V increase from ~ 50 Oe to ~ 85 Oe while the $(\alpha_{xx}; \alpha_{yy})$ evolves from $(67; 55)$ to $(92; 43)$ and for the satellite magnetic mode (green) of the CSA system which δH_{res} values at 100 V evolves from ~ 55 Oe to ~ 80 Oe while the $(\alpha_{xx}; \alpha_{yy})$ evolves from $(56; 72)$ to $(101; 69)$. In addition, as pointed out in the previous subsection, some α_{xx} and α_{yy} are found to be higher than 100% meaning that the magnetic mode is located in a region where we have a concentration of the strain higher than the imposed one. Finally, we have used simple modeling by using equation 6.1 and by replacing $\sigma_{xx}^{sub}(\mathrm{V})$ by $\sigma_{xx}^{mode} = \alpha_{xx}\sigma_{xx}^{cf}(\mathrm{V})$ and $\sigma_{yy}^{sub}(\mathrm{V})$ by $\sigma_{yy}^{mode} = \alpha_{yy}\sigma_{yy}^{cf}(\mathrm{V})$ to try to fit the experimental data. The continuous lines in figure 6.8 and 6.9 are the corresponding fits. It is worth noting that we have made no supplementary fit than the one performed for the continuous film when determining λ. One can note good correlation between the modeling and the experimental data. This good correlation is partly due to the fact that the studied magnetic modes correspond to a static situation where the magnetization are almost uniform.

Conclusion

The objectives of the present thesis are articulated around two main aspects, namely a numerical aspect which consisted in setting up a non-exhaustive numerical code for the study of the effects of magnetoelastic couplings in flexible magnetic systems and a purely experimental aspect which consisted in studying the magnetoelastic properties in magnetic systems nanostructured or not on flexible substrates. The whole allows to give a new insight on the relations between strain distribution and static and dynamic magnetic properties.

Regarding the numerical aspect of the work, a finite element code has been developed in the Comsol Mutliphysics® software in order to simulate, in a fully coupled way, the magnetoelastic effects in magnetic nanostructures by taking into account their elastic deformation state, which is not possible in the commonly used classical micromagnetic codes. In fact, it is possible to include a known strain field in OOMMF but it must be spatially uniform. Thus, the development of the present code in ComSol Mutliphysics® has been an important step towards a good understanding and prediction of the effects resulting from the mechanical loading of magnetic nano-objects. The code has been implemented and validated by following different elementary steps and comparing the results obtained with those from Nmag simulations. Different application examples were simulated such as the Larmor precession phenomenon which was compared with the analytical form, the magnetization equilibrium and the magnetostatics in different nano-objects (disks, spheres and nanowires). The results obtained in the case of magnetostatic studies were compared with those obtained by simulating the same situation, the same object with the same magnetic parameters under Nmag. Our results were in good agreement with those obtained from the calculations made with the Nmag software. Indeed, a comparison of the temporal evolution of the demagnetization field and magnetization was made between the results obtained from the two codes (Nmag and in-house code). This comparison showed small discrepancies. We also performed calculations on the magnetoelastic effects in which we highlighted the effects of mechanical heterogeneities and the shape of the prototypical object. Two configurations were studied, the supported nanowire (deposited on a flexible substrate) and the self-supported nanowire subjected to the equivalent homogeneous strain field. These phenomena have been studied in static and dynamic cases. In the dynamic study, it was shown that the only difference between the two cases (homogeneous and heterogeneous deformed objects) consists in the difference of the trajectories of magnetization and the initiation of the movement of magnetic moments. Thus, we observed that in the case of a homogeneous strain of a magnetostrictive object, the reversal of the magnetization is coherent and its trajectory presents attenuated concentric circles whereas the heterogeneous deformation

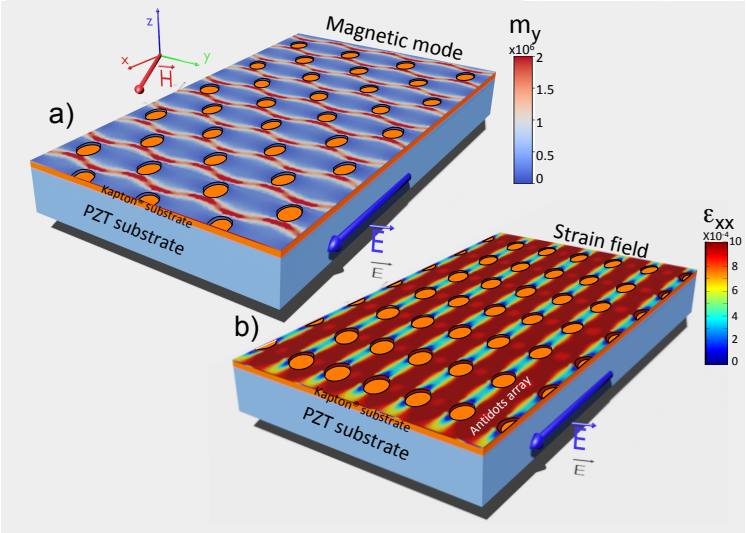

Figure 6.10: 3D schem of antidot nanostructres with the simulated micromagnetic modes (a) and micromechanical strain fiels.

presents less coherence in the trajectory and floating phenomena were observed on the temporal evolution of the components of the magnetization. This flutter comes from the initiation of the movement of the spins located in the zones undergoing a higher value of deformation than elsewhere in the object and propagates under the exchange interaction. This phenomenon can be likened to an avalanche effect. A fast Fourier transform was performed on the components of the oscillating magnetization showing that in fact, in the case of homogeneous deformation, there is mainly one excited mode while we found at least two modes in the case of heterogeneous deformation. However, the estimated area under the FFT curves in both cases is the same which confirms the fact that the conservation of magnetic energy is respected. Note that a magnetoelastic module resembling our code was developed in Mumax in 2021 [203], showing that these approaches are needed by the nanomagnetism community.

Until now, magnetomechanical properties have been the subject of many experimental studies in continuous thin films on flexible systems subjected to small or large strains. However, the effect of nanostructuring has not been studied in flexible systems subjected to small strains. The objective of this thesis was also to experimentally characterize the effects of magnetoelastic coupling in one- and two-dimensional nanostructures. We thus performed *in situ* deformation tests (with a ferroelectric actuator) combined with ferromagnetic resonance. The link with the numerical part is that the strain fields are potentially very heterogeneous. Moreover, numerical calculations are essential to interpret the experiments properly. To this end, we chosen to study these effects in the case of materials showing significant magnetostriction (but not giant) such as $Ni_{60}Fe_{40}$. The nanostructures studied are fabricated by interference lithography and concern arrays of

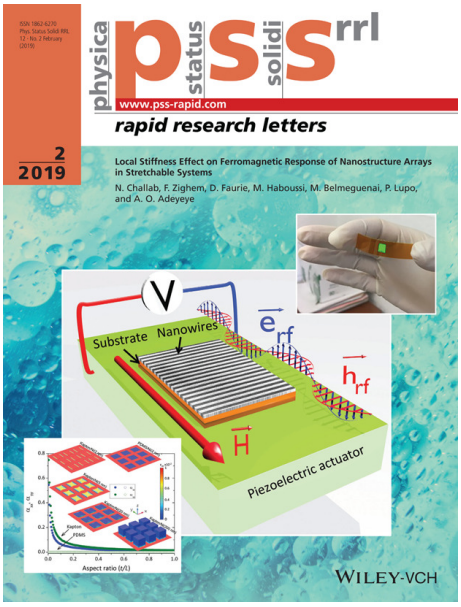

Figure 6.11: Back cover of PSS-RRL [204]

nanowire with a width of 480 nm and a period of 600 nm as well as arrays of antidot with a diameter of 250 nm and a period of 600 nm. These different lateral structuring give rise to very different strain distributions. While the nanowires are subjected to relatively homogeneous strain (but very different from the substrate strain), the antidots are subjected to very complex strain fields. This has been analyzed by numerical calculations. As a preamble, a continuous layer of the same thickness fabricated under the same conditions with the same material was also studied in order to have reference results (with homogenous strain fully transmitted from the substrate). These reference results served as a basis to determine the effects of patterning on the magnetomechanical behavior. These nanostructures and continuous film were fabricated with $Ni_{60}Fe_{40}$ having a magnetostriction of about 11×10^{-6}.
It is well known in micromagnetism that the nanostructuration results in localized and confined modes[205] (figure-6.10-a). It is also well known in the field of mechanics that the effects of systems with defects or geometric contrasts result in a concentration of stress and a heterogeneous distribution of the strain and stress field over the considered systems [206] (figure-6.10-b). A methodology was emmployed to localize and estimate the magnetomechanical effect in nanostrured surface. First, we made an identification of the magnetic oscillation modes in the considered nanostructures. After that, we estimated the local concentration ratio of the different strain tensor components used in the analytical model for estimating the spectral shifts due to the presence of the strain.
Using this methodology, it was possible to study the behavior of the different modes in which we were interested in the two types of nanostructures, keeping the same static magnetic parameters used in the case of the continuous film, *i.e.* magnetization, gyro-

magnetic factor and magnetostriction coefficient. This provides additional leverage for the manipulation and control of magnetic modes in future applications in spintronics, straintronics and flexible magnonics. From my point of view, my thesis has advanced the state of the art on the heterogeneous magnetomechanical properties of nanostructures. These heterogeneities are seen in a global sense since they concern the mechanical fields and the localization of the magnetic modes. This type of study will probably become more widespread as the miniaturization of components and the increasingly complex nanoarchitectures will generate this kind of complex coupled phenomena. 4 articles were published in international journals [124, 73, 207, 208], while one of them have been object of the RSS-RRL back cover (see figure 6.11).

Perspectives

The perspectives concerning my research group are numerous and currently follow two axes. The first one concerns the influence of large strains damage on magnetization curves, including new development of original experiments. As shown throughout this manuscript, flexible or stretchable systems are very promising in different applications in different fields. In this context, the thesis of Hatem Ben Mahmoud which started in October 2020 is a continuation of the present studies, namely the study of the influence of large strains on magnetic properties. The project concerns the study of the anisotropy induced by plastic deformation/multicracking on continuous thin films and nanostructures deposited on flexible substrates.

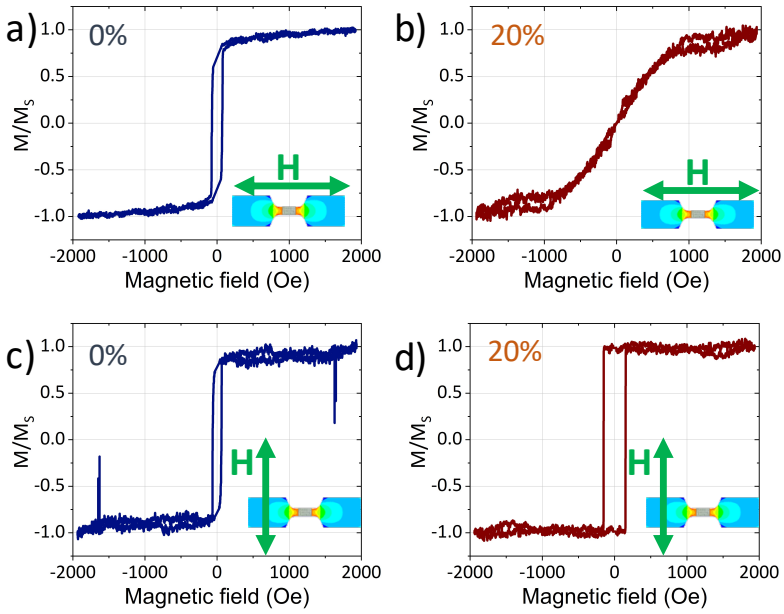

Figure 6.12: Anisotropy tailoring in continuous magnetic thin films deposited on flexible substrate and deformed in plastic regim. Typical MOKE hysterisis loop without plastic deformations (a-c) and in presence of plastic deformation (20% strain)

Figures 6.12 show typical hysteriss loops obtained with the corresponding sketches displaying the applied field directions with respect to the applied loading. This study is carried out *in situ* with MOKE to get relationship between plastic deformation, crack apparition and magnetic anisotropy. Two extrem values of the induced strain are choosen

in the present example (0% and 20%) obtained with a prior calibration using the well-known digital image correlation. One can see the possibility to change the anisotropy axis from easy axis to a hard axis natures (6.12a) showing an easy axis which is transformed to a hard axes as displayed in 6.12b)). The other situation consists on reinforcing an existant easy axis and induce an increasing in the coercitive magnetic field by changing the steady magnetic field direction to a perpedicular direction with respecte to the applied displacement axis. These transformation are due to the negative magnetostriction coefficient of the cobalt film.
On the other hand, magnetic nanostructures deposited also on flexible substrates will be studied using the same setup. These nanostructres concern dot arrays deposited on flexible substrate or interfaced with magnetic continuous film (figure-6.13).

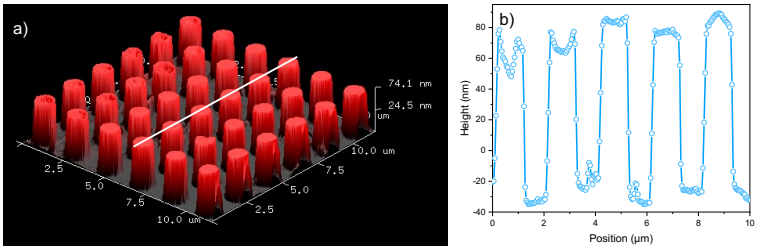

Figure 6.13: Permalloy dot arrays deposited on Kapton® substrate. a) Topographic image of the considered arrays obtained form atomic force microscopy characterization and b) lineprofile of the height versus position.

The geometrical and magnetic properties combined give rise to different magnetic configurations especially with the effect of interfaces and volumes as can be seen in figure6.14[209]. This latter represents topographic images of Py dots deposited on a cobalt continuous film in c) and in Py in b). Here are two examples of votex configuration in the first nanostructure and magnetic domain in the seconde one.

The objective here is the study of small and high strains on the magnetic configuration in such nanostructures. This is prospective of the possibility to change the equilibrium states in such nanostructures [210] or to stabilise and to stimulate other situations of equilibrium with a view to applications in spintronics, particularly in the field of information storage. Exploratory micromagnetic simulations were performed using the geometrical parameters obtaind from atomic force microscopy (AFM) in order to get a mapping of the most intense and visible magnetic mode in such nanostructres (figure-6.15 and figure-6.16). These results have been confronted with the preliminary results obtained from ferromagnetic resonance spectroscopy. The same methodology that the one used during this thesis will be adopted in the present case. Namely, the localization of the modes we are interested in, the simulation of the deformation transmitted to the nanostructures and the estimation of the induced effect.

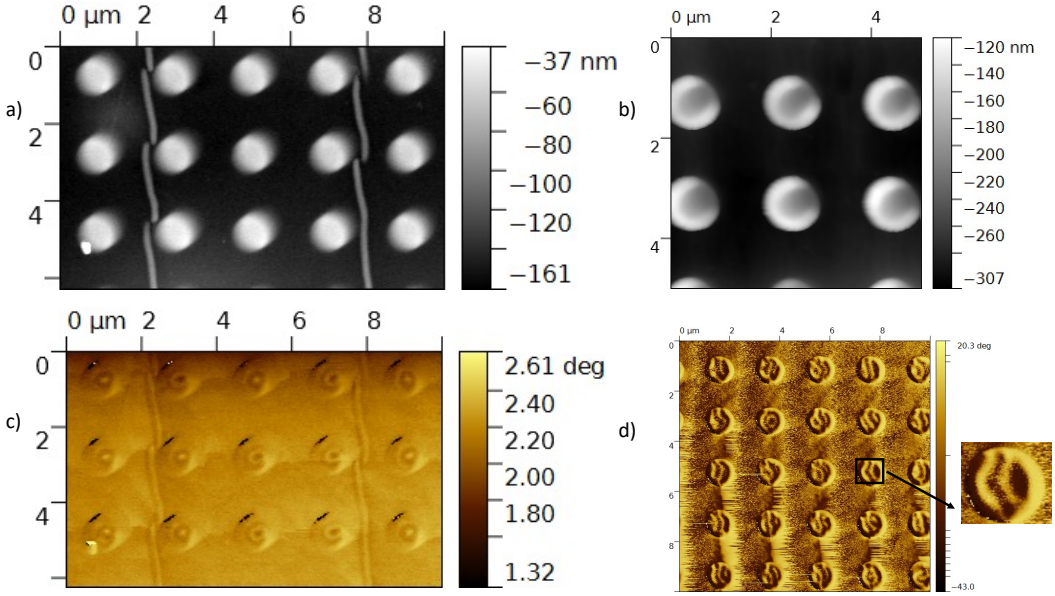

Figure 6.14: Permalloy dot deposited on a) cobalt continuous film and b) permalloy continuous film, repectively with the accompagned magnetic configuration c) related to the a) topography and d related to the b) topographic image.

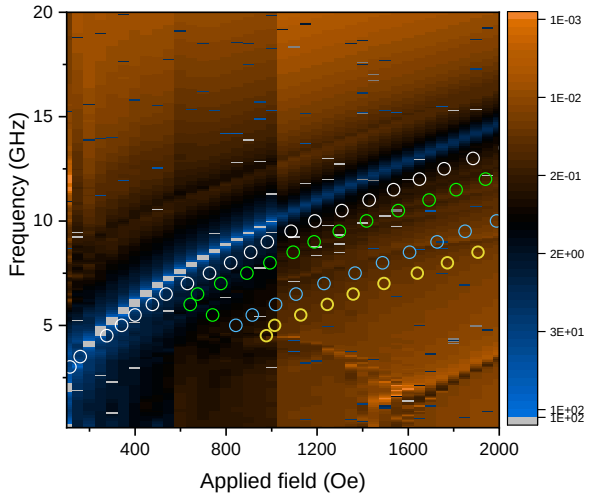

Figure 6.15: Frequency dependance calculated using OOMMF software using geometrical characteristics obtained form AFM topography. The colorbar indicates the intensity of the calculated spectral response.

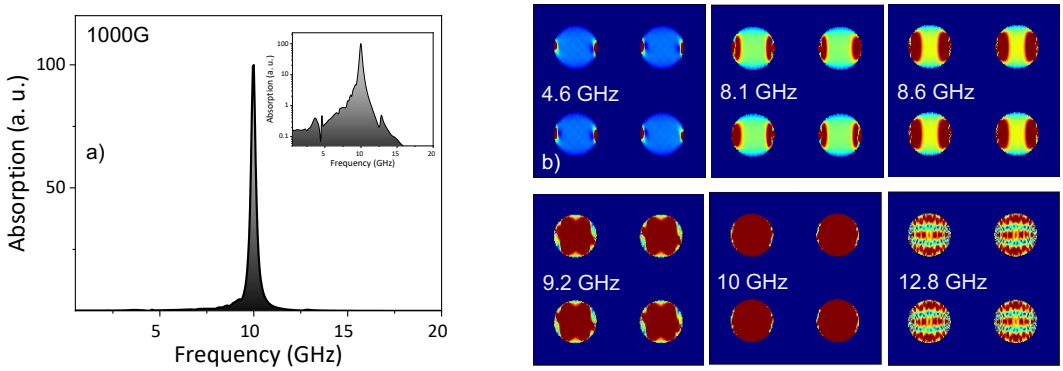

Figure 6.16: a) Typical calculated spectrum in the case of the Py dot array inder 1000G magnetic field applied in plane of the sample. b) Magnetic mode profiles in Permalloy dots of 1μm diameter. The calculations were performed for 1000 Oe applied field in the longitudinal direction and the magnetization is excited with a sinc radiofrequency field applied in the transversal direction of the applied steady field.

Calculations using ComsolMultiphysics® (figure-6.17) show for a nanostructure with the same geometrical characteristics (1um diameter dots with a periodicity of 2 um) the transmitted strain is strongly heterogeneous and is essentially concentrated in the center of each cylinder. The spatial extension of each dot being small (very important free surfaces) would allow us, according to the estimations made using the same calculation, to go to higher deformations without causing the deterioration of the nanostructures by inducing cracks propagation.

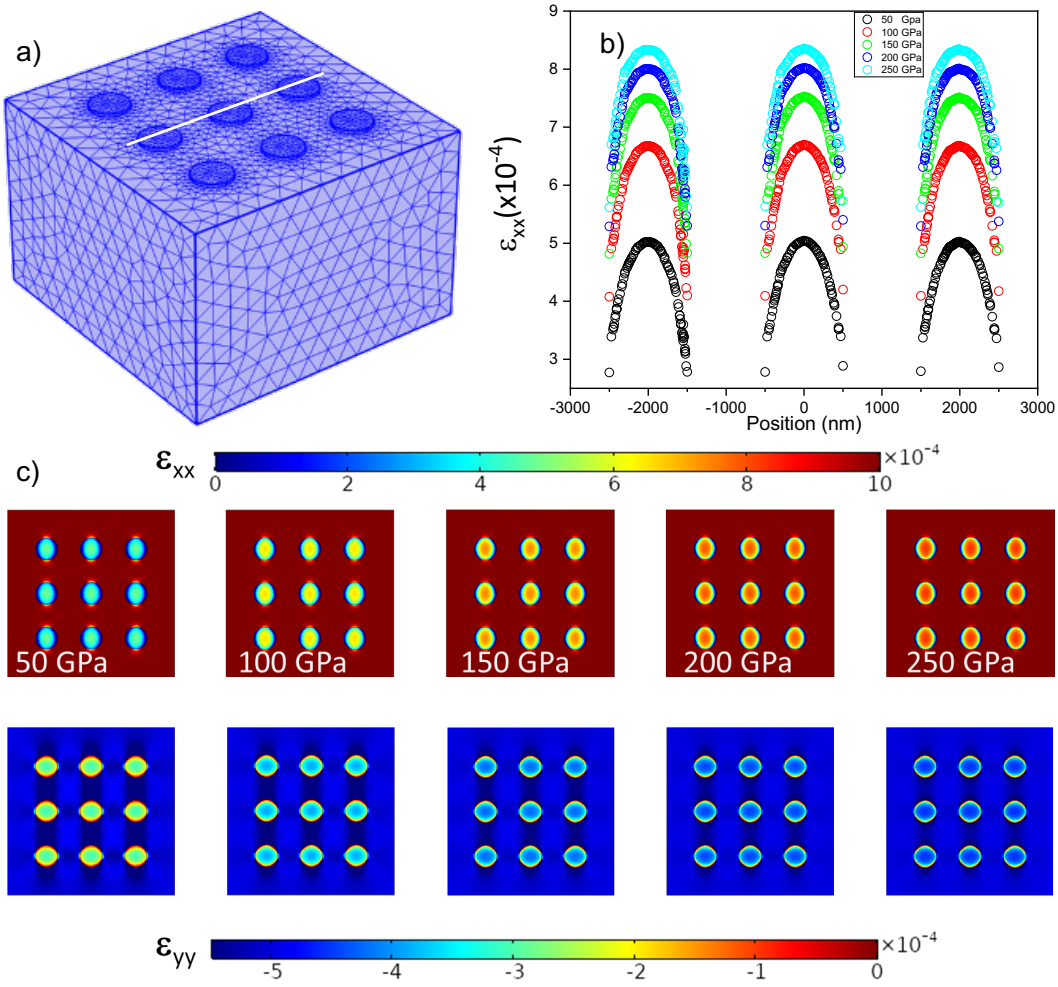

Figure 6.17: a) Snapshot of the mesh distribution generated by ComsolMultiphysics® mesher, b) strain x-component line profile on the top surface of the Permalloy dots for a fixed value of the Kapton® Young moduli and dots Young modulus ranging in 50 GPa to 250GPa , c)Spatial carthography of the x and y-component of the strain tensor in the case of of 80 nm height and 1 μm diameter dots deposited on Kapton® substrate sbmitted to uni-axial strain essay.

An other project is starting and concerns the PhD thesis of Stephan Chiroli, which will begin in September 2021. The ElecAcouSpin project funded by ANR is dealing with the study of the coupling between phononic and magnonic properties of nanostructure arrays [211, 212], and the strain effects on the band structures. The magnonics crystals being exhibit also phononic band structures[211, 213] making the interraction between the two type of band structures possible. To descriminate the coupling effects within the nanostructres, its is important to "manipulate" separately the two bands. The de-

termining factors in the case of phononic band structures being mainly the density of the material used and its elastic properties as well as the geometric factors of the nanostructure makes it difficult to manipulate the phononics branches with imposed strain in a reversible way. On the other hand, it has been demonstrated the possibility to manipulate the branches of the magnetic band structure by applying an external magnetic field inducing a gap of the order of GHz. This gap increasing depends on the intrinsic properties of the used materials during the fabrication of the crystal and the geometrical properties[214]. Considering the induced gap opening, it should be sufficient to control the coupling between the two band structures which arise in the same artificial crystal. Then, the project concerns first the identification and the understanding of the strain effects and magnetomechnical couplings on the magnonic band structures including the effects of deformation heterogeneities[58] on such nanostructures after what the effect of the induced changes in this latter on the phononic ones. Numerical simulations being very important and prominent factor to good understanding and forecasting particularly the determination of the geormetrical and intrinsic properties of such crystal making then possible such coupling between the to band structures. Actually, it is also planned to continue the development of the code built during this thesis in order to go towards the simulation of phononic and magnonic band structures, as well as the different effects induced by the presence of a deformation field and the identification of the mutual interractions between the two. The success of such a project would open the door to a new type of applications and a new generation of electronic devices combining high efficiency, multiphysical characteristics and adaptability to different media as they would be flexibles.

Abstract

Since its discovery in 1847 by Joule, magnetoelasticity has not ceased to be studied not only for its most fundamental aspects but also for its potential application area. This phenomenon has become particularly popular in recent years because it is involved more or less directly in various types of magnetic systems that are widely studied in the magnetism community. Among these, we can mention the flexible magnetic systems which are generally composed of a magnetic deposit (thin layers or multilayers which can be nanostructured) on a polymeric substrate whose applications range from everyday gadgets to aerospace devices. During their use, these devices will be subjected to strong (and complex) deformations that can modify the magnetic properties *in operando*. For these applications, the influence of magnetoelasticity can be undesirable and it is therefore necessary to find solutions to limit its effects. On the other hand, magnetoelasticity can be advantageously used to control magnetic (and electronic) properties through the application of controlled elastic strains: this has given rise to an emerging thematic commonly called "straintronics" which includes, for example, "strain-mediated artificial multiferroics". This magnetoelasticity is also found in so-called flexomagnetic systems, which can induce complex magnetic configurations.

The objectives of this thesis are based on two main aspects: i) a numerical aspect which consists in setting up a numerical code for the study of the effects of magnetoelastic couplings in flexible magnetic systems and ii) an experimental aspect which consists in studying the magnetoelastic properties in nanostructured magnetic systems on flexible substrates. The whole allows to give a new light on the relations between the distribution of the deformations and the static and dynamic magnetic properties. Concerning the numerical aspect, a finite element code has been developed under Comsol Mutliphysics® in order to simulate, in a fully coupled way, the magnetoelastic effects in magnetic nanostructures by taking into account their elastic deformation state, which is not possible in the classical micromagnetic codes commonly used in the magnetism community. The development of this code was an important step towards a good understanding and prediction of the effects resulting from complex mechanical loading of magnetic nano-objects. Based on these predictions, we have studied the dynamic magnetic response of magnetic nanostructure arrays under controlled deformations (using a ferroelectric actuator). A methodology has been developed to localize and estimate the magnetoelastic effects in nanostructured surfaces. First, we proceeded to the spatial and temporal identification of the magnetic oscillation modes in the considered nanostructures. Then, we estimated the local concentration ratio of the different components of the strain tensor to estimate the spectral shifts due to the presence of the deformation. Thanks to this methodology, it was possible to study the behavior of the different modes of interest in two types of nanostructures. The results obtained provide an additional lever for the manipulation

and control of magnetic modes in future applications in spintronics, straintronics and flexible magnonics.

Résumé

Depuis sa découverte en 1847 par Joule, la magnétoélasticité n'a céssé d'être étudiée non seulement pour ses aspects des plus fondamentaux mais également pour ses aspects applicatifs. Ce phénomène connaît un engouement particulier ces dernières années en raison du fait qu'il intervient plus ou moins directement dans différents types de systèmes magnétiques très étudiés au sein de la communauté du magnétisme. Parmi ces derniers, on peut citer les sytèmes magnétiques flexibles qui sont générallement composés d'un dépôt magnétique (couches minces ou multicouches qui peuvent être nanostructurées) sur un substrat polymère dont les applications vont de gadgets de la vie quotidienne aux dispositifs aérospatiales. Durant leurs utilisations, ces dispositifs vont être soumis à de fortes (et complexes) déformations qui peuvent modifier les propriétés magnétiques *in operando*. Pour ces applications, l'influence de la magnétoélasticité peut être indésirable et il convient dès lors de rechercher des solutions afin d'en limiter les effets. A contrario, la magnétoélasticité peut être avantageusement utilisée pour contrôller les propriétés magnétiques (et électroniques) par le biais de l'application de déformations élastiques contrôllées: cela a donné naissance à une thématique émergente que l'on nomme communément "straintronique" qui englobe par exemple les composés multiferroïques artificiels ("strain-mediated artificial multiferroics"). Cette magnétoélasticité se retrouve également dans des systèmes dits "à gradient de déformations" induisant ainsi des configurations magnétiques complexes.

Les objectifs de cette thèse s'articulent autour de deux aspects principaux: i) un aspect numérique qui a consisté à mettre en place un code numérique pour l'étude des effets des couplages magnétoélastiques dans les systèmes magnétiques flexibles et ii) un aspect expérimental qui a consisté à étudier les propriétés magnétoélastiques dans des systèmes magnétiques nanostructurés sur des substrats flexibles. L'ensemble permet de donner un nouvel éclairage sur les relations entre la distribution des déformations et les propriétés magnétiques statiques et dynamiques. Concernant l'aspect numérique, un code d'éléments finis a été développé sous Comsol Mutliphysics® afin de simuler, de manière totalement couplée les effets magnétoélastiques dans des nanostructures magnétiques en prenant en compte leur état de déformation élastique, ce qui n'est pas possible dans les codes micromagnétiques classiques couramment utilisés au sein de la communauté du magnétisme. Le développement de ce code a été une étape importante vers une bonne compréhension et prédiction des effets résultant d'un chargement mécanique complexe de nano-objets magnétiques. Fort de ces prédictions, nous avons étudié la réponse magnétique dynamique de réseaux de nanostructures magnétiques sous déformations contrôllées (par le biais d'un actionneur ferroélectrique). Une méthodologie a été développée pour localiser et estimer les effets magnétoélastique dans des surfaces nanostructurées. Tout d'abord, nous avons procédé aux identifications spatiale et temporelle

des modes d'oscillations magnétiques dans les nanostructures considérées. Ensuite, nous avons estimé le rapport de concentration local des différentes composantes du tenseur de déformation pour estimer les décalages spectraux dus à la présence de la déformation. Grâce à cette méthodologie, il a été possible d'étudier le comportement des différents modes qui nous intéressaient dans deux types de nanostructures. Les résultats obtenus fournissent un levier supplémentaire pour la manipulation et le contrôle des modes magnétiques dans de futures applications en spintronique, en straintronique et en magnonique flexible.

List of Figures

Bibliography

[1] R. Streubel, P. Fischer, F. Kronast, V. P. Kravchuk, D. D. Sheka, Y. Gaididei, O. G. Schmidt, and D. Makarov. *J. Phys. D: Appl. Phys.*, 49:363001, 2016.

[2] V. P. Kravchuk, D. D. Sheka, R. Streubel, D. Makarov, O. G. Schmidt, and Y. Gaididei. *Phys. Rev. B*, 85:144433, 2012.

[3] O.V. Pylypovskyi, V. Kravchuk, D. D. Sheka, D. Makarov, O. G. Schmidt, and Y. Gaididei. *Phys. Rev. Lett.*, 114:197204, 2015.

[4] D. D. Sheka, O. V. Pylypovskyi, P. Landeros, Y. Gaididei, A. KÃ¡kay, and D. Makarov. *Com. Phys.*, 3:128, 2020.

[5] D. I. Khomskii. *J. Magn. Magn. Mater.*, 306:1, 2006.

[6] Y. Tokura. *Science*, 312:1481, 2006.

[7] N. A. Spalding, S-W. Cheong, and R. Ramesh. *Phys. Today*, 63:10, 2010.

[8] V. Garcia, M. Bibes, and A. Barthélémy. *C. R. Phys.*, 16:168, 2015.

[9] J.-M. Hu, L. Q. Chen, and C.-W. Nan. *Adv. Mater.*, 18:15, 2016.

[10] F. Zighem, D. Faurie, S. Mercone, M. Belmeguenai, and H. Haddadi. *J. Appl. Phys.*, 114:073902, 2013.

[11] R. Cai, V.-A. Antohe, Z. Hu, B. Nysten, L. Piraux, and A. M. Jonas. *Adv. Mater.*, 29:1604604, 2017.

[12] N. Lei, T. Devolder, G. Agnus, P. Aubert, L. Daniel, J.-V. Kim, W. Zhao, T. Trypiniotis, R. P. Cowburn, C. Chappert, D. Ravelosona, and P. Lecoeur. *Nat. Com.*, 4:1378, 2013.

[13] M. Ha, G. S. C. Bermúdez, T. Kosub, I. Mönch, Y. Zabila, E. S. O. Mata, R. Illing, Y. Wang, J. Fassbender, and D. Makarov. *Advanced Materials*, 33:2005521, 2021.

[14] S. Merabtine, F. Zighem, D. Faurie, A. Garcia-Sanchez, P. Lupo, and A. Adeyeye. *NanoLetters*, 18:3199, 2018.

[15] M. Gueye, B. M. Wague, F. Zighem, M. Belmeguenai, M. S. Gabor, T. Petrisor Jr., C. Tiusan, S. Mercone, and D. Faurie. *Applied Physics Letters*, 105:062409, 2014.

[16] M. Gueye, F. Zighem, M. Belmeguenai, M. Gabor, C. Tiusan, and D. Faurie. *Journal of Physics D: Applied Physics*, 49:265001, 2016.

[17] F. Zighem, M. Belmeguenai, D. Faurie, H. Haddadi, and J. Moulin. *Review of Scientific Instruments*, 85:103905, 2014.

[18] C. Kittel. *Physical Review*, 73:155, 1948.

[19] M. Farle. *Reports on Progress in Physics*, 61:755, 1998.

[20] S. S. Kalarickal, P. Krivosik, M. Wu, C. E. Patton, M. L. Schneider, P. Kabos, T. J. Silva, and J. P. Nibarger. *Journal of Applied Physics*, 99:093909, 2006.

[21] S. Beguhn, Z. Zhou, S. Rand, X. Yang, and J. Lou. *Journal of Applied Physics*, 111:07A503, 2012.

[22] Y. Ding, T. J. Klemmer, , and T. M. Crawford. *ournal of Applied Physics*, 96:2969, 2004.

[23] M. Belmeguenai, F. Zighem, Y. Roussigné, S-M. Chérif, P. Moch, K. Westerholt, G. Woltersdorf, and G. Bayreuther. *Physical Review B*, 79:024419, 2009.

[24] M. Belmeguenai, M. S. Gabor, F. Zighem, N. Challab, T. Petrisor Jr, R. B. Mos, and C. Tiusan. *Journal of Physics D: Applied Physics*, 51:045002, 2018.

[25] M. Gueye, F. Zighem, D. Faurie, M. Belmeguenai, and S. Mercone. *Applied Physics Letters*, 105:052411, 2014.

[26] M. Gueye, F. Zighem, M. Belmeguenai, M. S. Gabor, C. Tiusan, and D. Faurie. *Journal of Physics D: Applied Physics*, 49:145003, 2016.

[27] M. Liu et al. W. Liu. *Advanced Functional Materials*, 28:1705928, 2018.

[28] A. V. Khvalkovskiy, R. Chepulskii, R. S. Beach, A. Ong, X. Tang, A. Driskill-Smith, W. H. Butler, P. B. Visscher, D. Lottis, E. Chen, V. Nikitin, and M. Krounbi. *J. of Phys. D: Applied Physics*, 46:074001, 2013.

[29] S Yuasa and D D Djayaprawira. *Journal of Physics D: Applied Physics*, 40:R337, 2007.

[30] K. Nagasaka. *Journal of Magnetism and Magnetic Materials*, 321:508, 2009.

[31] F. Zighem, A. El Bahoui, J. Moulin, D. Faurie, M. Belmeguenai, S. Mercone, and H. Haddadi. *Journal of Applied Physics*, 116:123903, 2014.

[32] L. Shen, G. Lan, L. Lu, C. Ma, C. Cao, C. Jiang, H. Fu, C. You, X. Lu, Y. Yang, L. Chen, M. Liu, and C. âL. Ji. *Advanced Science*, 5:1800855, 2018.

[33] B. Li, M. N. Kavaldzhiev, and J. Kosel. *Journal of Magnetism and Magnetic Materials*, 378:499, 2015.

[34] W. Karboul-Trojet, D. Faurie, Y. Roussigné, S. M. Chérif, P. O. Renault, and Ph. Goudeau. *Journal of Physics D: Applied Physics*, 44:155002, 2011.

[35] G. Dai, Q. Zhan, Y. Liu, H. Yang andX. Zhang, B. Chen, and R.-W. L. *Applied Physics Letters*, 100:122407, 2012.

[36] X. Zhang, Q. Zhan, G. Dai, Y. Liu, Z. Zuo, H. Yang, B. Chen, and R.-W. Li. *Journal of Applied Physics*, 113:17A901, 2013.

[37] Z. Tang, B. Wang, and H. Yang. *Applied Physics Letters*, 105:103504, 2014.

[38] B. Özkaya, S. R. Saranu, S. Mohanan, and U. Herr. *Physica Status Solidi (a)*, 205:1876, 2008.

[39] T. Uhrmann, L. Bar, T. Dimopoulos, N. Wiese, M. Ruhrig, and A. Lechner. *Journal of Magnetism and Magnetic Materials*, 307:209, 2006.

[40] Y. F. Chen, J. McCord, J. Freudenberger, R. Kaltofen, and O. G. Schmidt. *Journal of Applied Physics*, 105:07C302, 2009.

[41] D. Cao, Z. Wang, L. Pan, H. Feng, X. Cheng, Z. Zhu, J. Wang, Q. Liu, and G. Han. *Applied Physics A*, 122:938, 2016.

[42] A. Bedoya-Pinto, M. Donolato, M. Gobbi, L. E. Hueso, and P. Vavassori. *Applied Physics Letters*, 104:062412, 2014.

[43] G. Lin, D. Makarov, M. Melzer, W. Si, C. Yan, and O. G. Schmidt. *Lab on a Chip*, 14:4050, 2014.

[44] D. Karnaushenko, D. Makarov, M. Stöber, D. D. Karnaushenko, S. Baunack, and O. G Schmidt. *Advanced Materials*, 27:880, 2015.

[45] M. Kondo, M. Melzer, D. Karnaushenko, T. Uemura, S. Yoshimoto, M. Akiyama, Y. Noda, T. Araki, O. G. Schmidt, and T. Sekitani. *Science Advances*, 6:eaay6094, 2020.

[46] M. Melzer, D. Makarov, and O.G. Schmidt. *Journal of Physics D: Applied Physics*, 53:083002, 2019.

[47] J.-Y. Chen and J.-P. Wang. *Nature Electronics*, 1:96, 2018.

[48] S. Ota, A. Ando, and D. Chiba. *Nature Electronics*, 1:124, 2018.

[49] M. Melzer, A. Kopylov, D. Makarov, and O. G. Schmidt. *Spin*, 3:1340005, 2013.

[50] W. Karboul-Trojet, D. Faurie, E. Aït-Yahiatène, Y. Roussigné, F. Mazaleyrat, and S. M. Chérif. *Journal of Applied Physics*, 111:07A926, 2012.

[51] W. Karboul-Trojet, Y. Roussigné, D. Faurie, , and S.M. Chérif. *European Physical Journal B*, 85:339, 2012.

[52] N. Thi Lan, S. Mercone, J. Moulin, A. El Bahoui, D. Faurie, F. Zighem, M. Belmeguenai, and H. Haddadi. *Journal of Magnetism and Magnetic Materials*, 373:259, 2015.

[53] G. Dai, X. Xing, Y. Shen, and X. Deng. *Journal of Physics D: Applied Physics*, 53:055001, 2020.

[54] T. Fischbacher, M. Franchin, G. Bordignon, and H. Fangohr. *IEEE Transactions on Magnetics*, 43:2896, 2007.

[55] M.J. Donahue and D.G. Porter. *OOMMF Userâs Guide, Version 1.0*. NIST, 1999.

[56] G. Venkat, M. Franchin, O. Dmytriiev, M. Mruczkiewicz, H. Fangohr, A. Barman, M. Krawczyk, and A. Prabhakar. *IEEE Transactions on Magnetics*, 49:524, 2013.

[57] W. Eerenstein and J. N. D. Mathur. *Nature*, 442:759, 2006.

[58] C.-Y. Liang, S.M. Keller, A.E. Sepulveda, A. Bur, W.-Y. Sun, K. Wetzlar, and G.P. Carman. *Nanotechnology*, 25:435701, 2014.

[59] T. Mathurin, S. Giordano, Y. Dusch, N. Tiercelin, P. Pernod, and V. Preobrazhensky. *Physical Review B*, 95:140405, 2017.

[60] Z. Xiao, R. Lo Conte, C. Chen, C. Y. Liang, and A. Sepulveda. *Scientific Reports*, 26:5207, 2018.

[61] K. Darrow. *Bell System Technical Journal*, 15:224, 1936.

[62] A. G. Gurevich and G. A. Melkov. *Magnetization Oscillations and Waves*. CRC Press, 1996.

[63] A. Aharoni and R. Kronstein. *Introduction to the Theory of Ferromagnetism*. Oxford Science Publications, 2000.

[64] R.C.O'Handleya. *Encyclopedia of Physical Science and Technology*. 2003.

[65] N. Ashcroft and W. Mermin. *Solid State Physics*. Brooks/ Cole, 1976.

[66] C. Kittel. *Introduction to Solid State Physics*. John Wiley and Sons, 1953.

[67] V. Vleck. *The theory of electric and magnetic susceptibilities*. Oxford University Press, 1932.

[68] J. A. Osaorn. *Phys. Rev.*, 67:351, 1945.

[69] A. Aharoni. *Jou. Appl. Phys*, 83:3432, 1998.

[70] J. Staunton, P. Strange, B. L. Gyorffy, M. Matsumoto, J. Poulter, H. Ebert, and N. P. Archibald. *Theory of Magnetocrystalline Anisotropy in The Effects of Relativity in Atoms Molecules and the Solid State 295*. Springer, 1991.

[71] J.-A. Serret and G. Darboux. *uvres de Lagrange Tome 11*. Gauthier-Villars, 1868.

[72] C. Kittel. *Phys. Rev.*, 76:743, 1949.

[73] N. Challab, A.D. Aboumassound, F. Zighem, D. Faurie, and M. Haboussi. *Journal of Physics D: Applied Physics*, 52:355004, 2019.

[74] L.D. Landau and E. Lifshitz. *Phys. Z. Sowjetunion*, 8:101, 1935.

[75] A.A.Pilla, D.J.Muehsam, and M.S.Markov. *Bioelectrochemistry and Bioenergetic*, 43:239, 1997.

[76] T. Gilbert. *Phys. Rev.*, 100:1243, 1955.

[77] M. Lakshmanan. *Phil. Trans. R. Soc. A*, 369:1280, 2011.

[78] D. Polder. *Phil. Mag.*, 40:99, 1949.

[79] J. Smit and H.G. Beljers. *Philips Res. Rep.*, 10:113, 1955.

[80] J.O. Artman. *Phys. Rev.*, 105:74, 1957.

[81] C. Kittel. *J. Phys. Radium*, 12:291, 1951.

[82] R. W. Damon and H. Van De Vaart. *Jou. Appl. Phys.*, 36:3435, 1965.

[83] R.W.Damon and J.R.Eshbach. *J. of Phys. and Chem. of Solids*, 19:308, 1961.

[84] J. R. Eshbach and R. W. Damon. *Phys. Rev.*, 118:1208, 1960.

[85] D. D. Stancil. *Theory of Magnetostatic Waves*. Springer, 1993.

[86] A. A. Serga, A. V Chumak, and B. Hillebrands. *J. Phys. D. Appl. Phys.*, 43:264002, 2010.

[87] C. Bayer, J. Jorzick, B. Hillebrands, S. O. Demokritov, R. Kouba, R. Bozinoski, A. N. Slavin, K. Y. Guslienko, D. V. Berkov, N. L. Gorn, and M. P. Kostylev. *Phys. Rev. B*, 72:064427, 2005.

[88] F. Zighem, Y. Roussigné, S.-M. Chérif, and P. Moch. *J. Phys.: Condens. Matter*, 19:176220, 2007.

[89] M. Belmeguenai, H. Tuzcuoglu, M. Gabor, T. Petrisor, C. Tiusan, D. Berling, F. Zighem, and S. M. ChÃ©rif. *J. Magn. Magn. Mater.*, 373:140, 2015.

[90] M. Grimsditch, A. Malozemoff, , and A. Brunsch. *Phys. Rev. Lett.*, 43:711, 1979.

[91] A. Baker, M. Beg, G. Ashton, M. Albert, D. Chernyshenko, W. Wang, S. Zhang, M. A.Bisotti, M. Franchin, C. L. Hu, R. Stamps, T. Hesjedal, and H. Fangohr. *Journal of Magn. and Magn. Mat.*, 421:428, 2017.

[92] *see https://www.comsol.com.*

[93] B. M. Jones. *Mechanical of composite materials.* Taylor & Francis, 1998.

[94] K. M. Knowles and P. R. Howie. *J. Elasticity*, 120:87, 2015.

[95] R. J. Schiltz Jr., T. S. Prevender, and J. F. Smith. *Journal of Applied Physics*, 42:4680, 1971.

[96] J. F. Nye. *Physical Properties of Crystals: Their Representation by Tensors and Matrices.* Oxford Science Publications, 1958.

[97] S. Hirsekorn. *Texture Stress and Microstructure*, 12:1, 1990.

[98] J. M. J. d. Toonder, J. A. W. v. Dommelen, and F. P. T. Baaijens. *Modelling Simul. Mater. Sci. Eng.*, 7:909, 1999.

[99] N. Challab, F.Zighem, D. Faurie, M. Haboussi, M. Belmeguenai, P. Lupo, and A. O. Adeyeye. *Physica Status Solidi (RRL)*, 13:1800509, 2018.

[100] *See https://www.comsol.com/support/knowledgebase/1270.*

[101] R. Chang, S. Li, M. V. Lubarda, B. Livshitz, and V. Lomakin. *J. Appl. Phys.*, 109:07D358, 2011.

[102] A. Puzrin. *Equations of Continuum Mechanics / Chapter 5*, volume 55. Springer, 2012.

[103] H. Forster, T. Schrefl, W. Scholz, D. Suess, V. Tsiantos, and J. Fidler. *Journal of Magnetism and Magnetic Materials*, 249:435701, 2002.

[104] H. Fangohr, T. Fischbacher, M. Franchin, G. Bordignon, J. Generowicz, A. Knittel, and M. Walter. *NMAG User Manual.* 2009.

[105] D.-X. Chen, J.A. Brug, and R.B. Goldfarb. *IEEE Transactions on Magnetics*, 27:3601, 1991.

[106] D. R. Fredkin and T. R. Koehler. *IEEE Transactions on Magnetics*, 26:415, 1990.

[107] H. B. Callen and N. Goldberg. *J. Appl. Phys.*, 36:976, 1965.

[108] R. C. Peng, J.-M. Hu, L.-Q. Chen, and C.-W. Nan. *NPG Asia Materials*, 9:e404, 2017.

[109] D. Makarov, M. Melzer, D. Karnaushenko, and O. G. Schmidt. *App. Phys. Rev.*, 3:011101, 2016.

[110] X. Shi, W. Mi, Q. Zhang, and X. Zhang. *Appl. Phys. Lett.*, 117:132401, 2020.

[111] H. Matsumoto, S. Ota, T. Koyama, and D. Chiba. *Appl. Phys. Lett.*, 118:022406, 2021.

[112] S. Ota, Y. Hibino, D. Bang, H. Awano, T. Kozeki, H. Akamine, T. Fujii, T. Namazu, T. Takenobu, and T. Koyama. *Appl. Phys. Expr.*, 9:043004, 2016.

[113] S. Ota, M. Ono, H. Matsumoto, A. Ando, T. Sekitani, R. Kohno, S. Iguchi, T. Koyama, and D. Chiba. *Appl. Phys. Expr.*, 12:053001, 2019.

[114] D. Karnaushenko, D. D. Karnaushenko, D. Makarov, S. Baunack, R. SchÃ€fer, and O. G. Schmidt. *Adv. Mater.*, 27:6582, 2015.

[115] R. Streubel, J. Lee, D. Makarov, M.âY. Im, D. Karnaushenko, R. Schäfer L. Han, P. Fischer, S.âK. Kim, and O. G. Schmidt. *Adv. Mater.*, 26:316, 2014.

[116] F. Gabler, D.D. Karnaushenko, D. Karnaushenko, and O. G. Schmidt. *Nat. Commun.*, 10:3013, 2019.

[117] A. Fernández-Pacheco, R. Streubel, O. Fruchart, R. Hertel, P. Fischer, and R. P. Cowburn. *Nat. Commun.*, 8:15756, 2017.

[118] O. M. Volkov, A. Kákay, F. Kronast, I. Mšonch, M.-A. Mawass, J. Fassbender, and D. Makarov. *Phys. Rev. Lett.*, 123:07720, 2019.

[119] O. V. Pylypovskyi, D. Y. Kononenko, K. V. Yershov, U. K. Röbler, A. V. Tomilo, J. Fassbender, J. Van den Brink, D. Makarov, and D. D. Sheka. *Nano Lett.*, 11:8157, 2020.

[120] A. A. Bukharaev, A. K. Zvezdin, A. P. Pyatakov, and Y. K. Fetisov. *Physics - Uspekhi*, 61:1175, 2018.

[121] J.-M. Hu, T. Yang, and L.-Q. Chen. *NPJ Comp. Mater.*, 4:62, 2018.

[122] K. Wang, T. Hu, F. Jia, G. Zhao, Y. Liu, I. V. Solovyev, A. P. Pyatakov, A. K. Zvezdin, and W. Ren. *Appl. Phys. Lett.*, 114:092405, 2019.

[123] Y. Wang, C. Wang, S.-J. Liang, Z. Ma, K. Xu, X. Liu, L. Zhang, A. S. Admasu, S.-W. Cheong, L. Wang, M. Chen, Z. Liu, B. Cheng, W. Ji, and F. Miao. *Adv. Mater.*, 32:2004533, 2020.

[124] N. Challab, F. Zighem, D. Faurie, M. Haboussi, M. Belmeguenai, P. Lupo, and A. O. Adeyeye. *Physica Status Solidi (RRL)*, 13:1800509, 2019.

[125] C.-Y. Liang, S. M. Keller, A. E. Sepulveda, W.-Y. Sun A. Bur, K. Wetzlar, and G. P. Carman. *Nanotech.*, 25:355004, 2014.

[126] H. Bommel and K. Dransfeld. *Phys. Rev. Lett.*, 3:83, 1959.

[127] R. L. White, l. H. Solt, and JR. Hgghes. *Phys. Rev.*, 104:56, 1956.

[128] I. Neudecker, G. Woltersdorf, B. Heinrich, T. Okunoc, G. Gubbiotti, and C.H. Backa. *Jou. Magn. Magn. Mat.*, 307:148, 2006.

[129] E. Montoya, T. McKinnon, A. Zamani, E. Girt, and B. Heinrich. *Jou. Magn. Magn. Mat.*, 356:12, 2014.

[130] W. Barry. *IEEE TMTT*, 34:80, 1986.

[131] D. B. Bhat and S. K. Koul. *Transmission Lines for Microwave Integrated Circuits.* New Age International, 1989.

[132] M. Belmeguenai, D. Apalkov, M. Gabor, F. Zighem, G. Feng, and G. Tang. *IEEE*, 54:01, 2018.

[133] C. Lueng, F. Zighem, D. Faurie, and M. Kostylev. *J. App. Phys.*, 122:163901, 2017.

[134] Y. S. Gui, A. Wirthmann, and C.-M. Hu. *Phys. Rev. B*, 80:184422, 2009.

[135] F. Lagattu, J. Brillaud, and M. C. Lafarie-Frenot. *Material characterisation*, 53:17, 2004.

[136] H. Haddadi and S. Belhabib. *Optics and Lasers in Engineering*, 46:185, 2008.

[137] See http://www.ncorr.com/ for more information about Ncorr software.

[138] See http://www.opticist.org/ for more information about Moire software.

[139] See http://www.matchid.org/ for more information about Matchid software.

[140] G. Besnard, F. Hild, and S. Roux. *Experimental Mechanics*, 46:789, 2006.

[141] See https://www.pprime.fr/?q=fr/la photomecanique.

[142] See http://www.gom.com/ for more information about Aramis software.

[143] Gom. mbH. *RAMIS User Manual - Software v6.1 and higher.* Mittelweg 7-8 D-38106 Braunschweig, 2009.

[144] M. Belmeguenai, K. Aitoukaci, F. Zighem, M. S. Gabor, T. Petrisor Jr., R. B. Mos, and C. Tiusan. *Journal of Applied Physics*, 123:113905, 2018.

[145] M. Caminale, A. Ghosh, S. Auffret, U. Ebels, K. Ollefs, F. Wilhelm, A. Rogalev, , and W. E. Bailey. *Phys. Rev. B*, 94:014414, 2016.

[146] I. Benguettat-EL Mokhtari, Y. Roussigné, T. Petrisor Jr., F. Zighem, F. Kail, L. Chahed, V. Pierron, L. Méchin, M. Gabor, and M. Belmeguenai. *PSSB*, 257:2000265, 2020.

[147] H. Nakayama, K. Ando, K. Harii, T. Yoshino, R. Takahashi, Y. Kajiwara, K. Uchida, and Y. Fujikawa. *Phys. Rev. B*, 85:144408, 2012.

[148] Y. Tserkovnyak and A. Brataas. *PHYS. REV. B*, 66:224403, 2002.

[149] M. Gueye, P. Lupo, F. Zighem, D. Faurie, M. Belmeguenai, and A. O. Adeyeye. *EPL*, 114:17003, 2016.

[150] P.J. Kelly and R.D. Arnell. *Vaccum*, 56:159, 2000.

[151] V. Kouznetsov, K. Macak, J. M.Schneider, U. Helmersson, and I.Petrov. *Surface and Coatings Technology*, 122:290, 1999.

[152] W. Khan, Qun Wang, and X. Jin. *Materials*, 11:439, 2018.

[153] W. Mao, I. Wathuthanthri, and Ch. H. Choi. *OPTICS LETTERS*, 36:3176, 2011.

[154] Q. Xie, M.H. Hong, H.L. Tan, G.X. Chen, L.P. Shi, and T.C. Chong. *Journal of Alloys and Compounds*, 449:261, 2008.

[155] H. v. Wolferen and L. Abelmann. *H. v. Wolferen and L. Abelmann*. H. v. Wolferen and L. Abelmann, 2011.

[156] J. H. Seo, J. H. Park, S. I. Kim, B. J.Park, Z. Mal, J. Choi, and B. K. Ju. *Journal of Nanoscience and Nanotechnology*, 14:1521, 2014.

[157] J. d. Boor, N. Geyer, J. V Wittemann, U. Gosele, and V. Schmidt. *Nanotechnology*, 21:095302, 2010.

[158] S. Aksu, A. E. Cetin, R. Adato, and H. Altug. *Advanced Optics Materials*, 1:798, 2013.

[159] J. Arcamone, M. A. F. v. d. Boogaart, F. Serra-Graells, J. Fraxedas, J. Brugger, and F. P.-Murano. *Nanotechnology*, 19:305302, 2008.

[160] F. Yesilkoy, V. Flauraud, M. Ruegg, B.J. Kimb, and J. Brugger. *Nanoscale*, 8:4945, 2016.

[161] R. Libanori, R. M. Erb, A. Reiser, H. Le Ferrand, M. J. Süess, R. Spolenak, and A. R. Studart. *Nat. Commun.*, 3:1265, 2012.

[162] D. H. Kim, J. Xiao, J. Song, Y. Huang, , and J. A. Rogers. *Adv. Mater.*, 22:2018, 2010.

[163] R. M. Erb, K. H. Cherenack, R. E. Stahel, R. Libanori, T. Kinkeldei, N. Münzenrieder, G. Tröster, and A. R. Studart. *ACS Applied Materials and Interfaces*, 4:2860, 2012.

[164] F. Zighem, D. Faurie, M. Belmeguenai, A. Garcia-Sanchez, P. Lupo, and A. O. Adeyeye. *Appl. Phys. Lett.*, 111:052408, 2017.

[165] S. Merabtine, F. Zighem, F. Faurie, A. Garcia-Sanchez, P. Lupo, and Adekunle O. Adeyeye. *NanoLetters*, 18:3199, 2018.

[166] J. Jorzick, S. O. Demokritov, C. Mathieu, B. Hillebrands, B. Bartenlian, C. Chappert, F. Rousseaux, and A. N. Slavin. *Phys. Rev. B*, 60:15194, 1999.

[167] Y. Roussigné, S. M. Chérif, C. Dugautier, , and P. Moch. *Phys. Rev. B*, 63:134429, 2001.

[168] Y. Khivintsev, Bijoy Kuanr, T. J. Fal, M. Haftel, R. E. Camley, Z. Celinski, and D. L. Mills. *Phys. Rev. B*, 81:054436, 2010.

[169] M. J. Pechan and C. Yu. *Journal of Applied Physics*, 97:10J903, 2005.

[170] J. Gadbois and J.G Zhu. *IEEE Trans. Magn.*, 31:3802, 1995.

[171] B. B. Maranvillea, R. D. McMichael, S. A. Kim, W. L. Johnson, C. A. Ross, and J.Y. Cheng. *J. Appl. Phys.*, 99:08C703, 2006.

[172] B. B. Maranville, R. D. McMichael, and D. W. Abraham. *Appl. Phys. Lett.*, 90:232504, 2007.

[173] M. Zhu and R. D. McMichael. *J. Appl. Phys.*, 109:043904, 2011.

[174] P. Djemia, C. Dugautier, , T. Chauveau, E. Dogheche, M. I. De Barros, and L. Vandenbulcke. *J. Appl. Phys.*, 90:3771, 2001.

[175] A. Kanrar and U. S. Ghosh. *J. Appl. Phys.*, 52:5851, 1981.

[176] F. Zighem, D. Faurie, M. Belmeguenai, N. Girodon-Boulandet, M. S. Gabor, and P. Djemia. *J. Phys. D: Appl. Phys.*, 50:455002, 2017.

[177] H. Haddadi and S. Belhabib. *Int. J. Mech. Sci.*, 62:47, 2012.

[178] F. Zighem, D. Faurie, S. Mercone, M. Belmeguenai, and H. Haddadi. *J. Appl. Phys.*, 114:073902, 2013.

[179] S. Djaziri, P.-O. Renault, E. Le Bourhis, Ph. Goudeau, D. Faurie, G. Geandier, C. Mocuta, and D. ThiaudiÃšre. *J. of Appl. Phys.*, 116:093504, 2014.

[180] L. Shen, M. Liu, C. Ma, L. Lu, H. Fu, C. You, X. Lu, and C.-L. Jia. *Mater. Horiz.*, 5:230, 2018.

[181] M. Melzer, M. Kaltenbrunner, D. Makarov, D. Karnaushenko, D. Karnaushenko, T. Sekitani, T. Someya, and O. G. Schmidt. *Nat. Commun.*, 6:6080, 2015.

[182] A. Casiraghi, H.r C.-Leon, M. Vafaee, F. G.-Sanchez, G. Durin, M. Pasquale, G. Jakob, M. KlÃ€ui, and O. Kazakova. *Communications Physics*, 2:145, 2019.

[183] T.T. Nguyen, J. Yvonnet, Q.-Z. Zhu, M. Bornert, and C. Chateau. *Eng. Frac. Mechanics*, 139:18, 2015.

[184] W. Ogierman and G. Kokot. *Materials*, 13:287, 2020.

[185] J. Ding, D. Tripathy, and A. O. Adeyeye. *EPL*, 98:16004, 2012.

[186] G. Gubbiotti, F. Montoncello, S. Tacchi, M. Madami, G. Carlotti, L. Giovannini, J. Ding, and A. O. Adeyeye. *Appl. Phys. Lett.*, 106:262406, 2015.

[187] S. Neusser, B. Botters, M. Becherer, D. Schmitt-Landsiedel, and D. Grundler. *Appl. Phys. Lett.*, 93:122501, 2008.

[188] R. Mandal, S. Saha, D. Kumar, S. Barman, S. Pal, K. Das, A. Kumar Raychaudhuri, Y. Fukuma, Y. Otani, and A. Barman. *ACS Nano*, 6:3397, 2012.

[189] A. Manzin, G. Barrera, F. Celegato, M. Coïsson, and P. Tiberto. *Scientific Reports*, 6:22004, 2016.

[190] I.Maskery, L.Sturm, A.O.Aremu, A.Panesar, C.B.Williams, C.J.Tuck, R.D.Wildman I.A.Ashcroft, and R.J.M.Hague. *Polymer*, 152:62, 2018.

[191] N. Challab, F. Zighem, D. Faurie, M. Haboussi, M. Belmeguenai, P. Lupo, and A. O. Adeyeye. *Phys. Status Solidi (RRL)*, 13:1800509, 2019.

[192] S. Choudhury, S. Majumder, S. Barman, Y. Otani, and A. Barman. *Phys. Rev. Applied*, 10:064044, 2018.

[193] O. N. Martyanov, V. F. Yudanov, R. N. Lee, S. A. Nepijko, H. J. Elmers, R. Hertel, C. M. Schneider, and G. Schönhense. *Phys. Rev. B*, 75:174429, 2007.

[194] M. Bailleul, R. Höllinger, and C. Fermon. *Phys. Rev. B*, 73:104424, 2006.

[195] C. Yu and M. J. Pechan. *Appl. Phys. Lett.*, 83:3948, 2003.

[196] M. Yu, L. Malkinski, L. Spinu, W. Zhou, and S. Whittenburg. *J. Appl. Phys.*, 101:09F501, 2002.

[197] C. Bayer, S. O. Demokritov, B. Hillebrands, and A. N. Slavin. *Appl. Phys. Lett.*, 82:607, 2003.

[198] S. Neusser, B. Botters, and D. Grundler. *Phys. Rev. B*, 78:054406, 2008.

[199] R. D. McMichael and B. B. Maranville. *Phys. Rev. B*, 74:024424, 2006.

[200] F. Zighem, Y. Roussigné, S.M. Chérif, and P. Moch. *J. Phys.: Condens. Matter*, 19:176220, 2007.

[201] G. Gubbiotti, M. Kostylev, S. Tacchi, M. Madami, G. Carlotti, J. Ding, A. O. Adeyeye, F. Zighem, A. A. Stashkevich, E. Ivanov, and S. Samarin. *J. Phys. D: Appl. Phys.*, 47:105003, 2014.

[202] T. Sadat, D. Faurie, P. Godard, D. Thiaudière, P.-O. Renault, and F. Zighem. *J. Phys. D: Appl. Phys.*, 53, 2020.

[203] F. Vanderveken, J. Mulkers, J. Leliaert, B. V. Waeyenberge, B. Sorée, O. Zografos, F. Ciubotaru, and C. Adelmann. *Open Research Europe*, 2021.

[204] N. Challab, F. Zighem, D. Faurie, M. Haboussi, M. Belmeguenai, P. Lupo, and A.O. Adeyeye. *Physica Status Solidi â Rapid Research Letters*, 13:1970015, 2019.

[205] R. Rückriem, P. Krone, T. Schrefl, , and M. Albrecht. *Appl. Phys. Lett.*, 100:242402, 2012.

[206] J.âH. Lee, J. P. Singer, and E. L. Thomas. *Advanced Materials*, 24:4782, 2012.

[207] N. Challab, D. Faurie, M. Haboussi, and F. Zighem. *accepted in Physica Status Solidi â Rapid Research Letters*, 2021.

[208] N. Challab, D. Faurie, M. Haboussi, A.O. Adeyeye, and F. Zighem. *accepted in ACS Applied Materials and Interfaces*, 2021.

[209] G. Gubbiotti, P. Malagò, S. Fin, S. Tacchi, L. Giovannini, D. Bisero, M. Madami, G. Carlotti, J. Ding, A. O. Adeyeye, and R. Zivieri. *Physical review. B, Condensed matter*, 90:024419, 2014.

[210] A. N. Bogdanov and U. K. Rößler. *Phys. Rev. Lett.*, 87:037203, 2002.

[211] H. Pan, V. L. Zhang, K. Di, M. H. Kuok, H. S. Lim, S. C. Ng, N. Singh, and A. O. Adeyeye. *Nanoscale Research Letters*, 8:115, 2013.

[212] V. Kruglyak, G. Gubbiotti, M. Madami, and G. Carlotti. *Metamaterial, Chapter 14: Magnonic Metamaterials*, 2012.

[213] V. L. Zhang, F. S. Ma, H. H. Pan, C. S. Lin, H. S. Lim, S. C. Ng, M. H. Kuok, S. Jain, and A. O. Adeyeye. *Appl. Phys. Lett.*, 100:163118, 2012.

[214] Z. K. Wang, V. L. Zhang andH. S. Lim, S. C. Ng, M. H. Kuok, S. Jain, and A. O. Adeyeye. *ACS Nano*, 4:643, 2010.